CompressSpec

Photonic crystal based instrument for greenhouse gases measurements

Johannes Algera

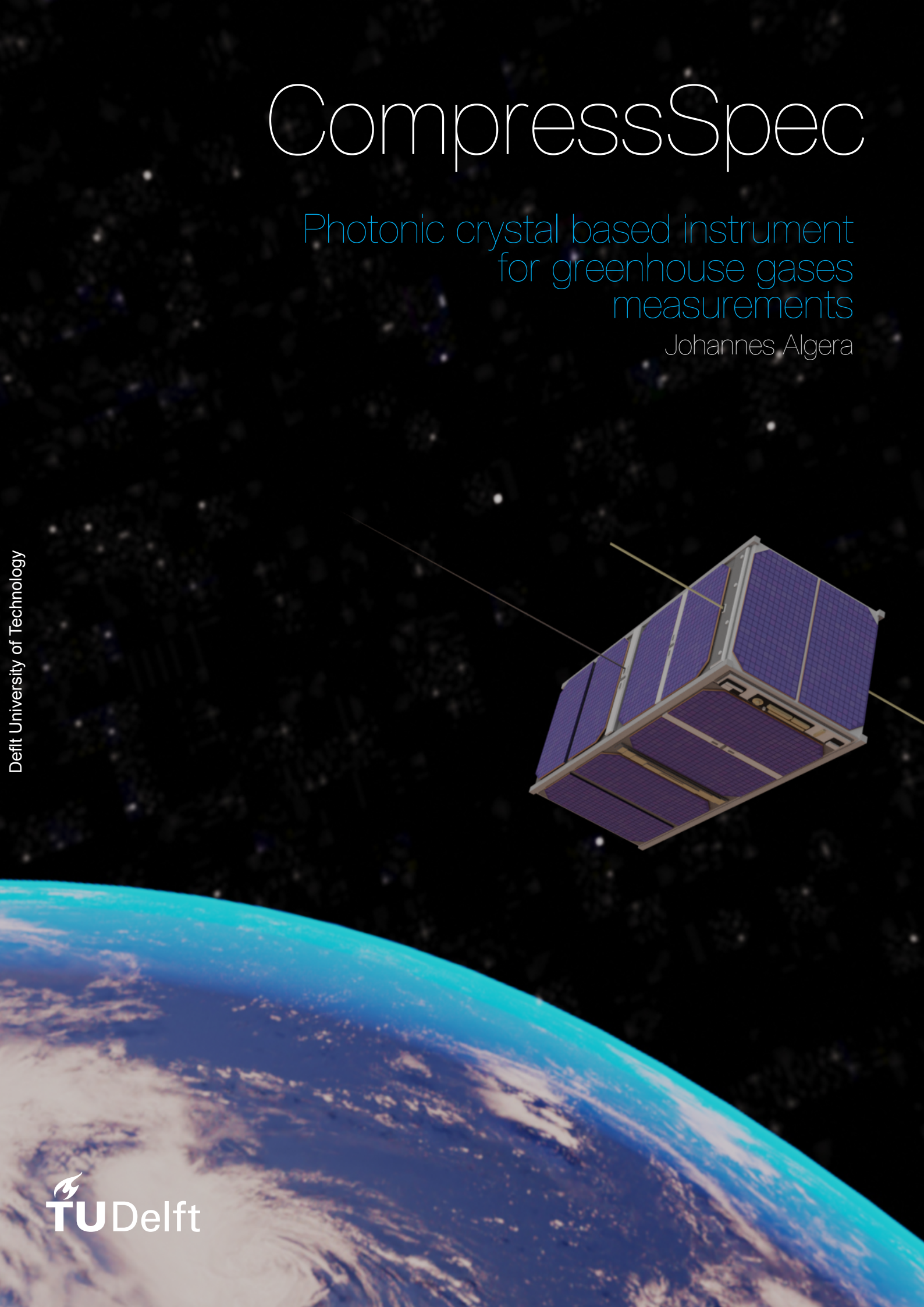

Delft University of Technology

TU Delft

Page left blank intentionally.

CompressSpec

Photonic crystal based instrument for greenhouse gases measurements

Author:

Johannes Algera (4856309)

Supervisors:

Jerome Loicq - TU Delft
Marijn Siemons - SRON

Delft University of Technology

TU Delft

Page left blank intentionally.

Preface

In May 2022, Ralf Kohlhaas responded my email about joining his interesting innovative project and invited for an interview. I am very grateful to Ralf Kohlhaas for receiving me in for that interview and creating the internship position, where I got to learn a lot about optics in practice. I initially joined CompressSpec for an internship, where I would measure the transmission profile of photonic crystals. During this time, Marijn Siemons introduced me to the optical experimentation world and guided me through some visits to the clean-room. These were all very exciting and I am greatfull for having these opportunities. At time the experiment results were disappointing, but you thought me that it is how scientific experiments sometimes go. Somethings have not been done by other people before, so there are no guidelines of what the results will be. It is important to keep an analytical mentality about them.

I would also like to thank Marijn for the many occasions that he took the time to explain me some concepts and discuss the progress of what I was doing. It was always noticeable that you took the time to reflect about the subject and the feedback was very helpful.

Furthermore, I would like to thank Marijn and Ralf for creating the thesis topic, where I got this unique opportunity to work on the development of an instrument. I would like to also thank Ralf for the organisation of the project and linking me with Jochen Landgraf. My time at SRON was very gratifying. Specially seeing that the data from space missions are being used for combating global warming, it gave extra meaning to this work.

I would also like to thanks Jerome Loicq for, first, accepting the invitation to be the supervisor for this thesis. A second perspective from outside the project was very helpful, specially to see points that were being overlooked. Also, I would like to thank you for taking the time for the meetings and having one to one discussions. With all very thought out comments. I hope we will still have many insightful conversations in the future.

Finally, I would also like to thank Jochen Landgraf with whom discussions lead to part of the method described here to select filters. His knowledge and experience on the area were very valuable for this thesis. The books and explanations provided by you were all very useful. I wish you best of luck on the development of TANGO!

Last but not least, I would like to thank my family, girlfriend and friends. For the support and leisure times, all so necessary to keep a healthy life.

Johannes Algera
Delft, December 22, 2023

Contents

List of Figures

List of Tables

1 Introduction

The Paris Agreement, signed in 2015, marked a significant milestone in global efforts to combat climate change. This agreement seeks to limit global temperature rise to below 2 degrees Celsius compared to pre-industrial levels. And it pursues efforts to limit the temperature increase to 1.5 degrees Celsius [5]. To achieve these goals, countries have committed to reducing their greenhouse gas emissions and regularly reporting their progress.

Among the green house gases, methane has one of the biggest additional direct heating of the atmosphere, second only to carbon dioxide [6]. Also, the growth in its concentration from pre-industrial levels to nowadays are predominately caused by human activity [6]. Furthermore, methane has a relatively short life time in the atmosphere of about 10 years [7]. Therefore, policies that aim to reduce the emission of methane are bound to have more impact in the Paris agreement goals in the short term. Thus there is extra interest into measuring their emissions precisely and frequently.

Various space missions have been used to measure the emission of methane and other greenhouse gases on a global scale. The measurement provided by these missions are generally the spectrum of sunlight reflected from Earth's surface. The measured spectra can then be used to retrieve the concentration of the greenhouse gases on the atmosphere. Which is afterwards used to detect and quantify various sources of green house gas emissions over time. This allows monitoring the effect of policies and if countries are achieving their goals set in the Paris agreement. Examples of such missions are: the Sentinel missions [8], SciSat-1 [9], FengYun-3d [10], Gaofen-5 [11], Metop-C [12], EnMAP [13], PRISMA [14], GOSAT [15], GOSAT-2 [16], Aqua [17] and GHGSat [1].

Many of the missions cited use dispersion based spectrometers (grating or prisms). GHGSat is an exception, which uses a Fabry-Perot resonator whose transmission has sharp peaks in the spectral domain. The position of these peaks shift as the object on the ground moves over the field of view, thus the entire spectrum of interest can be covered, as shown in Figure 1.1.

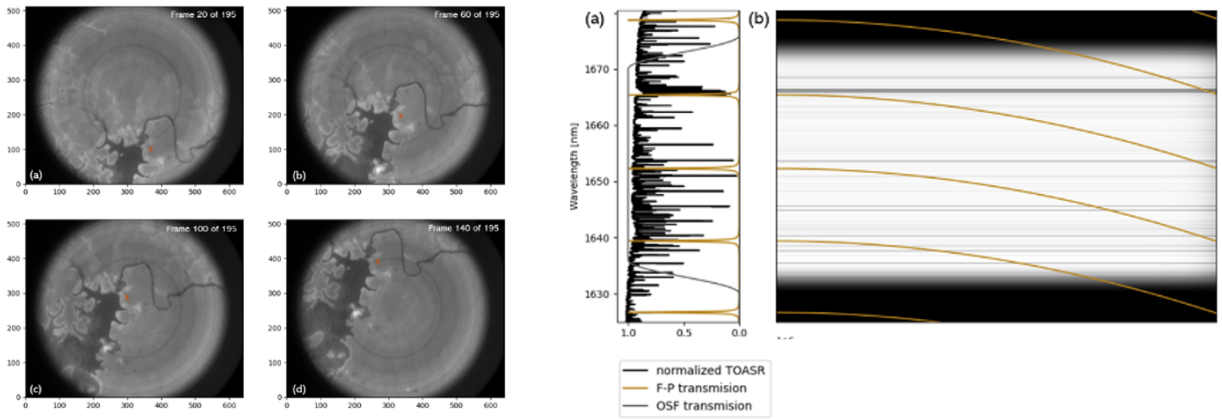

Figure 1.1: Working principle of GHGSat. On the left 4 images of the same facility moving along the field of view. On the right, the transmission of the Fabry-Perot resonator and the shift of the peaks with the change of incidence angle [1].

The dispersion spectrometers require more volume in order to improve its spectral resolution and per consequence its precision. Making it increasingly difficult to miniaturise such instruments without los-

ing performance. On the other side, the Fabry-Perot resonator from GHGSat is easier to miniaturise. In fact, the GHGSat spacecraft is 65 times lighter than Sentinel5-P [18][1]. However, the transmission profile of the resonator reflects away most of the light that reaches the instrument. Therefore, an instrument that is not physically limited by dispersion and can sample the spectrum more efficiently than GHGSat is a strong candidate for miniaturisation of such instruments.

The costs of space missions limits the amount of spacecraft that can be launched and thus the frequency that areas can be imaged. For instance, Sentinel-5P is able to image the entire globe once a day with a single spacecraft[18]. However, it comes at a cost of having a ground pixel size of 5x7 kilometres. Which, in turn, requires higher precision of the instrument to detect small sources thus making the instrument bigger and more expensive. The size and mass are big costs drivers in the space sector. Thus reducing the size and mass of the instrument will both reduce the cost per instrument and allow the use of constellations of spacecraft to monitor the emissions of these gases. These constellations can be made of spacecraft with smaller ground pixel resolution that can still image the entire globe daily or even more frequently.

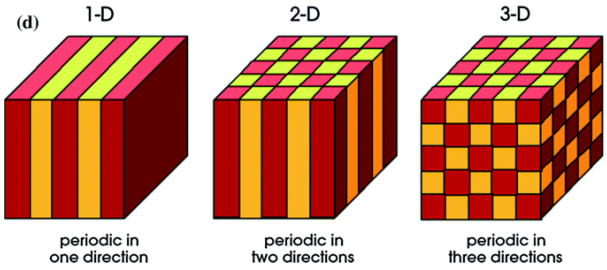

Figure 1.2: Different types of photonic crystals [2]

A Dutch proposal for such a mission is the Twin ANthropogenic Greenhouse Gas Observers (TANGO) [19]. This mission is a strong candidate for ESA's SCOUT mission, which aims to complement the measurements of the Copernicus global survey. TANGO will consist of two spacecraft flying in formation, one will measure carbon dioxide and methane while the other measures nitrogen dioxide emissions. The mission will have a swath width of 30 km, with a ground pixel resolution of 300x300 m[19]. Thus it lies between the resolution and swath width of Sentinel5-P and GHGSat. TANGO is also being developed in cooperation with the Netherlands Institute of Space Research (SRON). Thus TANGO can be used as a benchmark to compare the performance of new instruments, as it is easy to talk to people developing it.

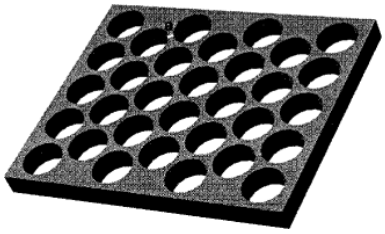

Figure 1.3: Example of photonic crystal slab. Material was carved out in the shape of circles [3]

Recently, a novel spectrometry technique was demonstrated which uses photonic crystals as optical filters [20]. Photonic crystals are periodic structures with varying dielectric constant. This periodicity can happen in 1, 2 or 3 dimensions as depicted in Figure 1.2. The periodicity of the crystal is comparable to the wavelength of the light propagating through it. This allows some frequencies to transmit through the crystal while others are completely reflected, creating photonic band gaps [21].

The photonic crystals presented in Figure 1.2 are considered to expand infinitely in all directions. A variation of the 2-D crystals are photonic crystals slabs. The difference being that it has a small thickness in the direction perpendicular to the periodicity as shown in Figure 1.3. This small thickness makes the crystal easier to manufacture, being possible to make it with single exposure photolitography or e-beam lithography[20].

Light incident on the photonic crystal slab from free space will couple to lateral guided modes in the crystal [22]. This will increase or decrease the transmission of light at certain wavelengths, creating spectral features such as in Figure 1.4. These spectral features can then be used to achieve desired transmission profiles for the sampling of the radiance on top of the atmosphere.

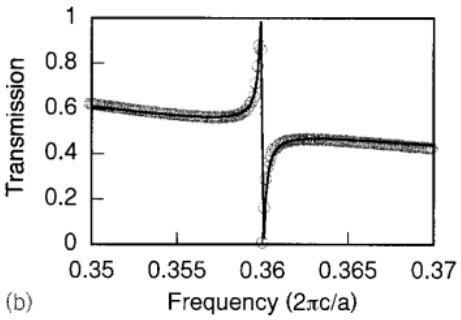

Figure 1.4: Transmission of a photonic crystal at a wavelength that a resonance occurs. 'a' is the lattice size, or the size of the repeating structure in the crystal.[3]

Can the novel spectrometer of Wang [23] be adapted for space applications such as the remote sensing of methane? What ways could these filters be adapted for such applications? This thesis will investigate these questions. The main focus will be on remote sensing of methane due to its impact on the goals of the Paris agreement in the short term. Also, an instrument with photonic crystal filters has the potential to better sample the spectrum compared to GHGSat but also does not have the physical limitations of dispersion based instruments. Lastly, the TANGO instrument design and concept provides an excellent comparison to a state-of-the-art, but conventional imaging spectrometer and will be used for that.

Some work on this instrument concept has been performed in SRON already [24]. This included the development of an instrument simulator, which will be described in Chapter 3. This instrument uses a push broom concept where an area on the ground will be imaged using a series of filters. For every picture that the instrument takes it images an area as shown in Figure 1.5. The area marked by an "X"in the image will be first imaged through filter 4 in the instrument. In a latter picture this "X" will be imaged through filter 3, due to the movement of the spacecraft. So a small area on the ground is imaged by multiple filters. The concentration of methane is then inferred from these measurements.

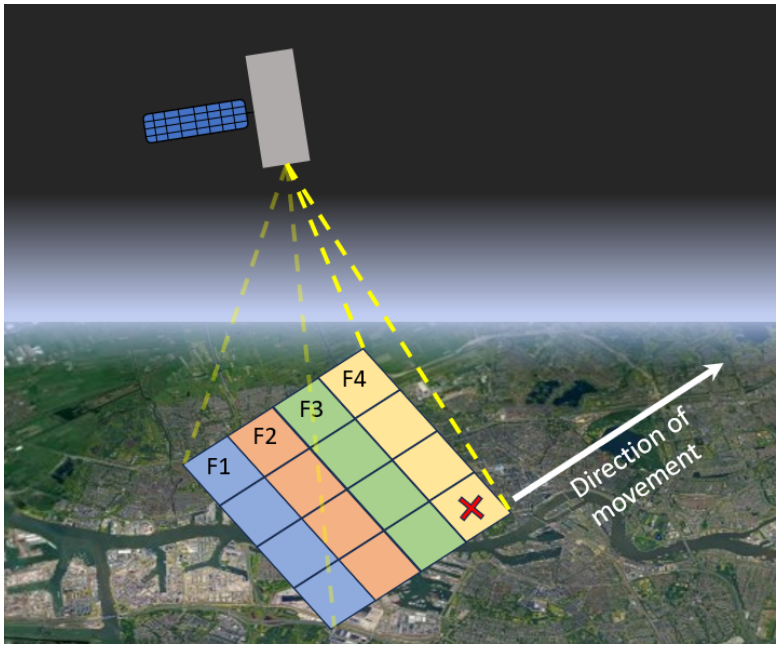

Figure 1.5: Sketch of the push-broom concept with filters. The same area on the ground is first imaged by filter F4 and then by filter F3 and so on.

The research question for this thesis is then: **"Is an instrument based on photonic crystals filters viable for remote sensing of methane?"**. This question was subdivided into the following research questions:

1. What way of using photonic crystals for remote sensing is the most viable?
2. How does the instrument perform when considering the concentrations of other gases and spectral dependency of the surface reflectance?
    (a) What gases influence the retrieval of methane in the chosen band?
    (b) How big is the influence of the spectral dependence of surface reflectance?
    (c) How can the filter selection be improved based on the concentration of other gases and surface reflectance?
    (d) What are the effects of expanding the wavelength range used by the instrument?
3. What is the size of such an instrument?
    (a) What is the trade-off between Field of View, F-number, number of filters, spatial resolution and retrieval precision?
    (b) What is a viable optical design for such an instrument?
    (c) How does the instrument compare to TANGO?

The transmission profile of the photonic crystals change when it is positioned in the image plane or in the infinity space of an optical system, as will be explained in Chapter 2. It is necessary to evaluate concepts that use photonic crystals in different ways, these are explored and traded-off in Chapter 2. Thus answering the first question.

Afterwards, the instrument performance simulator is explained in Chapter 3. This is used in latter comparisons of filter selections methods. It is followed by the explanation of methods developed here for selecting filters, in Chapter 4. These methods are mainly based on the sensitivities of each filter to the greenhouse gases and the singular value decomposition of a set of filters.

After that, the filter selection methods are compared to a selection made using an evolutionary algorithm in Chapter 5. In this comparison, the effect of other greenhouse gases and the wavelength dependency of the surface reflectance are also investigated. Thus answering the second question.

It is followed by answering the third question in Chapter 6, where the telescope design is explored by exploring the variables that it depends and chosen values for them. Furthermore, two different telescope design are presented that can be compared with TANGO.

Finally, the outlook for this instrument is explored in Chapter 7. It explores how better the filter selection can become and the potential gains of finding photonic crystals that are less angle dependant.

2
Concept generation and analysis

This chapter aims to answer the first research sub question *"What way of using photonic crystals for remote sensing is the most viable?"*. It explores how the properties of photonic crystal slabs could be used to sample the spectrum. This comparison started by picking the criteria to trade off concepts in Section 2.1. This is followed by the method used to generate concepts and their explanations in Section 2.2. After that the concepts are traded-off, the trade off and the explanation on how each concepts was ranked for each criteria is given in Section 2.3.

In the context of space systems, objects are considered to be extremely distant. Therefore, light that reaches the imaging system from the object is considered to be collimated. Thus one side of the imaging system is called the infinte plane whereas the other side is the image plane, as illustrated in Figure 2.1. Placing the photonic crystal on a infinite plane is equivalent to a collimated beam incident on the crystal. Whereas, placing the crystal on the image plane is equivalent to focusing the light on the crystal.

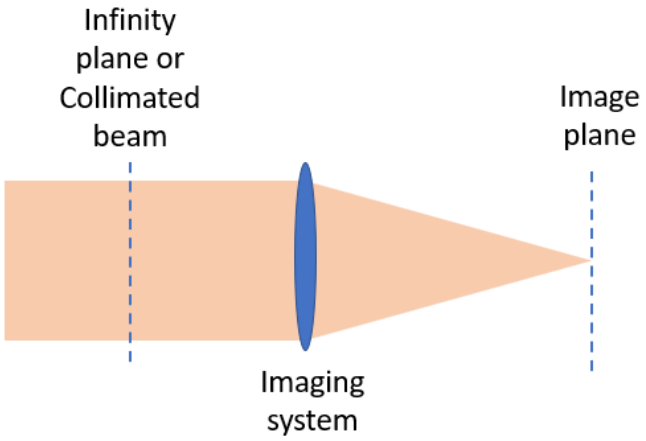

Figure 2.1: The difference between image plane and infinity plane.

The transmission of photonic crystal slab is angle dependent [22]. The filter will have a certain transmission profile if a plane wave is incident normal to it. This profile changes as the angle of incidence of the plane wave also changes. Also, a beam that is focused on a crystal can be modelled as a superposition of plane-waves with varying incidence angle(with the appropriate intensity and phase terms). Hence, when directing a focused beam onto the crystal, the transmission can be similar to a combination of the transmissions of plane waves with various incidence angles. This was also observed experimentally at SRON. On the experiment the transmission of a photonic crystal was measured for three cases: plane wave, a top hat beam focused on the crystal and a Gaussian beam focused on the crystal. The results are shown in Figure 2.3.

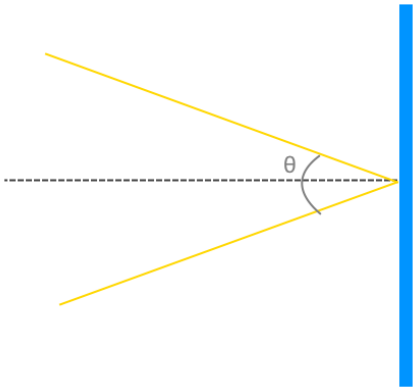

Figure 2.2: Illustration of the angle theta of a focused beam, equivalent to the F-number.

The effect of this combination of incidence angles is the dampening of the sharp spectral features. This may be prejudicial for the sampling of the spectrum. However, this can be limited by constraining the F-number, or the angle of the cone of light incident on the crystal, shown in Figure 2.2. The smaller this angle is, the more similar it becomes to a collimated beam.

Also adding a Gaussian mask in the instrument aperture may help reducing the dampening of the spectral features. This is due to it reducing the weight of the components with a bigger incidence angle in the cone of light shown in Figure 2.2. This was also observed experimentally, as shown in Figure 2.3.

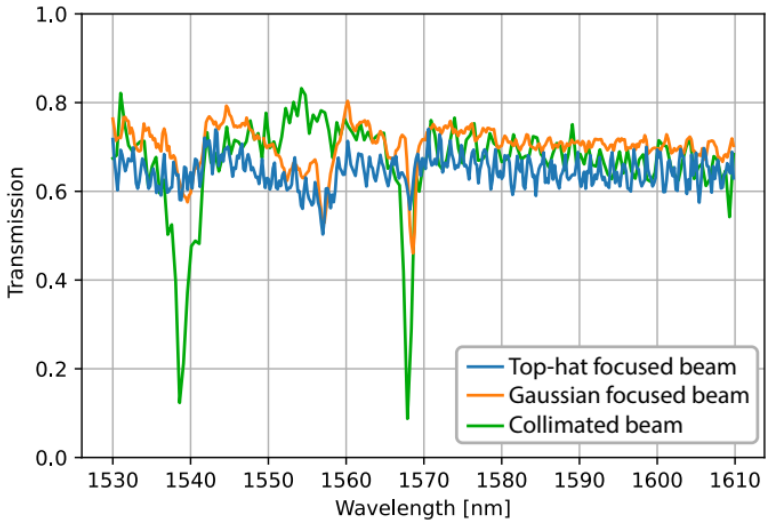

Figure 2.3: Transmission of a photonic crystal with plane wave at normal incidence, focused Top-hat beam and focused Gaussian beam.

The concepts will then explore ways of positioning the photonic crystal filter in the infinite plane or in the image plane of the imaging system. They consider how the transmission profiles of the filters will behave on each of those planes, how much light get through the system, the complexity of the system and also the generation of stray light.

2.1. Criteria selection

The criteria were selected before knowing the concepts. This is done in order to compare the concepts as objectively as possible. Four criteria were selected, as presented in Table 2.1.

“Cost” is driven by: the number of elements that the concept would require; and how complex the manufacturing technique is. Concepts that requires more elements, such as mirrors and extra structure, will likely be more expensive. Also concepts that require more complex manufacturing techniques are bound to be more expensive. No exact calculations of cost are done, only qualitatively estimating what would be more expensive.

The “Spectral features” criterion is used to compare the spectral diversity of the photonic crystals transmission. This diversity changes, for instance, if the beam is focused onto the crystal, thus it depends also on the concept.

“Stray light” was considered due to the photonic crystals reflecting back some of the light and scatter some light forward. This light can propagate through the instrument and introduce a bias in the measurement, thus degrading the instrument performance.

Finally, “Signal to noise ration & Fov/Ground resolution” was considered due to it impacting the performance of the retrieval algorithm. Concepts that lead to higher signal to noise ratio are favoured. This is due to higher SNR leading to a better precision of the retrieval algorithm. Also concepts that limit more the Field of view are less favoured due to adding a restriction on the covered area.

The criteria were then ranked in importance, such that concepts can also be ranked. The rank is shown in Table 2.2. “Cost” was ranked the highest because the objective of this instrument is to reduce the size and cost compared to similar instruments. It is followed by “Spectral features” and “Signal to noise ration& FoV/Ground resolution”, both of them affect the performance of the instrument, which is of interest for the scientist that will use its data. Stray-light comes in last due to the possibility of using baffles, coatings and numerical methods to reduce its effect on the performance of the instrument.

The rubric used to score the concepts is shown also in Table 2.1.

Table 2.1: Selected criteria and the rubrics for rating concepts per criterion

Score	Cost	Spectral feutres	Stray light	Signal to noise ratio & FOV/Ground resolution
Very good	Just requires a telescope. Simple manufacturing technique	Very sharp spectral features and possibility for many different filters	No stray light in the instrument	Concept does not reduce SNR nor limit FoV
	Adds few elements or a manufacturing technique	Very sharp spectral features but limited variability of filters	Concept already offers some straylight control	Concept imposes some restrictions in the FoV
Standard	Adds elements that make the instrument bigger	Some smearing of spectral features but possibility of many different filters	Addition of baffles may control the stray light generated	Concept imposes some restrictions in SNR and FoV
	Makes the instrument significantly bulkier or expensive manufacturing	Significant smearing and limited variability of filters	Straylight propagates significantly into the instrument before it can be baffled	Concept significantly reduces SNR due to division of aperture or the detector
Very bad	The instrument is no longer smaller than dispersion spectrometers	There are no spectral features	Stray light dominates the instrument measurement	Extreme reduction in SNR and/or very limited FoV

Table 2.2: Selected criteria and what is important for each of them

Rank	Weight	Criterion	Justification
1	4	Cost	Main driver to launch more spacecraft.
2	3	Spectral features	Spectral features affects the precision of the instrument
2	3	Signal to noise ratio & FoV/Ground resolution	Also affects directly the precision of the instrument
4	1	Stray light	Stray light will introduce bias in the retrieval. However there are ways of reducing its impact.

2.2. Concepts generation

The concepts were generated using a discovery tree in order to facilitate the discovery of new options. The discovery tree used is shown in Figure 2.4.

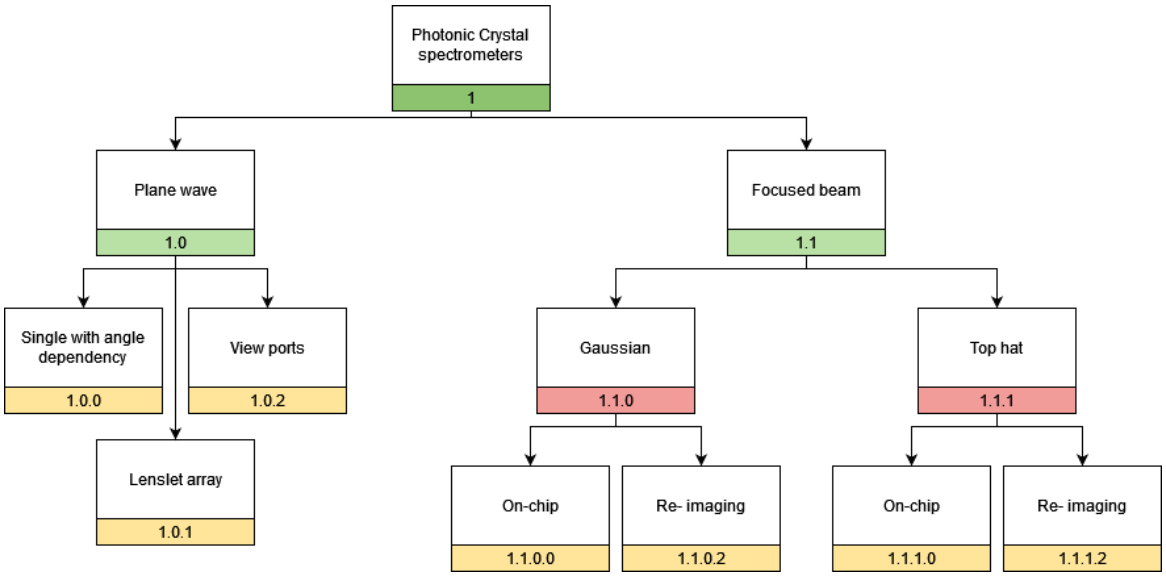

Figure 2.4: Discovery tree used to find concepts for the instrument.

The first level was divided into plane wave and focused beam. This is equivalent to placing the crystals in the infinite or in the image plane, as in Figure 2.1. The focused beam is further divided into Gaussian and top-hat. The Gaussian beam has a Gaussian intensity profile when collimated while the top-hat has a flat intensity profile, as shown in Figure 2.5. The intensity profile changes how the plane waves combine on the focus and thus the transmission profile. The Gaussian profile requires a Gaussian-mask at the aperture to reach its intensity distribution. From those divisions the concepts derived were: view ports, single photonic crystal with angle dependency, lens-let array, on chip and re-imaging.

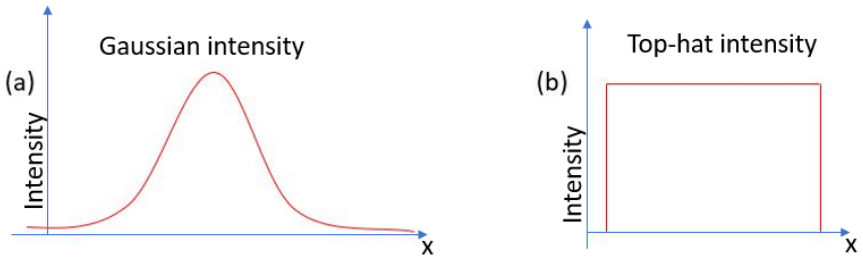

Figure 2.5: The intensity distribution of a collimated beam, one with a Gaussian distribution and the other with a top hat distribution.

2.2.1. View-ports

The first idea for using the transmission of the photonic crystals with plane waves are using view ports. The instrument would have a handful of view ports with a photonic crystal each, as in Figure 2.6. Each photonic crystal would have baffle such that only light incident normal to the photonic crystal surface can reach it. This way the light that reaches each filter can be considered to be a plane wave at normal incidence angle.

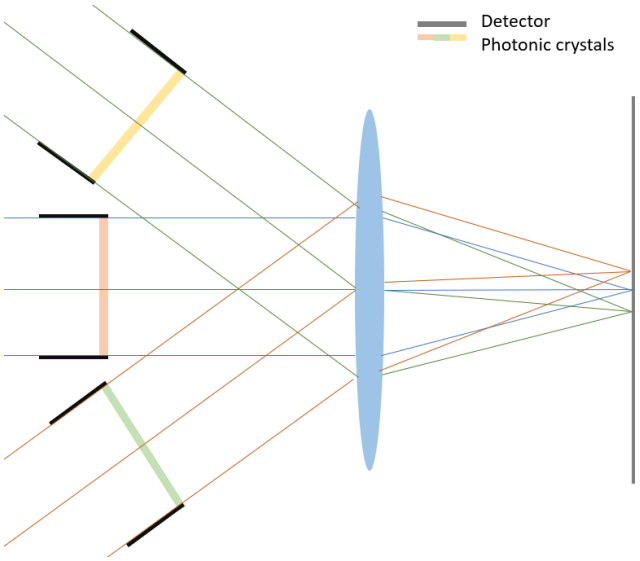

Figure 2.6: Concept that separates the photonic crystals into view-ports.

2.2.2. Angle dependency of transmission concept

This concepts would require a photonic crystal or a stack of photonic crystals whose transmission is significantly dependant on the incidence angle of the light, as in Figure 2.7. As a point on the ground travel along the field of view, the light reflected by the ground point will go through the photonic crystal at different incidence angles. The transmission profile of the photonic crystal would be angle dependant,therefore the transmission profile would also change.

This is similar to what is done by GHGSat [1]. However instead of using a Fabry-Perot resonator, a photonic crystal with transmission with angle dependency would be used.

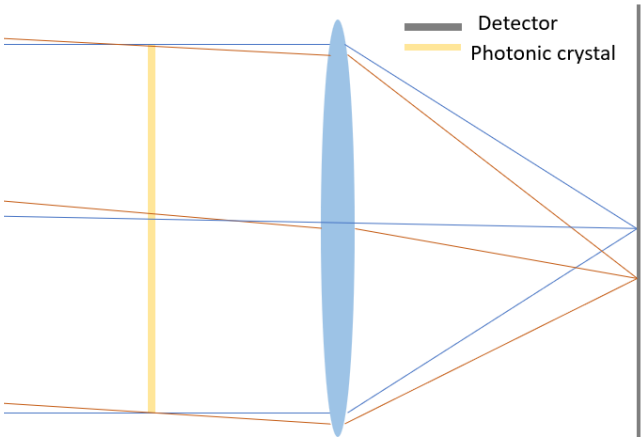

Figure 2.7: Concept that uses a photonic crystal whose transmission has significant angle dependency.

2.2.3. Lens-let array

The lens-let array would image the same area multiple times onto the detector, similar that what is done in Nanocarb [25]. It is also similar to the single angle dependency photonic crystal, however a different crystal can be used for each lens-let, as in Figure 2.8. This way a more diverse filter transmission set can be achieved when compared to the single photonic crystal with angle dependency.

In fact, each lens-let would image the entire scene. Therefore the detector has to be shared with multiple lens-lets, thus reducing the amount of pixels that the scene get.

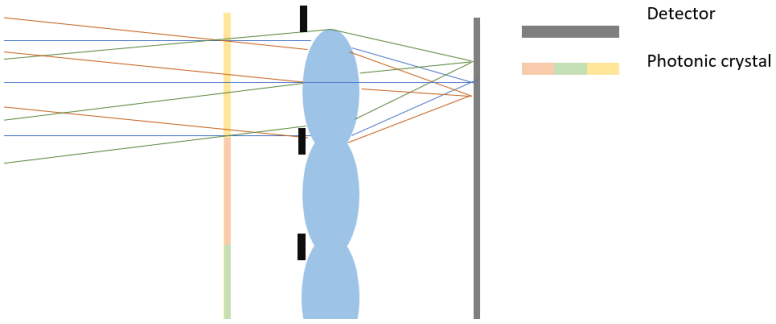

Figure 2.8: Concept with lens-let arrays

2.2.4. On chip

This concept focuses the beam onto the photonic crystal. The photonic crystal is than placed on top of the detector chip in order to make the instrument as compact as possible, as in Figure 2.9. This would require some bonding method of the crystals onto the detector. This concept can have a Gaussian mask before the telescope(represented in Figure 2.9 as a lens) or not. Thus creating two variations of it, with or without the mask.

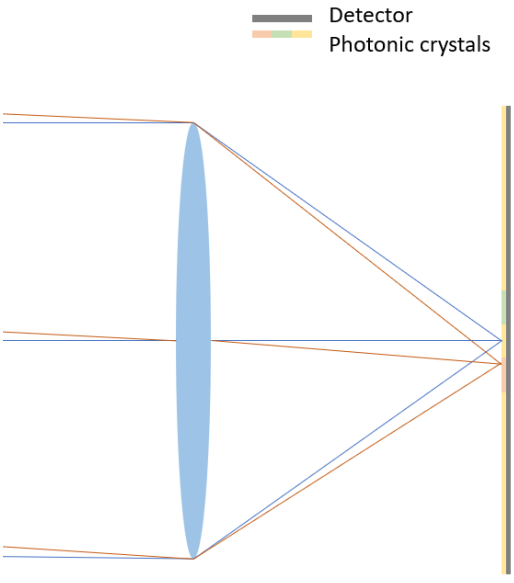

Figure 2.9: Concept that places the photonic crystal directly on top of the detector chip.

2.2.5. Re-imaging

The re-imaging concept builds onto the ”On chip” concepts. However, the photonic crystal would be re-imaged onto the detector instead of being bonded, as in Figure 2.10.This would simplify the manufacturing of the instrument at the cost of adding more elements to the telescope. It is also possible to add a Gaussian mask at the entrance of the telescope to have the transmission profile

associated with a Gaussian beam.

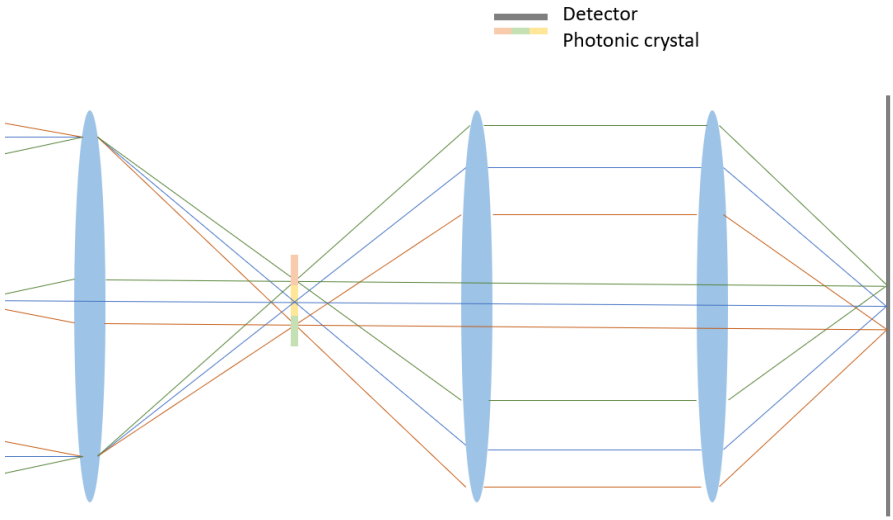

Figure 2.10: Concept that re-images the photonic crystal onto the detectors chip

2.3. Concepts trade-off

The concepts were compared using the trade off table. The justification for the rating of the concepts in each criterion is summarised in Figure 2.12. In order to give a numerical score to each concept, a number was associated to each qualification given in the trade-off table. The scores are listed in Table 2.3.

Table 2.3: Score given to each qualification for the trade-off

Qualification	Score
Very good	2
	1
Standard	0
	-1
Very bad	-2

The lens-let array concept has the advantage of using the transmission of the photonic crystal with plane waves and the possibility to use multiple filters. Also it is possible to add baffles in the lens-let array as in Figure 2.8. However, the lens-let can be very complex and expensive to manufacture. Furthermore, the detector would have to be divided into sections for each lens-let. The lens-lets also reduce the effective aperture effectively reducing the Signal to noise ratio, due to the shot noise increase.

The single photonic crystal with angle dependency has the advantage of using plane waves for the spectral features. However there is less spectral variability than when multiple photonic crystals are used. Therefore, the advantage of the plane wave is nulled by the disadvantage of little spectral variability. It also has the advantages of very few elements being necessary to the construction of the instrument, being one of the simplest concepts. Lastly, no special manufacturing technique is required, such as bonding or fabrication of complex elements.

The view ports also has the advantage of using the transmission of the photonic crystals with plane waves. However, it would be constrained by the volume of the instrument. This limits how many view ports can be added, and per consequence how many filters. Also the view ports add extra structure. Finally each photonic crystal filter would have its own aperture, which would be smaller than with concepts whose aperture is shared. Thus the signal to noise ratio would be significantly reduced.

The concepts that focus the beam on the crystal were divided into the ones with a Gaussian mask and the ones without one. The concepts with a Gaussian mask, would require a mask that reduces the intensity of light at the edges of the aperture. Simulations at SRON showed an improvement in

the transmission of photonic crystals with a Gaussian mask. This simulation reduced the electric field with a Gaussian shape cut at 2 sigma.

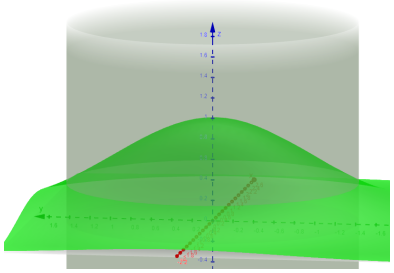

Figure 2.11: Illustration of a Gaussian electric field cut off at 2 sigma.

In order to calculate the transmission of such a mask the electric field squared was integrated over this aperture to get the total intensity. It was then divided by the intensity of a field with no Gaussian apodization to get the transmission. This transmission is independent of the value of sigma, so sigma was simplified to be 1. The transmission calculation was performed as in Equation 2.1.

$$T = \frac{\iint_0^2 e^{-\frac{2(x^2+y^2)}{2}} r \, dr d\theta}{\iint_0^2 r \, dr d\theta} = 0.158 \tag{2.1}$$

Therefore every concept that would use a Gaussian mask has a the signal reduced by 84%. For this reason these concepts were extremely penalised in the signal to noise ratio category. They are still slightly better in the spectral features criterion when compared to the top hat concepts.

The re-imaging concepts have a simpler manufacturing method but at a cost of the instrument becoming bulkier. These two facts compensate each other such that re-imaging concepts have a ”standard” score for cost.

Table 2.4: Trade off with score for each criterion and the total score based on the weights of each criterion.

Criteria	Cost	Spectral features	Stray light	SNR and FoV / ground resolution	Total score
Lens-let array	-1	2	1	-1	0,00
Angle dependency	1	-1	0	1	0,36
View ports	-1	1	-1	-2	-0,73
Gaussian on-chip	1	0	0	-2	0,18
Gaussian re-imaging	0	0	0	-2	-0,55
Top-hat on-chip	1	-1	0	2	0,64
Top-hat re-imaging	0	-1	0	2	0,27

The on-chip concepts still require the photonic crystal to be bonded to the detector however it is the simplest concepts and may be the most compact. Its disadvantage lies in the dampening of spectral feature. This can be compensated by limiting the F-number of the telescope. From Table 2.4, the winning concept from Table 2.4 is the “top-hat on-chip” and it will be used in the next chapters.

Concept name	Cost	Spectral features	Stray light	Signal to noise ratio FoV/Ground resolution
Lens-let array	Adds a len-let array which can be significantly expensive to manufacture	Has sharp spectral features due to the plane waves and more flexibility for using other photonic crystals.	The lens-let array can be coupled with baffles to control straylight	Detector array is divided for each lenlest to image the entire scene. Reducing FoV significantly and the effective aperture.
Single PhC with angle dependency	Very few elements but more than top hat on-chip	Plane wave transmission. Less variability is possible with angle dependency	Distance between Pc and detector allow for propagation of diffracted light, however it can be mitigated in filter selection	No penalties for SNR FoV is limited by the angle dependency of the PhCs
View ports	The construction of multiple viewing ports can take a lot of volume and adds elements	There are sharp spectral features. Amount of filters is physically limited due to mounting spaces	Stralight created by the PC is introduced at the entrance of the system thus propagatin more into it.	Division of apertures into view ports, reducing SNR Field of view and ground resolution is limited by the amount of viewing ports
Gaussian On-chip	Detector bonding is challenging Slightly more complex due to added gaussian mask	Focused beam smears out the spectral features, Gaussian mask compensates for the dampening Multiple filters can be used	Light reflected by the PC can become stray light but alsocan be baffled	Reduction of SNR due to Gaussian mask No penalties for FoV in a telecentric telescope
Gaussian re- imaging	Added reimaging system making the instrument bulkier No complicated manufacturing techniques	Focused beam smears out the spectral features but multiple filters can be used. Gaussian mask reduces light throughput but multiple filters can be used	Dispersion and diffraction can interfere with the measurement of neighboring pixels, however it can be mitigated in filter selection	Reduction of SNR due to Gaussian mask No penalties for FoV in a telecentric telescope
Top hat On-chip	Detector bonding is required Minimum amount of components possible	Top hat profile has the most feature dampening	Light reflected by the PhC can become stray light	No penalties for SNR No penalties for FoV in a telecentric telescope
Top hat re- imaging	Added reimaging system making the instrument bulkier No complicated manufacturing techniques	Top hat profile has the most feature dampening	Dispersion and diffraction can interfere with the measurement of neighboring pixels, however it can be mitigated in filter selection	No penalties for SNR No penalties for FoV in a telecentric telescope

Figure 2.12: Trade-off table used to compare the different concepts

3
Instrument performance simulator

The instrument performance simulator was made to numerically evaluate the precision of the instrument. It is divided into a forward part and an inverse part. The forward model simulates a measurement of the instrument for a given scene. It is sub divided into a radiance model and an instrument model, as shown in Figure 3.1. The radiance and instrument model will be explained in Section 3.1 and Section 3.2 respectively. In brief, the forward model will take as inputs the solar radiance, the transmission profile of a set of filters and parameters related to the scene it is observing. It will output then what readings the instrument would generate for that scene.

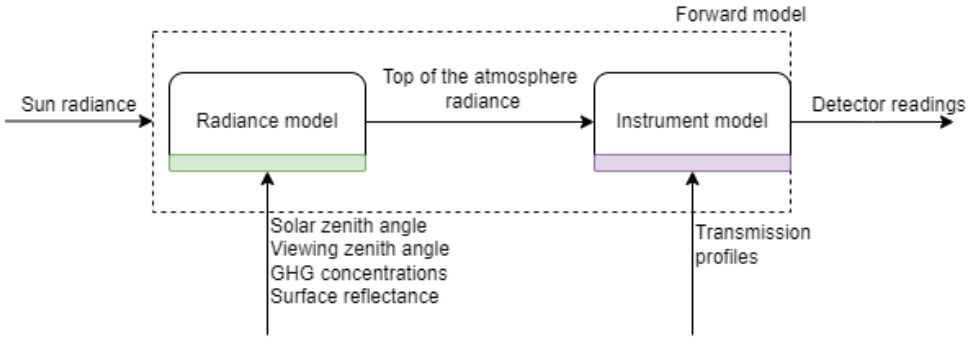

Figure 3.1: Diagram of inputs of the forward model, its sub divisions and the output. The output is the amount of electrons that would be at each detector pixel, including noise.

The inversion model is similar to the forward model. The difference being the output of the inversion model does not contain noise, shown in Figure 3.2. It is used to estimate what inputs were given to the forward model in order to generate a given measurement (y). This is done using a least square solver and the flow is depicted in Figure 3.2. This operation can be represented by Equation 3.1, where y is the output of the forward model, $F(x)$ is the output of the inversion model and x are the inputs of the inversion model. The objective is to minimise the squared error.

$$min[(y - F(x))^2] \tag{3.1}$$

The solution found by the least squares solver is called the best fit or the retrieval. The solution will be slightly different than the input to the forward model, due to the noise of the measurements. The deviation from the true value can be evaluated by the precision, bias and the total error of the instrument. These will be better explained in Section 3.3.

It is also possible to manually specify the inputs of the inversion model. Values can be passed for the concentration of each gas used in the radiance model. In such cases, the inversion model doesn't attempt to estimate the concentrations of these gases; instead, it takes the provided values as given. It's important to note that if the specified concentrations differ from what was used in the forward model, it can introduce a retrieval bias.

For instance, it is possible to pass to the inversion model the concentration of carbon dioxide as 500ppm, whereas the forward model used 400ppm. It becomes impossible for the inversion model to exactly match the forward model output and it will introduce a systematic error. The bias due to wrong assumptions will be investigated in Chapter 5.

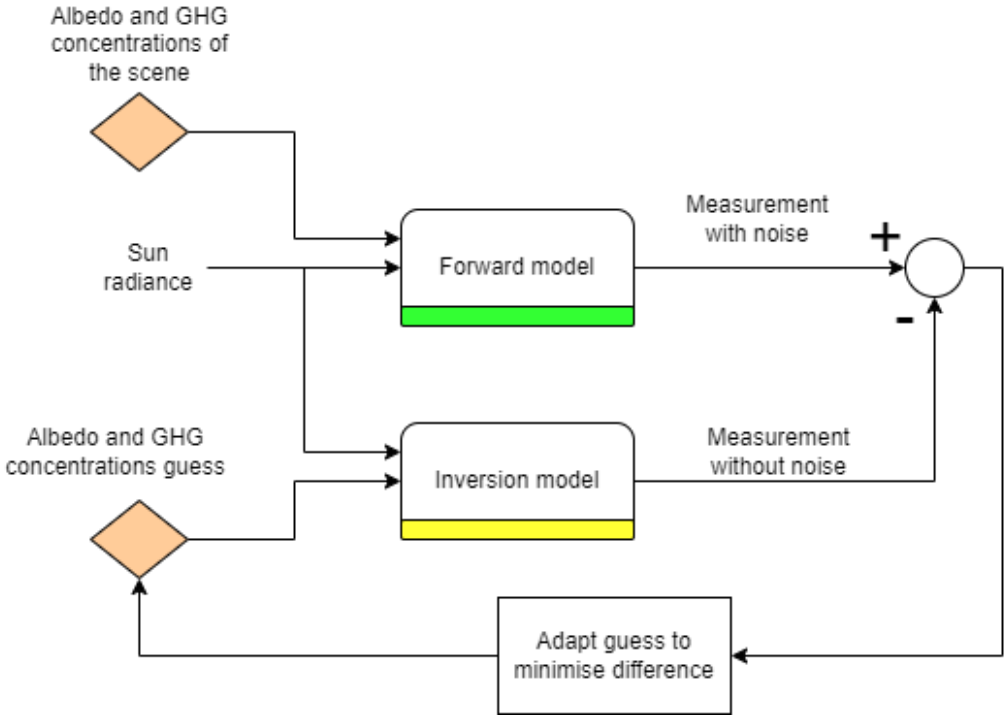

Figure 3.2: Diagram of how the forward and inversion models are used to retrieve the concentration of the guesses in the scene. A least squares solver is used to find the concentration of the gases and albedo that is to be inserted into the inversion model.

3.1. Radiance model

The radiance model simulates the transmission of the solar rays through the atmosphere, including the reflection on the surface of Earth. It takes the solar irradiance as input and outputs the top of the atmosphere irradiance, depicted in Figure 3.2. This relation depends on the solar zenith angle, viewing zenith angle, the surface reflectance and the concentration of greenhouse gases, shown in Figure 3.4. The solar irradiance used was provided by Paul Tol from SRON, it uses the Thuillier baseline and adds Kitt Peak lines. It is shown in Figure 3.3.

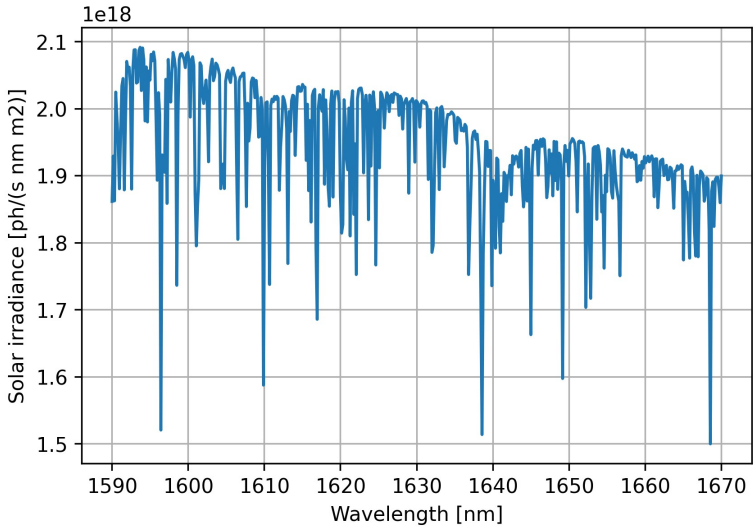

Figure 3.3: Solar irradiance used as input for both forward and inverse models.

As the light goes through the atmosphere it is partially absorbed by the greenhouse gases. The absorption of the gas depends both on its molecule structure and the gas pressure. Thus the atmosphere is modelled with layers with different pressure and gas concentrations. In this case, the

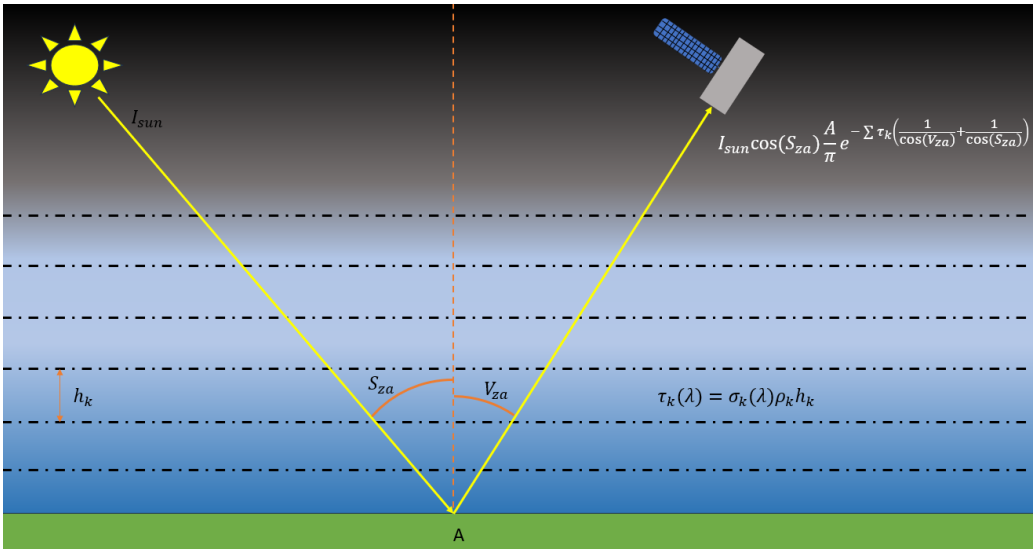

Figure 3.4: Sketch of the model of the atmosphere used in the simulation. The atmosphere is divided into layers. Each layer with its own attenuation, gas density and height. This is due to the absorption lines being dependant on pressure. The path length of the light through the layers depends also on the solar zenith angle and viewing zenith angle, defined as in the image.

atmosphere is divided into 24 layers; their thicknesses, pressure and gas concentrations are shown in Appendix A. Scattering caused by the atmosphere was not considered in this model.

The total optical thickness of the atmosphere (how much light will be absorbed at each wavelength) depends on the optical thickness of each layer. Which is given by Equation 3.2, where $\rho_{m,k}$ is the density of the gas m on layer k, $\sigma_{m,k}$ is the attenuation of gas m on layer k and h_k is the thickness of layer k.

$$\tau_k(\lambda) = \sum_m \rho_{m,k}\sigma_{m,k}(\lambda)h_k \tag{3.2}$$

HITRAN data [26] was used for the attenuation per gas for each layer as function of wavelength, noted that it depends on the pressure of the layer. The gases considered were: methane, carbon dioxide, carbon monoxide, nitrous oxide and water vapour. The total optical thickness is then the sum of the optical thickness of each layer:

$$\tau(\lambda) = \sum_k \tau_k(\lambda) \tag{3.3}$$

The optical thickness is defined perpendicular to each layer. However the gas takes a longer path in the atmosphere due to the solar zenith angle and viewing zenith angle, as depicted in Figure 3.4. Therefore the optical thickness has to be scaled by the longer path. If the light is consdered to travel in a straight line Equation 3.4 is used.

$$r_{air} = \frac{1}{\cos(S_{za})} + \frac{1}{\cos(V_{za})} \tag{3.4}$$

However, the light path curves as it travels through the atmosphere due to refraction caused by the density gradient. An approximation of the curved path was developed by Young [27]. The scaling of the path becomes as in Equation 3.5, where f_{Young} is the function developed by Young.

$$r_{air} = f_{Young}(S_{za}) + f_{Young}(V_{za}) \tag{3.5}$$

The total transmittance is the exponential of the total optical thickness scaled by the longer path, according to Beer-Lambert law. The atmosphere transmittance is given in Equation 3.6.

$$\alpha = e^{\tau(\lambda)(r_{air})} \tag{3.6}$$

How much light will be reflected from the surface depends on the illumination angle (Solar zenith angle) and the surface reflectivity ($A(\lambda)$). The total light that reaches the top of the atmosphere can be derived straight from Figure 3.4 and is equal to:

$$I_{ToA}(\lambda) = I_{sun}(\lambda)\cos(S_{za})\frac{A(\lambda)}{\pi}\alpha = I_{sun}(\lambda)\cos(S_{za})\frac{A(\lambda)}{\pi}e^{\tau(\lambda)r_{air}} \tag{3.7}$$

In the model the wavelength range can be defined, as well as how many points there should be in this range. The output of the radiance model is then two arrays: one with the wavelength and the other one with the top of the atmosphere radiance. A typical top of the atmosphere radiance is shown in Figure 3.5, with the regions with absorption lines due to carbon dioxide and methane highlighted.

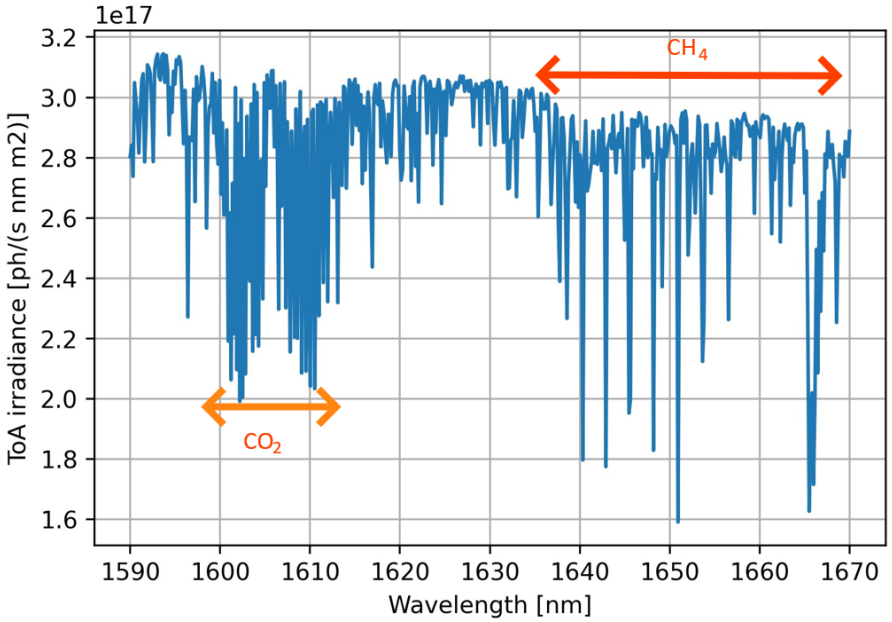

Figure 3.5: Top of the atmosphere radiance for methane 2000ppb, albedo = 0,7 and sza=10 degrees. In the left, a region rich with absorption lines due to CO_2. In the right, a region rich with absorption lines of CH_4.

The surface reflectivity depends on the material and can change with wavelength. In order to model the surface reflectance, data from ECOSTRESS was used [28]. ECOSTRESS is a mission from NASA that was meant to evaluate the stress of plants by accurately measuring their temperature. A by-product of this mission was the measurement of the reflectance as a function of wavelength for many materials.

Materials of this library could be picked and simulated with. The materials are separated into 8 categories, however some of them did not have data on the wavelength range used by the instrument thus they were not used. The number of materials per category is listed in Table 3.1.

The radiance model required albedo values between data points from ECOSTRESS. Thus polynomials were fit to the data, this also compensated for measurement noise in the data set from ECOSTRESS. Sixth order polynomials were fitted to each material, so 7 coefficients were found for

Table 3.1: Groups of materials and amount of materials per group that were imported from ECOSTRESS

Material group	Amount of materials
manmade	29
meteorites	0
mineral	163
non-photosynthetic vegetation	31
rock	154
soil	36
vegetation	132
water	6

each of them as in Equation 3.8. Given the coefficients, Equation 3.8 could be used whenever the reflectance had to be calculated for a wavelength between 1.59um and 1.67um.

$$R(x) = c_0 + c_1 x + c_2 x^2 + c_3 x^3 + c_4 x^4 + c_5 x^5 + c_6 x^6 \tag{3.8}$$

The data points and fitted polynomials for 3 materials from ECOSTRESS can be seen in Figure 3.6

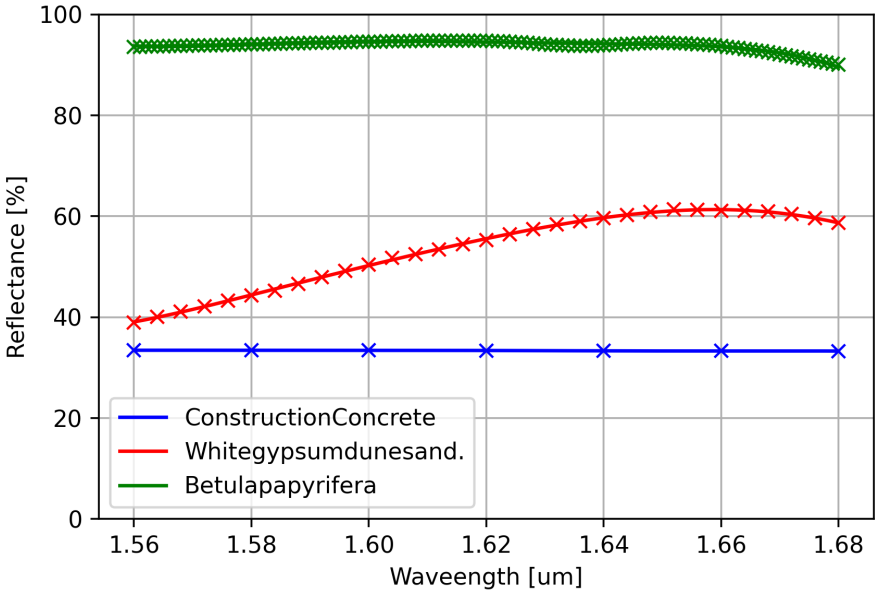

Figure 3.6: Reflectance of three different materials from ECOSTRESS. The crosses are data points and the lines are the fitted polynomials.

The inversion model also has to retrieve the albedo of the surface. It was constructed such that it is possible to choose how many coefficients it tries to retrieve. For instance, if the inversion model is configured to retrieve 2 albedo coefficients, it will model the surface reflectance of Equation 3.8 as a linear polynomial.

3.2. Instrument model

The instrument model takes as input the top of the atmosphere radiance provided by the radiance model and outputs the detector reading in electrons, as in Figure 3.1. Noise can be added to the detector reading and will be explained in this section.

The instrument is modelled as a simplified optical system with no aberrations and maximum transmittance (optical surfaces do not scatter nor absorb light). So there are no losses.

The instrument has a push-broom configuration. Lines of filter will brush the imaged area as a broom. Therefore each ground sampled element (represented in Figure 3.10 by a small square) will be imaged by various filters. The instrument has the filter placed on top of the detector(shown in Figure 3.7) such that the light that goes to different areas of the detector also goes through different filters, as explained in Figure 3.8.

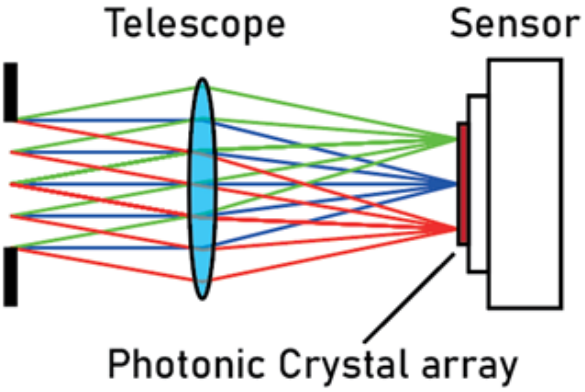

Figure 3.7: Sketch of the instrument, photonic crystals are placed on the detector. Taken from presentation for COMPRESSPEC in ESA's workshop for innovative technologies.

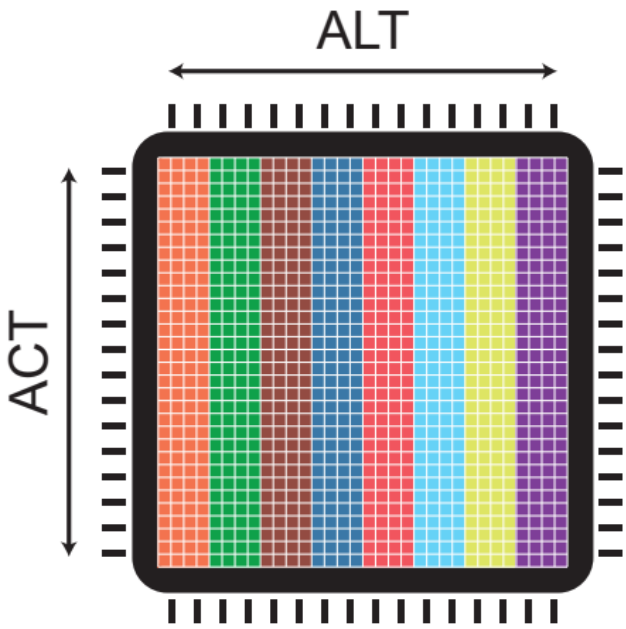

Figure 3.8: Detector with different filters placed on it. Points on the ground will move in the along track direction, thus also moving over different filters.

The detector to be used is Lynred's SNAKE. It is an InGaAs detector suitable for measuring wavelength from 0.9μm to 1.7μm. The array has 640x512 pixels. The longer side was chosen to be used for spectral information (Along track direction). Filters can cover more than one pixel, thus the transmission of filters can be the same for multiple pixels.

The transmission of 4374 photonic crystals were previously simulated in Lumerical. Various shapes and lattice sizes were simulated, such as the ones shown in Figure 3.9. Their shapes, spacing between structures and size of the structures were varied in the simulation. This was done to get a diverse library of filters. The transmission of the simulated filters could then be picked to be used in the instrument. The initial spectral range used for their transmission was from 1625nm to 1670nm. In Chapter 5 the extension of this range is also investigated.

An evolutionary algorithm was used to select an initial set of filters. It ran the instrument simulator and selected filters that improved the methane precision. The result were the 13 filters whose transmission are shown in Figure 3.11. These filters will be used for the initial analyses of the instrument performance and then for comparison with other methods of selecting filters in Chapter 5.

The instrument model generates 640 measurements for each ground element, due to the number of

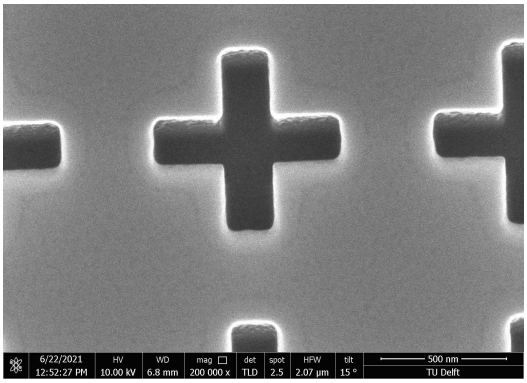

(a) Photonic crystal composed of crosses, height of 600 nm

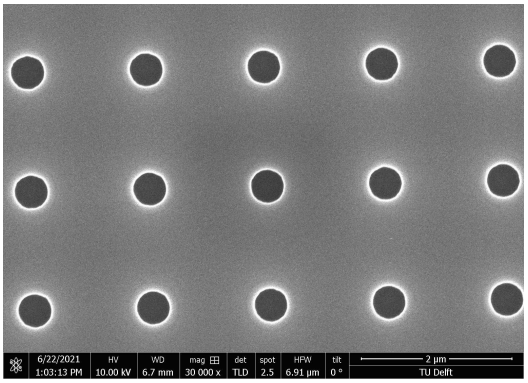

(b) Photonic crystal composed of circles with 400 nm diameter

Figure 3.9: Images of photonic crystals that were manufactured, one with crosses and another with circles.

detector pixels in the along track direction. These measurements depend on the quantum efficiency of the detector, the integration time, the etendue of the instrument and the filter associated with that pixel. The amount of electrons on each detector pixel (y_i) per reading is calculated with Equation 3.9.

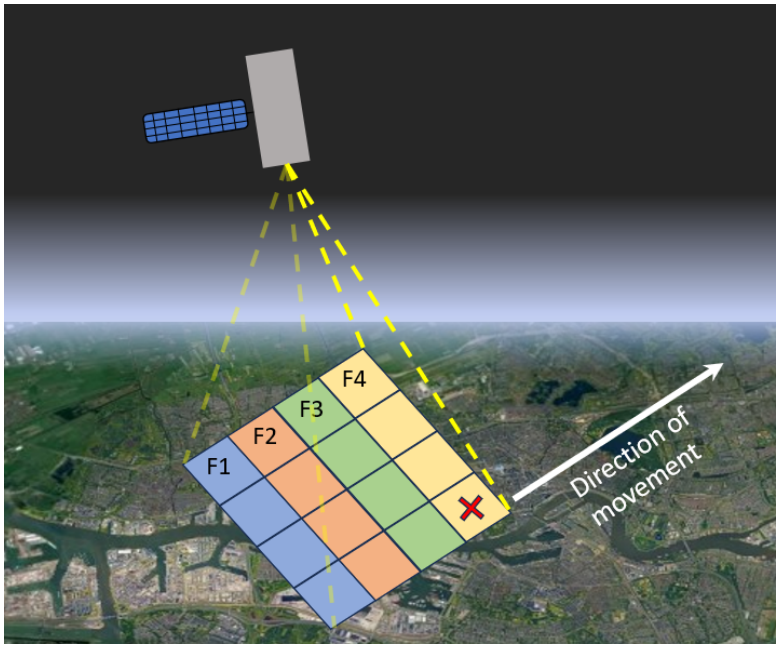

Figure 3.10: Sketch of the push-broom concept with filters. The same area on the ground is first imaged by filter F4 and then by filter F3 and so on.

$$y_i = \int q_e t_e \varepsilon T_i(\lambda) I_{ins}(\lambda) d\lambda \tag{3.9}$$

The values used for Equation 3.9 are shown in Table 3.2 and will be further explained in Chapter 6. The noise is modelled using Equation 3.10, where σ_r is the read noise, y is the noiseless measurement and i_{dark} is the detector's dark current. This noise is then added to the measurement using Equation 3.11, where $N(0,1)$ is a random number from a sample with normal distribution, average zero and standard deviation 1. This is done in order to emulate the randomness of the noise. In the end, y_{total} has an expectation equals to y and a standard deviation equal to y_{noise}.

$$y_{\text{noise}_i} = \sqrt{y_i + \sigma_r^2 + i_{\text{dark}} t_e} \tag{3.10}$$

Table 3.2: Values used in the calculation of the detector readings

Variable	Value	Unit
ε	6.248e-12	[-]
q_e	0.8	[e/ph]
t_e	8.496	[ms]

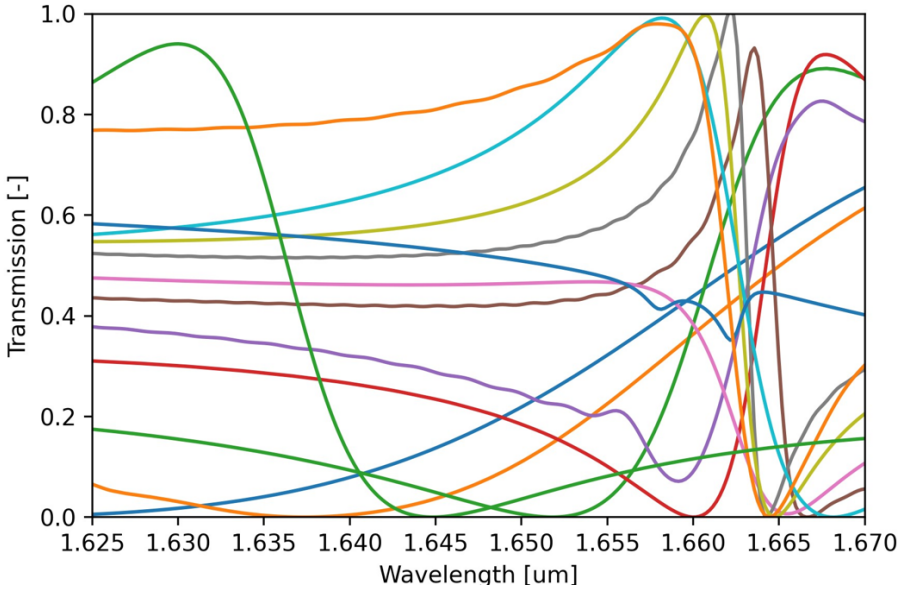

Figure 3.11: Transmission of filters selected using an Evolutionary algorithm

$$y_{\text{total}_i} = y_i + y_{\text{noise}_i} N(0,1) \tag{3.11}$$

The data used for the detector specifications were taken form the Lynred's SNAKE detector. The read noise is $300\ e^-$ and the dark current is $30000\ e^-/s$. In the inversion model the noise is not added to the measurement.

3.3. Calculations of precision, bias and total error

The retrieval of the inversion algorithm will deviate from the true value depending on noise and the selected filters. In order to asses this deviation, the precision, bias and total error are used. For that, the forward model is run 1000 times, each time with a different random number generator seed. This way there are 1000 different measurements vectors generated. The inversion model can then fit the parameters for each of those runs, generating an array with all the fitted values. For simplicity, only methane will be considered here. But the precision, bias and total error can be calculated for every fitted parameter. The retrieved methane concentration for each run can be organised in an vector **X**:

$$\mathbf{X} = \begin{bmatrix} x_1 CH_4 \\ . \\ . \\ . \\ x_{1000} CH_4 \end{bmatrix} \tag{3.12}$$

The best estimate of methane precision is the average value of the vector **X**:

$$\bar{x} = \frac{\sum_{i=1}^{1000} x_i}{1000} \tag{3.13}$$

The precision of methane retrieval is then defined as the standard deviation of **X**:

$$\sigma = \sqrt{\frac{\sum_{i=1}^{1000} (x_i - \bar{x})^2}{1000}} \tag{3.14}$$

The bias is the deviation of the best estimate to the actual methane concentration used in the forward model(x_{true}):

$$b = x_{true} - \bar{x} \tag{3.15}$$

The total error was added to have a metric that combine both bias and precision. It is a standard deviation from the true value instead of the sample mean:

$$Error = \sqrt{\frac{\sum_{i=1}^{1000} (x_i - x_{true})^2}{1000}} \tag{3.16}$$

4

Filter selection methods

A brute force approach would require testing all possible combinations of filters in order to find the best selection. However, there are 4374 simulated filters in the library. If 16 filters are to be selected, there would be $4374!/(4358!\ 16!)$ combinations, roughly 10^{45} combinations. This is much more than the roughly 10^{23} stars in the universe! And it may well be that the optimum number of filters to be used is not 16, opening up even more the amount of combinations possible. Thus better ways of navigating this vast space of possibilities were required.

Two approaches to select filters were assembled. The first approach is called the “gradient angles” and will be explained in Section 4.1. The second approach is called the “singular value” and will be explained in Section 4.2. Afterwards, both approaches were merged into one, which is explained in Section 4.3.

4.1. Gradient angles

This method is based on maximising the angle between the gradients of each filter. This method will first be explained with a simple case were only 2 parameters have to be fitted. It is latter expanded to the case where 7 parameters are to be fitted.

A given filter has a detector reading y in electrons at the detector that depends on 2 parameters. Here it is assumed that the parameters are only the concentration of CH_4 and a constant albedo. Thus y is a function of xCH_4 and Alb: $y = F(xCH_4, Alb)$. A given measurement y_{meas} for this filter is then a level curve of this function as depicted in Figure 4.1 . However y_{meas} has noise added to it and can vary between $y_{\text{meas}} + \epsilon$ and $y_{\text{meas}} - \epsilon$. Thus the region of solutions that could have generated this measurement is the region bounded by the dotted lines in Figure 4.1.

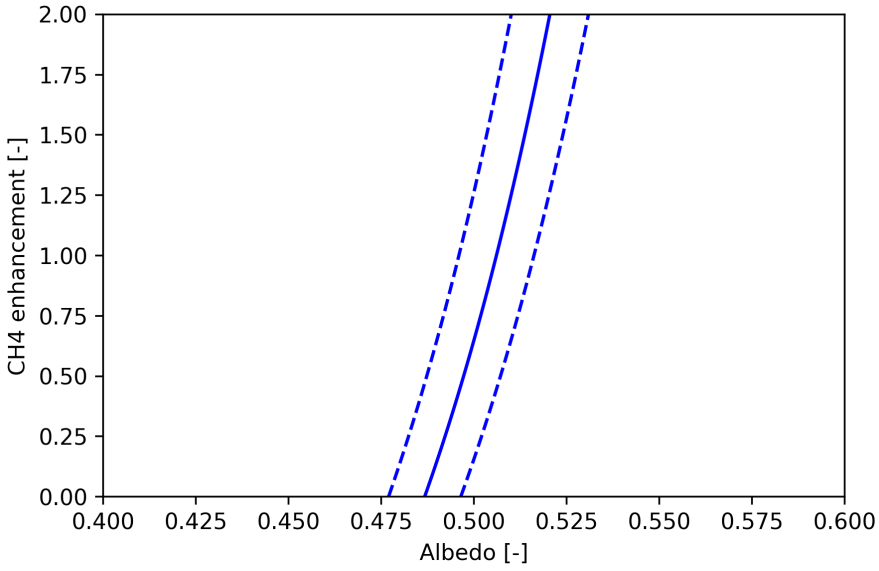

Figure 4.1: Region of solutions that could have generated a given measurement, given that there is noise in the measurement

The area of the solutions in Figure 4.1 is infinite, to limit this area another filter measurement has to be

added. This bounds the solution region to a finite area as in Figure 4.2. The idea of this method is that the precision of the inversion algorithm is related to the area of the bounded region. Thus minimising this area improves the precision.

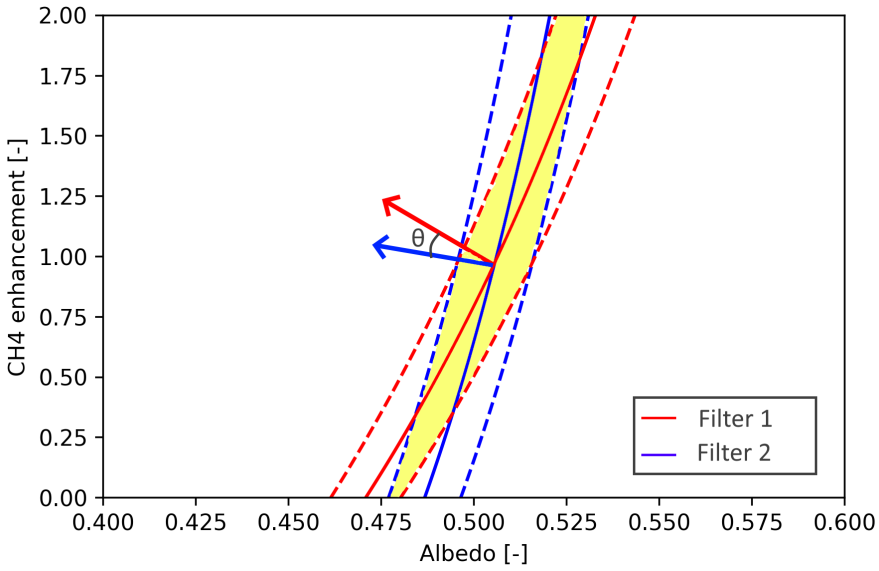

Figure 4.2: Region in yellow is bounded by two filter that could have generated a given pair of measurements. The gradient is normal to the level curve of each filter. The angle θ between the gradients is maximised in order to minimise the highlighted region.

The area is smallest when the curve lines of each filter are normal to each other. Furthermore, the gradient of a function is normal to its level curve, so minimising the cosine of the angle between the gradients of two curves will make the level curves as perpendicular as possible. Thus minimising the area.

This can then be expended to 7 dimensions. The procedure starts by picking the 2 filters whose cosine of the angle between their gradients is the smallest as possible, the angle is shown in Figure 4.2. These 2 filters define a 2 dimensional space in the 7 dimensional domain. The gradient of all the other filters can be projected onto the space defined by these 2 filters. The procedure after this is selecting the filter whose rejection to the space defined by the first 2 filters is the largest. The filter with the largest rejection is the most sensitive to the region that the first 2 filters can not cover.

After this the selection has 3 filters that span a 3 dimensional space on a 7 dimensional domain. The rejections and angles can be calculated again until a set of 7 filters that span the entire domain are selected. This entire procedure can be repeated to select sets of 7 filters that span the entire domain space and thus select as many filters as desired.

$$\nabla F_i(x_0) = \begin{pmatrix} \frac{\partial F_i(x_0)}{\partial xCH_4} \\ \frac{\partial F_i(x_0)}{\partial xH_2O} \\ \frac{\partial F_i(x_0)}{\partial xCO_2} \\ \frac{\partial F_i(x_0)}{\partial Alb_0} \\ \frac{\partial F_i(x_0)}{\partial Alb_1} \\ \frac{\partial F_i(x_0)}{\partial Alb_2} \\ \frac{\partial F_i(x_0)}{\partial Alb_3} \end{pmatrix} \tag{4.1}$$

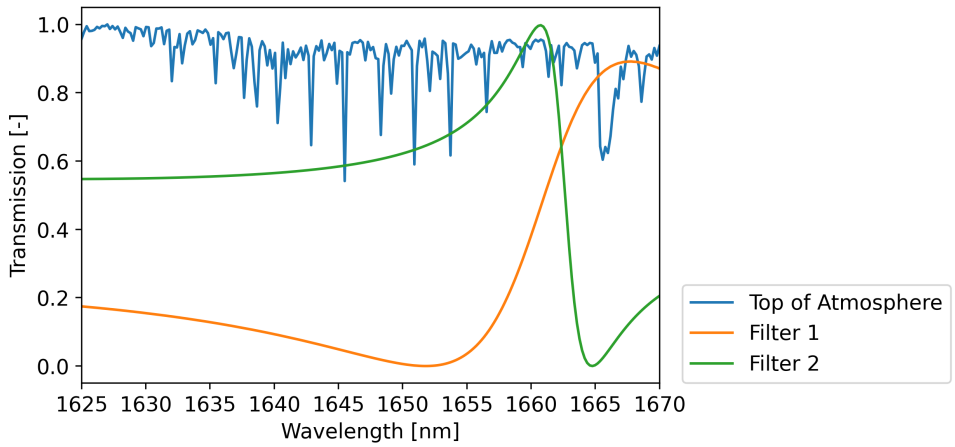

Figure 4.3: Two filters whose transmission allow different parts of the spectrum to reach the detector. Spectrum on top of the atmosphere is plotted in blue at the back as a reference.Thus they have different sensitivities to absorption lines in different regions of the spectrum.

The method starts by calculating the gradient of each filter with respect to the fitted parameters, as in Equation 4.1. Furthermore, the relation of $F(x)$ is defined as in Equation 3.9. In that equation only the sun radiance depends on the parameters. The integration and derivative operators are linear, so it can be rewritten as in Equation 4.2 for each parameter.

$$\frac{\partial F_i(x_0)}{\partial xCH_4} = \frac{\partial y_i(x_0)}{\partial xCH_4} = \int q_e t_e \varepsilon T_i(\lambda) \frac{\partial I_{ins}(x_0)}{\partial xCH_4} d\lambda \tag{4.2}$$

Thus the gradient of each filter depends on the gradient of the radiance that reaches the instrument, but each filter will select different parts of the spectrum. This is illustrated in Figure 4.3. For calculation purposes, the gradient of the radiance $\left(\frac{\partial I_{ins}(x_0)}{\partial x}\right)$ is first computed using the forward finite difference method and then Equation 4.2 is used to get the gradient of each filter.

After that, a matrix G is assembled that contains all gradients, as in Equation 4.3. The rows of this matrix can be normalised to get the matrix N with the directions of each gradient. The product of N with N^T gives then the inner product between all of the directions. A property of the inner product for two arbitrary vectors A and B is: $A \cdot B = |A||B| \cos\theta$ which gives the cosine of the angle between the two vectors. If the vectors are normalised the property can be simplified to $A \cdot B = \cos\theta$. So the matrix NN^T, contains the cosine of the angle between every possible selection of 2 vectors. The element with indices (0,0) will give the cosine between the filter 0 with itself, thus 1. And the element with indices (13,15) will give the cosine of the angle between the gradient of filter 13 and the gradient of filter 15.

$$G = \begin{pmatrix} \nabla F_0(x_0)^T \\ \nabla F_1(x_0)^T \\ . \\ . \\ . \\ \nabla F_{4374}(x_0)^T \end{pmatrix} \tag{4.3}$$

The pair of filter with the smallest cosine is picked, here denominated with the subscripts j and k.This is the same as picking the pair of filters with the biggest angle between them, due to the angle being always between 0 and $\pi/2$. After that, an orthonormal representation of the space spanned by the gradient of these filters needs to be calculated. This allows for the calculation of the rejection of the

gradients of other filters to this space. This is done by calculating the projection of the second filter onto the first one and then subtracting it from the gradient. This, in turn, requires the normalised gradient of the first selected filter $N_1 = \frac{\nabla F_j(x_0)}{||\nabla F_j(x_0)||}$ and Equation 4.4.

$$N_2 = \nabla F_k(x_0) - \nabla F_k(x_0) \cdot N_1 \; N_1 \tag{4.4}$$

N_2 and N_1 are then assembled together into the matrix $O_N = \begin{pmatrix} N_1^T \\ N_2^T \end{pmatrix}$. With this matrix it is possible to quickly calculate the rejection of any other gradient l to this space with Equation 4.5.

$$N_l = \nabla F_l(x_0) - (\nabla F_l(x_0)^T \; O_N^T \; O_N)^T \tag{4.5}$$

After this, the filter whose gradient has the rejection with the largest magnitude is selected. The rejection of this filter can then be normalised and added to the matrix O_N. This process can be repeated until 7 filters that span the entire domain are selected. The entire selection procedure is summarised in Figure 4.4. And can be repeated to select new sets of 7 filters.

Although this method provides good filter sets, it does come with several drawbacks. First, the pool of filters options is finite thus each new set of 7 filters are less likely to perform as well as the first ones; another downside is that the selection of the first 2 filters does not consider the length of the gradient, and the length contributes to reducing the volume of the solution space; And lastly selecting sequentially the filters with the largest rejection to the space of already selected filters is not proven to guarantee that the final solution will be the most spread out as possible.

4.2. Singular values

Another method selects filters based on singular value optimisation. The forward model can be summarised with an equation $\vec{y} = \mathbf{F}(\vec{x})$, where $\vec{y}$ are the measurements in the instrument and $\vec{x}$ are the parameters that are to be fitted. In this case it is assumed that the solar zenith angle and the viewing zenith angle are known beforehand. Thus the variables are only the concentration of the gases and the reflection of the surface.

The instrument is to operate in the 1625nm to 1670nm wavelength range. In this range, some of the gases that have absorption lines are CH_4, H_2O and CO_2. So the concentration of these gases are to be retrieved in the algorithm. Furthermore, if a 3rd degree polynomial is used to model the albedo, then $\vec{x}$ has to contain 4 terms for albedo, each for one of the polynomial coefficient (Alb_0, Alb_1, Alb_2 and Alb_3). Other polynomial orders could be used for the albedo. The structure of $\vec{x}$ with a cubic albedo is shown in Equation 4.6.

$$\vec{x} = \begin{pmatrix} xCH_4 \\ xH_2O \\ xCO_2 \\ Alb_0 \\ Alb_1 \\ Alb_2 \\ Alb_3 \end{pmatrix} \tag{4.6}$$

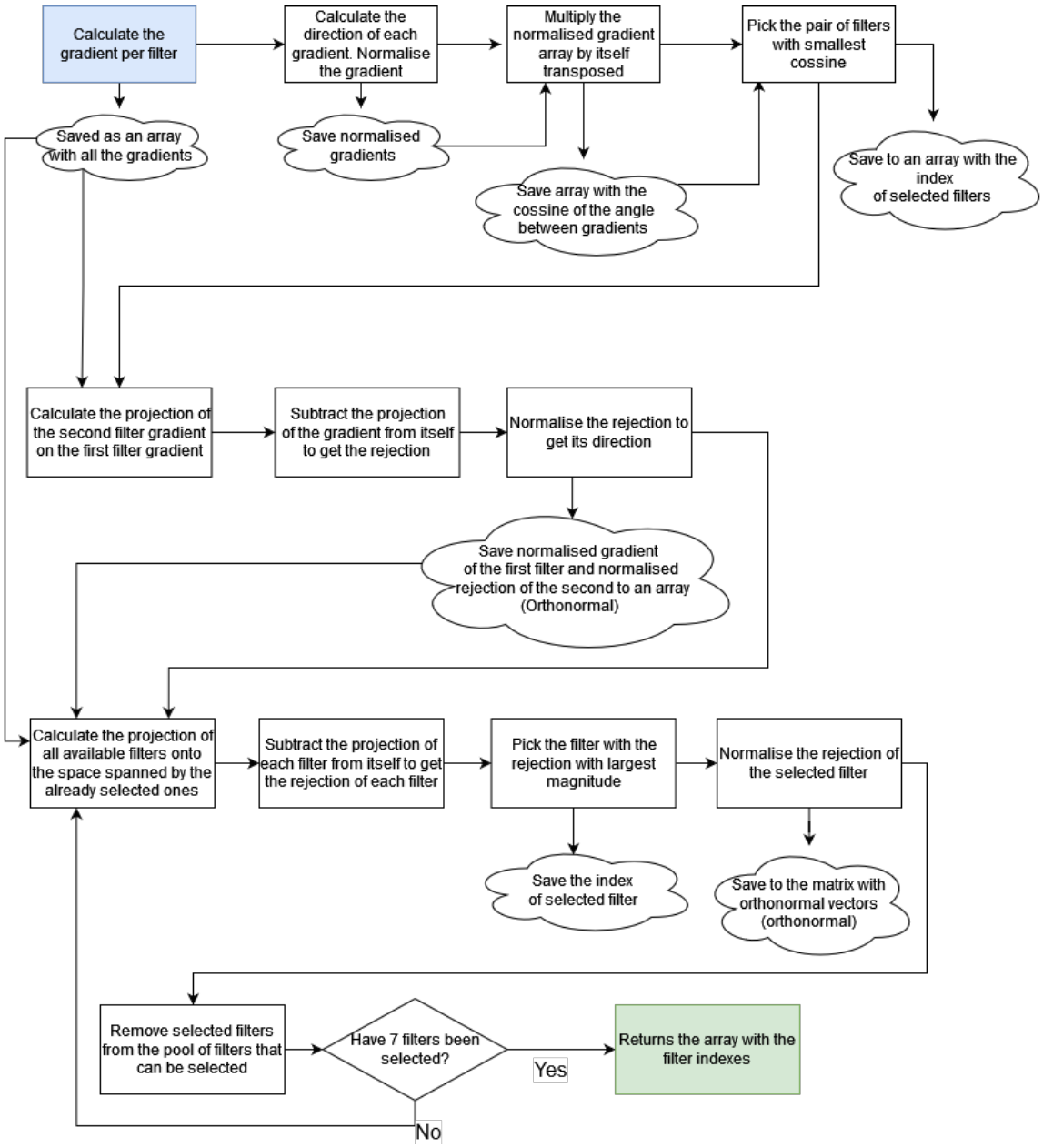

Figure 4.4: Flow of the method to select filters based on their gradients trying to make them as spread out as possible.

The forward relation $\vec{y} = \mathbf{F}(\vec{x})$ can be linearised about a point $\vec{x}_0$:

$$\vec{y} = \mathbf{F}(\vec{x}_0) + \frac{\partial \mathbf{F}(\vec{x}_0)}{\partial \vec{x}}(\vec{x} - \vec{x}_0) \tag{4.7}$$

From this relation it is possible to separate the part that depends only on $\vec{x}$, calling it $\tilde{y}$:

$$\tilde{y} = \frac{\partial \mathbf{F}(\vec{x}_0)}{\partial \vec{x}}\vec{x} \tag{4.8}$$

The relation of $\tilde{y}$ and $\vec{x}$ is linear and can be solved by doing singular value decomposition of the matrix $\frac{\partial \mathbf{F}(\vec{x}_0)}{\partial \vec{x}}$. Taking the singular value decomposition as:

$$\frac{\partial \mathbf{F}(\vec{x}_0)}{\partial \vec{x}} = \mathbf{U}\Sigma\mathbf{V}^T \tag{4.9}$$

Where the columns of U are the left singular vector u_i, the columns of V are the right singular vector v_i and the diagonal entries of matrix Σ are the singular values σ_i of the matrix $\frac{\partial \mathbf{F}(\vec{x}_0)}{\partial \vec{x}}$. The value of $\vec{x}$ is then:

$$\vec{x}_t = \sum_{i=0}^{6} \frac{u_i^T \tilde{y}}{\sigma_i} v_i \tag{4.10}$$

Where $\vec{x}_t$ is the true value of $\vec{x}$. If there is an error $\tilde{e}$ on $\tilde{y}$, this will be propagated to $\vec{x}$ as:

$$x = \sum_{i=0}^{6} \left(\frac{u_i^T \tilde{y}}{\sigma_i} v_i + \frac{u_i^T \tilde{e}}{\sigma_i} v_i \right) = x_t + x_e \tag{4.11}$$

Where $\vec{x}_e$ is the error on $\vec{x}$, which is equal to the second term under the summation. If the matrix $\frac{\partial \mathbf{F}(\vec{x}_0)}{\partial \vec{x}}$ changes, $\vec{x}_t$ will still obey the relation from Equation 4.10. On the other hand, $\vec{x}_e$ will change depending on the singular values σ_i. Larger singular values will reduce the value of $\vec{x}_e$, reducing the propagation of errors from the measurement to the retrieved state $\vec{x}$.

The method “singular values” therefore aims to improve the singular values of the matrix $\frac{\partial \mathbf{F}(x_0)}{\partial x}$. This method is simpler than the gradients however it takes more computational effort. It starts by calculating the gradient of each filter $\frac{\partial F_i(x_0)}{\partial x}$ as was done in Equation 4.2. The gradient for every filter is then saved to assemble the matrix $\frac{\partial \mathbf{F}(x_0)}{\partial x}$ based on the filters that are to be analysed. The flow in Figure 4.5 is then followed.

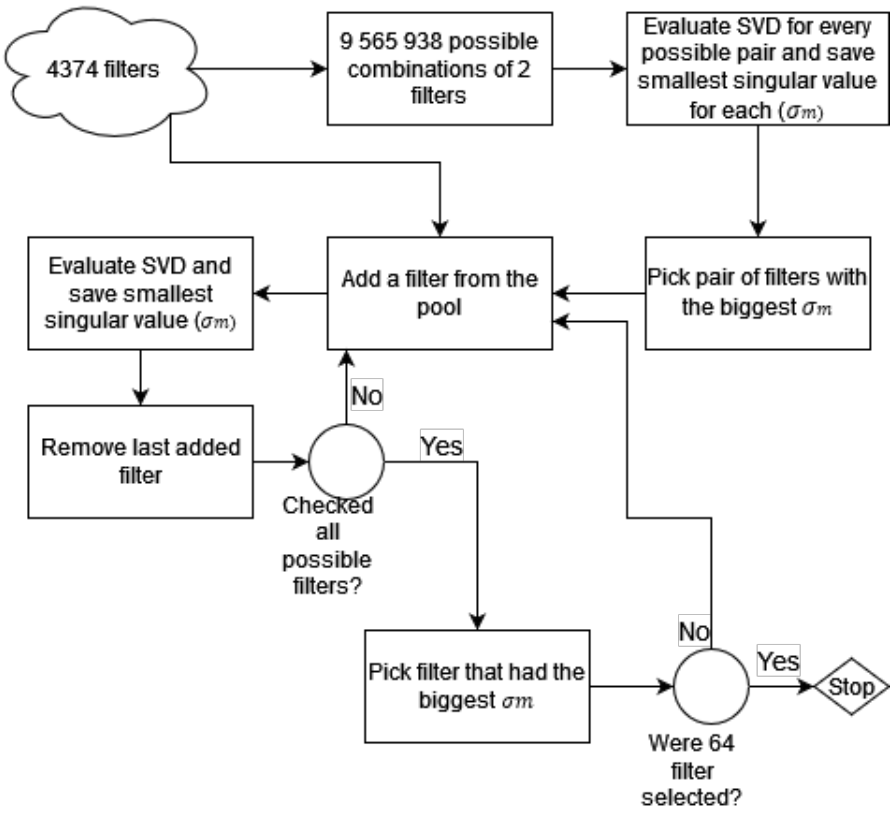

Figure 4.5: Flow of the selection based on singular value decomposition

It starts by evaluating the singular value for every possible pair of filters. This totals to $4374^2/2 = 9\ 565\ 938$ evaluations of singular values. The smallest singular value of each pair is saved, and the pair that had the biggest smallest singular value is picked, as explained in Figure 4.5.

After that another filter is added to the selection and the singular values reevaluated. This is evaluated for all other filter that can be added to the selection. The filter that best improves the smallest singular

value is selected. This is repeated to add new filters until the required amount of filters have been selected. In the simulations this was limited to 64 filters.

The advantage of this method compared to the gradient angles are: it considers the length of the gradients on the first two filters; and it can add as many filters as required, not being limited by multiples of 7. However, the downsides are: the path taken aims to improve the singular values but it does not guarantee that the selection is the one that would have the best singular values possible; This method is more computationally expensive because of the over 9 million evaluations of singular values that have to be done initially.

4.3. Selecting filters based on singular value decomposition and gradients

The first two filters that were picked by the gradients method could not include the length of the gradients. So the merger of method starts by picking the pair of filters as was done for “singular value”. This is followed by selecting filters using the gradients method until the number of filters equals the number of parameters being fitted. This way it is guaranteed that the filter selection can measure all parameters.

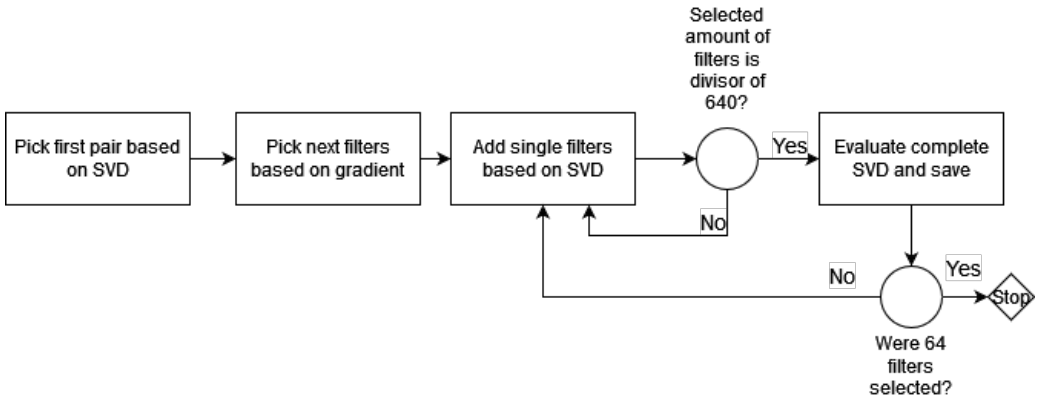

Figure 4.6: Flow of the selection based on singular value decomposition and gradients

After that, new filters are added based on the one that best improves the smallest singular value of the set. This is done until 64 filters are selected. The singular value of the matrix that relate the parameters to 640 measurements is evaluated every time the filter set reaches a divisor of 640 (8, 10, 16, 32 and 64). Adding more filters means that there will be less data points for each filter, thus at some filter set size the smallest singular value decreases again. This way the optimum filter set size for each case could be chosen.

5
Filter selection comparisons

The objective of this chapter is to answer the sub-question: “How does the instrument perform when considering the concentrations of other gases and spectral dependency of the surface reflectance?”. This will be done while comparing the performance of two filter selection methods: one made using an evolutionary algorithm and the other made using the method presented in Chapter 4. First, the influence of other gases that have absorption lines in the wavelength range of the instrument will be investigated in Section 5.1. It will be followed by investigating the effect of spectrally dependent surface reflectance in Section 5.2. Then the combined effect of other gases and spectrally dependent albedo is investigated in Section 5.3. The same aspects are then investigated in the case where the wavelength range used by the instrument would be expanded from $1625-1670nm$ to $1590-1670nm$. This expansion includes more absorption lines of carbon dioxide, thus improves the retrieval of that gas. Finally, all sections are summarised in Section 5.5.

This chapter uses the results of many different runs of the instrument simulator. All estimations of precision, bias and error in this chapter were done by running 1000 times the retrieval algorithm, explained in Chapter 3. Furthermore, the solar zenith angle is always set to 70 degrees and the albedo is set to 0.15, when not stated otherwise.

5.1. Influence of other gases

A prior selection of filters for the project was made using an evolutionary algorithm. It was made in collaboration with the Leiden Institute of Advanced Computer Science (LIACS) and considered only methane and albedo as fit parameters during the optimisation. In reality, there are absorption lines of other gases in the wavelength range used by the instrument. And the effect of these gases will be investigated here.

The method explained in Chapter 4 was also used to select filters with methane and a constant albedo as parameters. This can be directly compared with the evolutionary algorithm selection since it is the same scenario that it was optimised for.

Table 5.1: Precision, bias and total error for the instrument using the evolutionary algorithm selection and the new method. Fits only methane and a constant albedo.

	Evolutionary algorithm			New method		
	Precision	Bias	Error	Precision	Bias	Error
Methane	1.11%	0.03%	1.12%	0.91%	0.01%	0.91%

Table 5.1 shows that the new method finds a selection that performs better than the evolutionary algorithm at a fraction of the computational effort. This is due to only 2 filters being necessary to retrieve 2 parameters (methane and albedo). The new method begins by checking the pair of filters that outputs the best singular values, thus it checks all combinations of 2 filters that measures well the entire parameter domain. It can check all the options in less than 10 minutes and outputs the best combination. Reaching combinations that the evolutionary did not reach by chance.

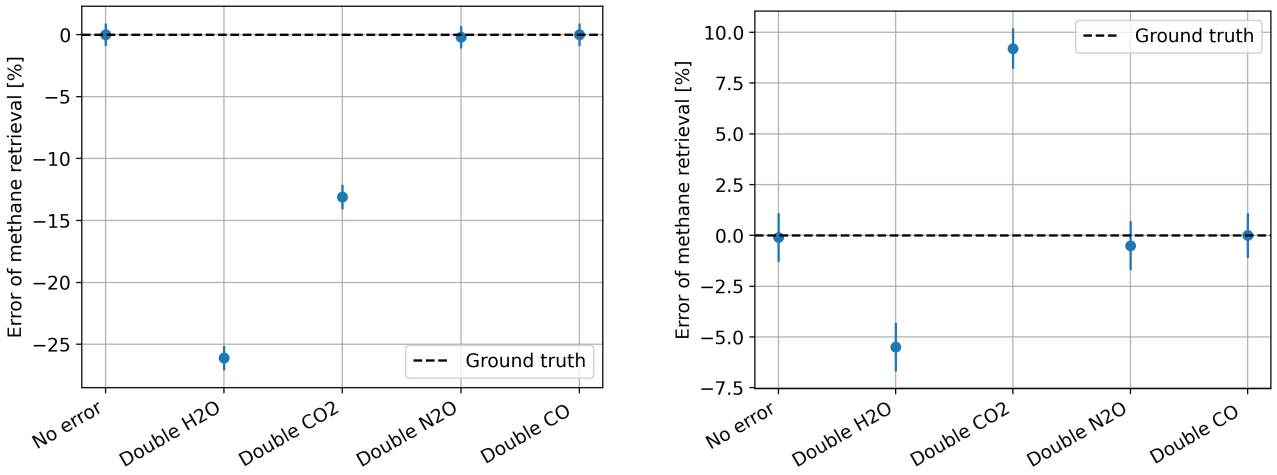

(a) SVD and gradients **(b) Evolutionary Algorithm**

Figure 5.1: Methane retrieval for cases that assume double the concentration of different gases than what is used in the forward model.

Next, the effect of other gases was investigated. This was first done by investigating the impact of assuming the wrong concentration of each gas. The inversion algorithm was given double the concentration of a gas than what was used in the forward model. This introduces a bias in the retrieval of methane, the more important a gas is, the bigger the bias will be. This was done for water vapour, carbon dioxide, nitrous oxide and carbon monoxide.

The bias and the precision of each experiment run are plotted in Figure 5.1. The dot is the average retrieval for that experiment and the bars are the precision. The further away the dot of a experiment is from the dotted line, the bigger the bias is. As a baseline, the first experiment retrieved the parameters for the case where the concentration of the other gases is known exactly, that is the same result as in Table 5.1. Thus the baseline is named “No error” in the plot.

For both filter selection methods the bias introduced by wrongly assuming the concentration of CO_2 and H_2O were very significant. This indicates the necessity of better estimates of their concentrations. To some extent, N_2O also affects the retrieval of methane but much less significantly than CO_2 and H_2O. Lastly, neither selections are affected by CO. This is due to the absorption lines of N_2O being very weak in this wavelength range and the absorption lines of CO are even weaker. Therefore, water vapour, carbon dioxide and nitrous oxide may be relevant for methane retrieval and carbon monoxide can be neglected.

The bias due to the wrong assumption of the gas concentrations depend on the selected filters, as can be seen in Figure 5.1. In the evolutionary algorithm selection, the wrong concentration of CO_2 and H_2O introduce a positive and a negative bias respectively. This is due to the evolutionary algorithm mainly using the absorption lines of methane around 1665 nm to retrieve its concentration, as shown in Figure 5.2a. It selected many filters that has a peak of transmission around that wavelength and uses that information to retrieve methane. The other filters are used mainly to retrieve the albedo of the surface.

In Figure 5.2b it can be seen that the absorption lines of CO_2 in this wavelength range mainly affect the filters that are used for the albedo retrieval. The inversion algorithm is using a higher concentration of CO_2 than there was in the scene, thus it compensates it by fitting a higher brightness or higher albedo. This is later compensated by fitting more methane than there is in the scene, introducing a positive bias.

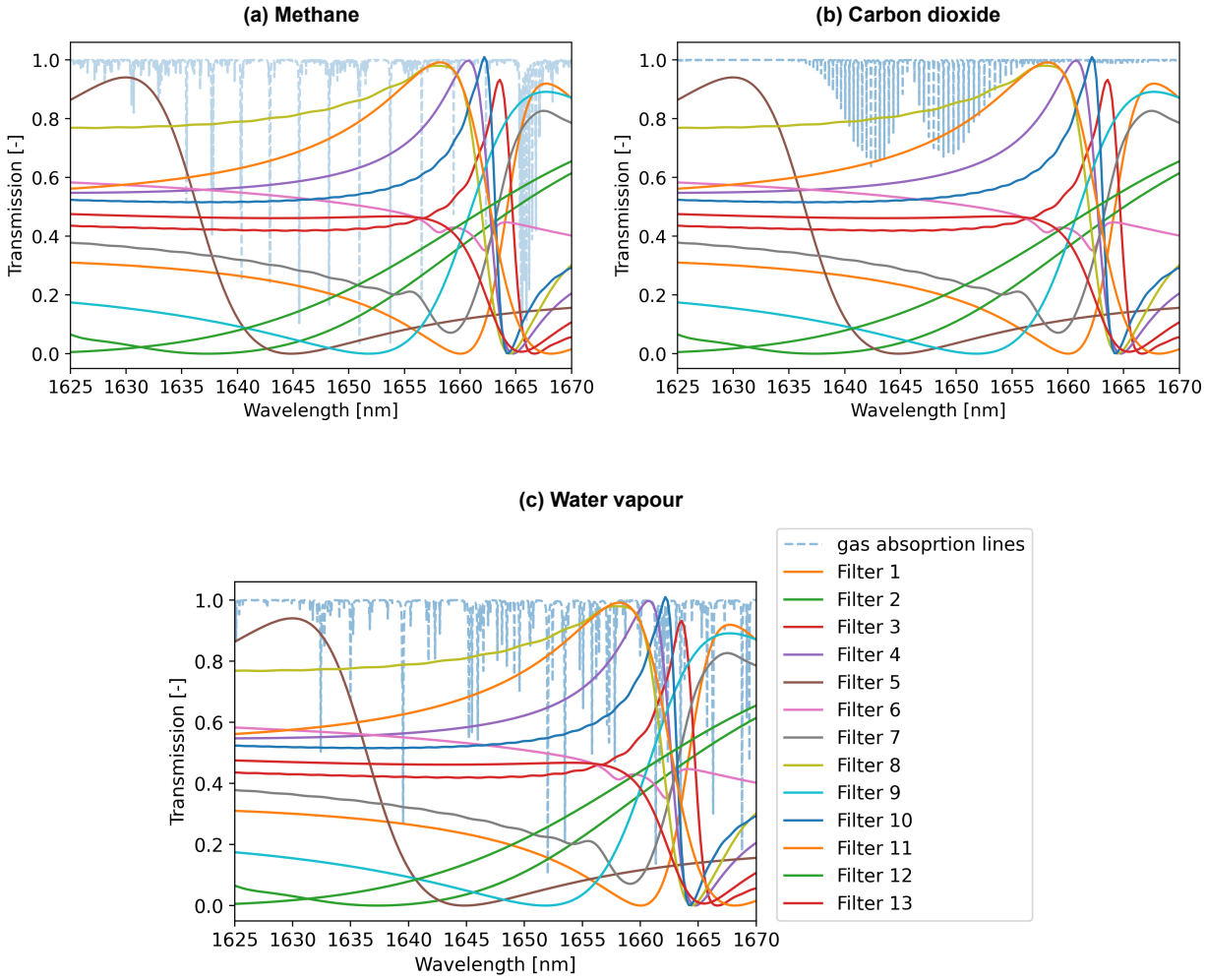

Figure 5.2: Transmission of the filters selected by the evolutionary algorithm, each represented by a different colour. The absorption lines of methane, carbon dioxide and water vapour are plotted on the background.

Water vapour has absorption lines more spread out over the spectrum. The impact of assuming double the concentration is compensated by fitting less methane than there was in the scene. Due to it also impacting the wavelength range that was used to retrieve methane.

The selection made using the gradients and SVD method used more the absorption lines of methane from 1630 nm to 1655 nm, as seen in Figure 5.3. This made the bias due to CO_2 being negative, similar to what happens with water vapour. Thus the algorithm compensated the error made in the concentration by fitting less methane.

One way of improving the estimate of CO_2, H_2O and N_2O is to retrieve them as fit parameters as well. Thus the impact of including all possible combinations of these gases as fit parameters was tested. The first test done was running an experiment that uses the wrong concentration of CO_2, H_2O and N_2O in the inversion model and does not fit them. This makes it easier to see the impact of fitting a certain gas later on, as retrieving its correct concentration will reduce the bias. Thus each gas that can be retrieved well will bring the baseline case closer to the ground truth. In Figure 5.4, the effects of fitting each of the cited gases can be seen. Furthermore, the method based on SVD and gradients was used considering each new parameter that was added. For example: water vapour, methane and albedo were considered when selecting filters, in the case that fits these parameters. Thus each

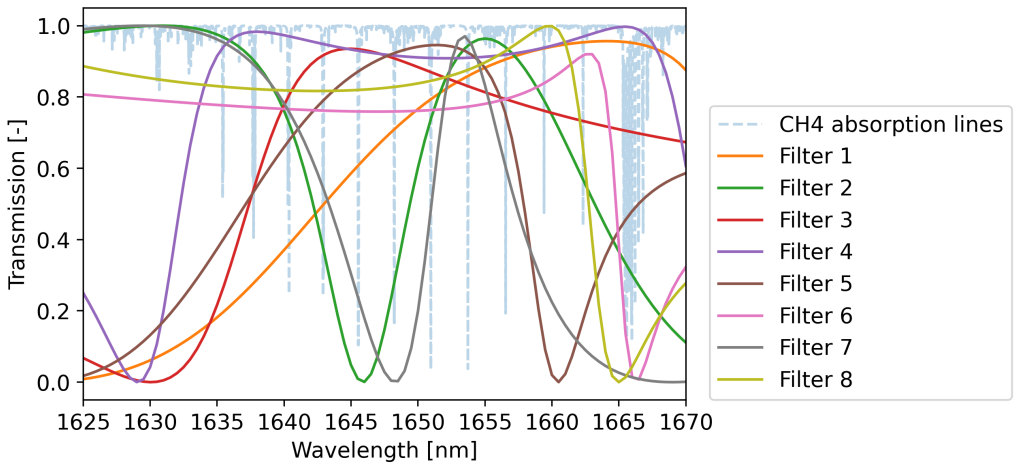

Figure 5.3: Transmission of filters selected using the ”SVD an gradients” method, each colour is a different filter. The absorption lines of methane are plotted as dotted lines in the background.

case in Figure 5.4a has different filter selection.

Adding water vapour as a fit parameter increased the bias when compared to the “Fit just CH4” case, seen in Figure 5.4b. This is due to the bias caused by water vapour being negative whereas for carbon dioxide it is positive. So when both bias are present they compensate for each other. Fitting water vapour removed the negative bias caused by it, thus increasing the already positive bias of the baseline case. A similar effect can be seen when just carbon dioxide was included as a fit parameter, the positive bias due to CO_2 was removed and the total bias became negative.

The case in Figure 5.4 that has the smallest bias is when just H_2O and CO_2 are fitted, besides methane. N_2O has to few absorption lines in this spectrum. Retrieving it becomes unstable, thus the precision and bias for methane becomes worse, as can be seen in Figure 5.4.

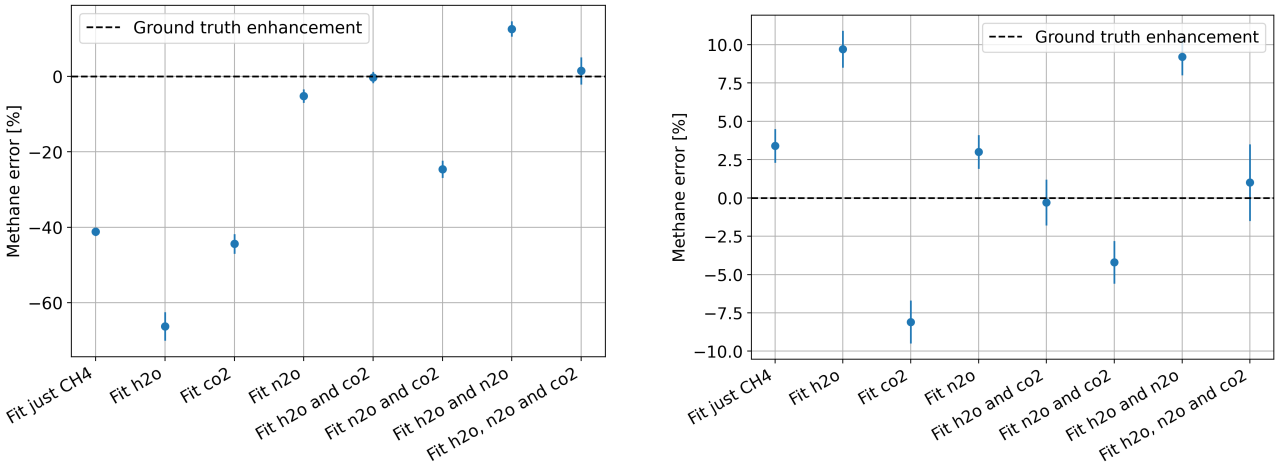

(a) SVD and gradients **(b) Evolutionary Algorithm**

Figure 5.4: Results of experiments used to evaluate the impact on the methane retrieval when fitting H_2O, CO_2 and/or N_2O.

5.2. Influence of spectrally dependent albedo

The reflectance of the surface of Earth can also vary with wavelength. This spectral dependence of the reflectance can cause the inversion algorithm to overestimate or underestimate the concentration of methane, effectively introducing a bias. The reflectance is then modelled as a polynomial as in

Equation 5.1.

$$R(x) = c_0 + c_1 x + c_2 x^2 + c_3 x^3 + c_4 x^4 + c_5 x^5 + c_6 x^6 \tag{5.1}$$

The inversion algorithm could then be used to retrieve the coefficients of Equation 5.1. This is similar to what was done in Section 5.1, but in those cases only c_0 was retrieved and the other coefficients were assumed to be zero.

The forward model needs some data to use as the ground truth for the spectrally dependant albedo. Two materials were chosen from the ECOSTRESS library: olive green gloss paint, due to showing significant spectral dependency, and asphalt shingles for being a common construction material. Their reflectance are shown in Figure 5.5.

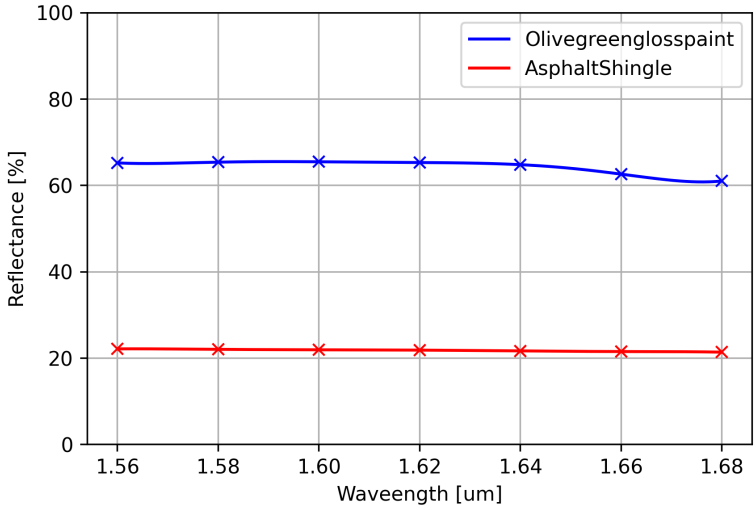

Figure 5.5: Reflectance of materials used for spectral dependence of albedo analyses.

The inversion algorithm has to retrieve the coefficients used in the forward model. It could use just the coefficient c_0 from Equation 3.8 and assume the others are zero. However, this would not approximate well the curves in Figure 5.5. Thus the effect of adding extra coefficients was investigated.

As the inversion algorithm retrieves more terms, its precision decreases. However, the bias should improve. This happens because the model in the inversion algorithm gets closer to what's used in the forward model, especially when they use a similar number of coefficients for the albedo. Also, the total error is a combination of both bias and precision. Thus there should be an amount of retrieved albedo coefficients that minimises the error, by balancing the loss in precision with the gain in the bias.

When using the evolutionary algorithm selection, there is a significant bias if just a spectrally constant albedo is retrieved, as seen in Figure 5.6. The bias is reduced as more albedo coefficients are added, however the precision is deteriorated, as expected. Also, in Figure 5.6b there is a jump in the precision when the 4th coefficient is added (c_3 in Equation 5.1). This is due to the retrieval of this coefficient being very unstable with the filters selected with the evolutionary algorithm. These effects are mainly due to this spectral dependency not being considered when the filters were selected by this method.

The evolutionary algorithm could be rerun to select new filter sets based on the number of albedo terms that have to be fitted. However, this would take weeks or even months to run. Therefore, the

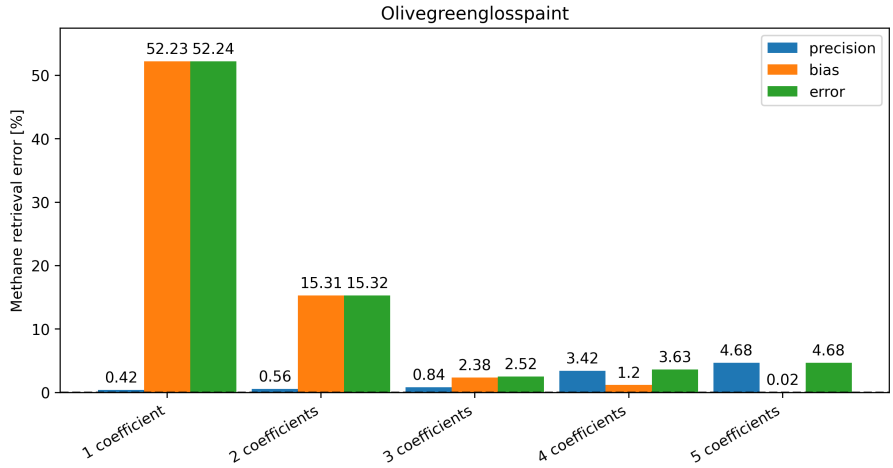

(a) Olive green gloss paint

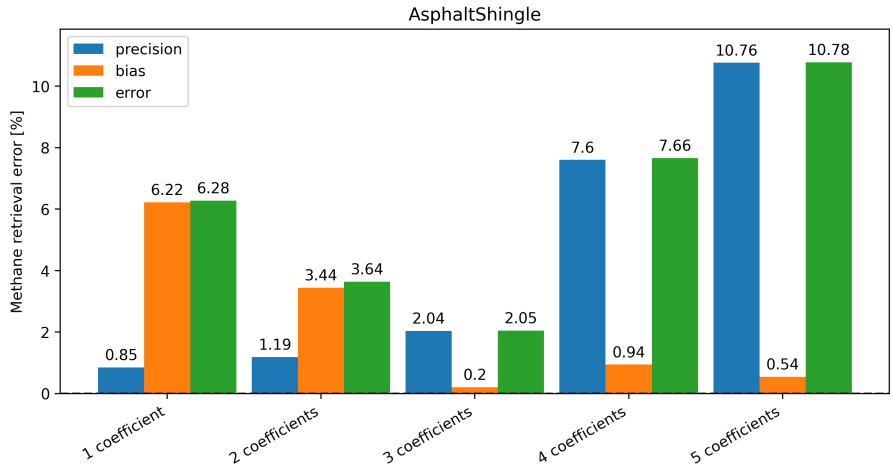

(b) Asphalt shingles

Figure 5.6: Evolutionary algorithm selection, methane retrieval when adding more coefficient terms to the albedo polynomial.

method explained in Chapter 4 was used. This methods might find filters that can better retrieve higher order coefficients for the albedo polynomial. This would reduce the penalty in the precision for retrieving more coefficients. So the selection was made considering how many coefficients would have to be retrieved. For instance, if 2 coefficients are fitted, the filter selection also considered those 2 coefficients. The same hold for all cases in Figure 5.7. Thus once again each case has a different filter selection.

The same materials that were used for the evolutionary algorithm analyses, shown in Figure 5.5, were used for the new filter selection: Asphalt shingle and the green gloss paint.

In Figure 5.7, there is a significant bias when only 1 albedo coefficient is fitted. This is due to the albedo used not being spectrally constant. Increasing to a linear albedo polynomial (2 coefficients) already reduces the bias significantly for both materials. More importantly, the degradation in the precision is much smaller than for the Evolutionary Algorithm filter selection. This is due to the filters being selected to measure these coefficients and thus retrieving them better. The impact of errors in these coefficients onto methane consequently becomes smaller.

In this simplified case, H_2O and CO_2 do not have to be retrieved and the optimum model for the surface reflectance is linear (2 coefficients). However this may not be true once the effect of the gases are also factored in.

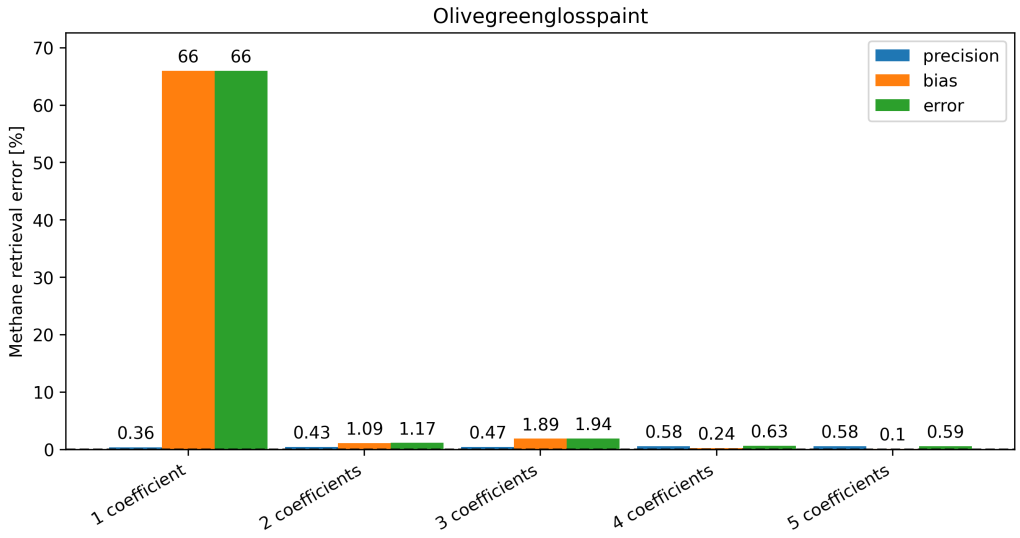

(a) Olive green gloss paint

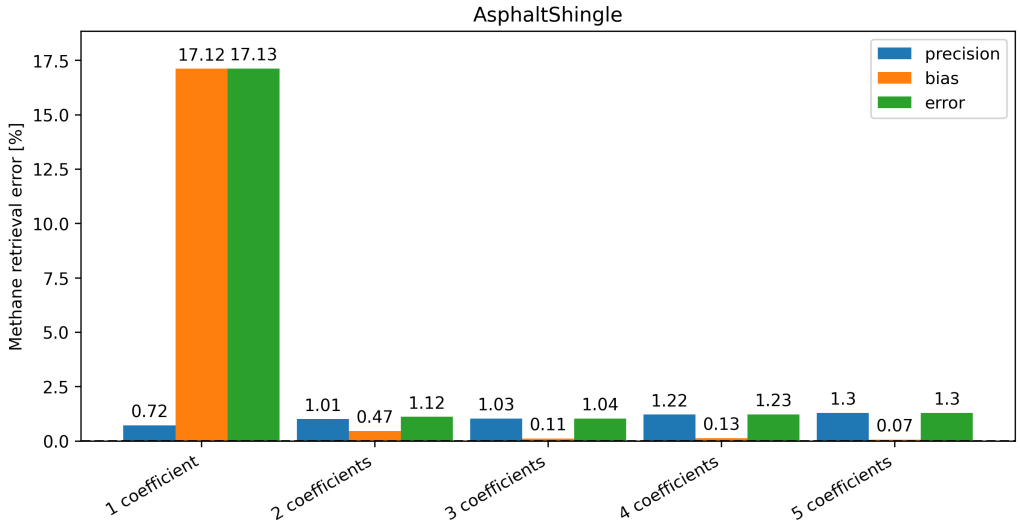

(b) Asphalt shingles

Figure 5.7: Methane retrieval when adding more coefficient terms to the albedo polynomial and using the new filter selection method.

Lastly, the olive green gloss paint is an extreme case of albedo dependence. So the analyses with the asphalt shingle will likely be more representative of a real scene. In real scenes the reflectance of many materials are combined, which will lead to less spectral variation. Thus the impact of the spectral dependency will be smaller than what is seen in Figure 5.7 and Figure 5.6.

5.3. Influence of albedo and gases

As mentioned, the optimum number of coefficients for modelling the surface reflectance might be different than what was found in Section 5.2. This is due to the degradation in the precision caused by fitting other gases and the one caused by the albedo coefficients not being considered together. Thus this section adds the influence of the gases and the spectrally dependant albedo into the same simulation performance, to get the total impact.

The precision of the retrieval of methane degrades further when also fitting water vapour and carbon dioxide, as can be seen in Figure 5.8. This is due to more fit parameters being retrieved with the same

amount of measurements. This in turns changes the number of coefficients where the total error is minimum. In Figure 5.8b the optimum number of coefficients was 3 (quadratic polynomial).

(a) Asphalt shingles without fitting H_2O and CO_2

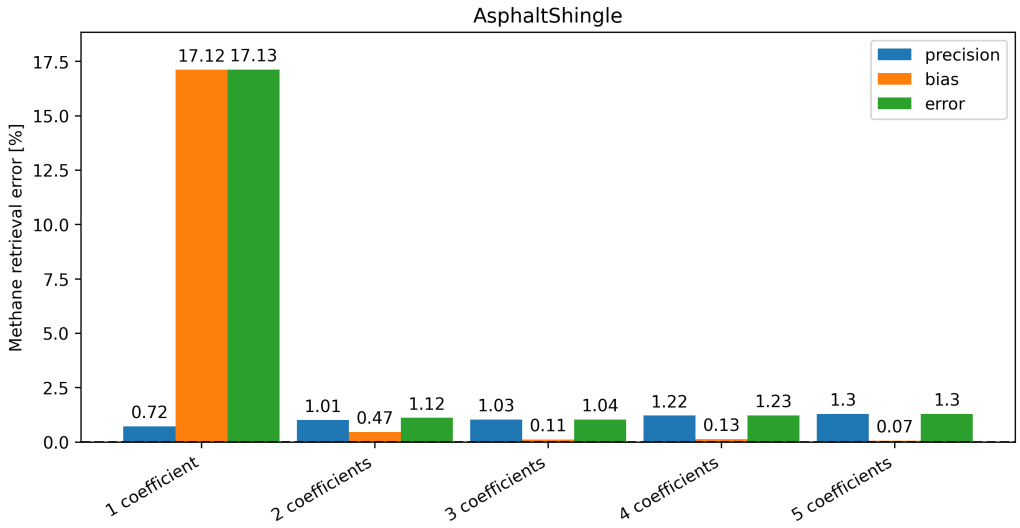

(b) Asphalt shingles also fitting H_2O and CO_2

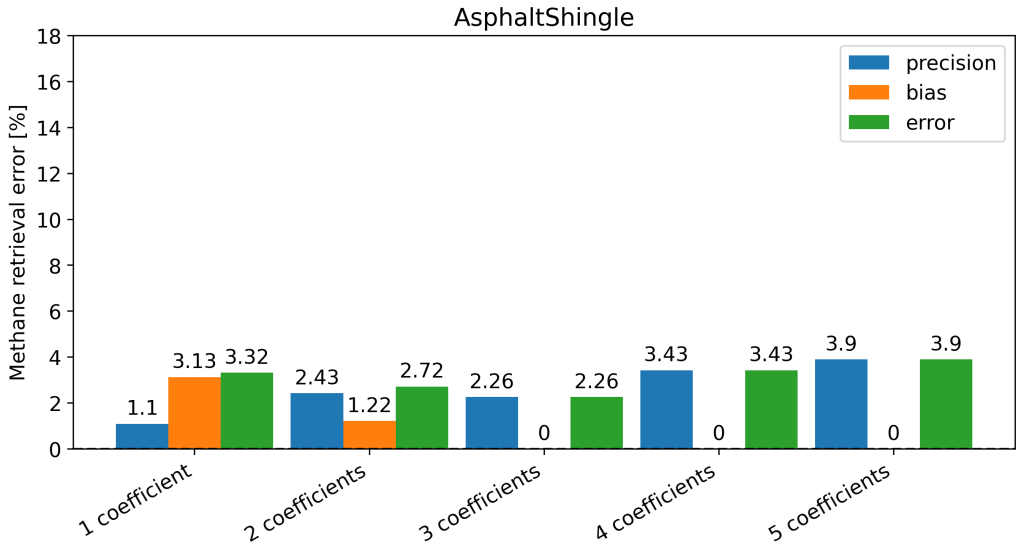

Figure 5.8: Methane retrieval when using the new filter selection method, adding more coefficient terms to the albedo polynomial. Effect of also including H_2O and CO_2.

The final impact of considering both the spectrally dependant albedo and the gases is just the further degradation of the precision. In the case where 3 polynomial coefficients are used for modelling the albedo in Figure 5.8, the precision degraded from 1.03% without fitting other gases to 2.26% with other gases. Roughly a two fold degradation.

5.4. Expansion of wavelength range

The light that traverses the atmosphere is also scattered. This scattering introduces a bias in the retrieval of the gases, however the bias affects both carbon dioxide and methane measurements the same way [29]. Thus if the concentration of one of these gases is known for a scene, then the bias introduced by scattering can be compensated for. For instance, if the concentration of carbon dioxide

is know to be 400 ppm and the instrument measures 410 ppm, there is a bias of 2.5% introduced by scattering and other effects. The retrieved concentration of methane can then be divided by 1.025 in order to remove the influence of theses effects. This method is called the proxy method.

However, in order to be able to use the proxy method the instrument must have comparable bias and precision for both methane and carbon dioxide. In order to improve the retrieval of carbon dioxide, this sections explores expanding the wavelength from 1625- 1670nm to 1590 - 1670 nm such that more absorption lines of CO_2 are included. The same steps as in the previous sections are followed in order to check if all findings remain true.

5.4.1. Constant albedo fitting and gas effects

A similar analysis as in Section 5.1 is performed to asses the sensitivity for prior knowledge mistake, where the ground truth concentration of the gases are doubled, see Figure 5.9. In this scenario the precision is a much smaller, due to the increased SNR caused by the expansion of the wavelength range. The total error is therefore either very small or completely dominated by the bias. As expected, the expansion of the wavelength range made the instrument more sensitive to changes in CO2, but it also remains sensitive to water vapour. The effect of N2O and CO remain small. Therefore, for good performance the retrieval algorithm should again include H2O and CO2.

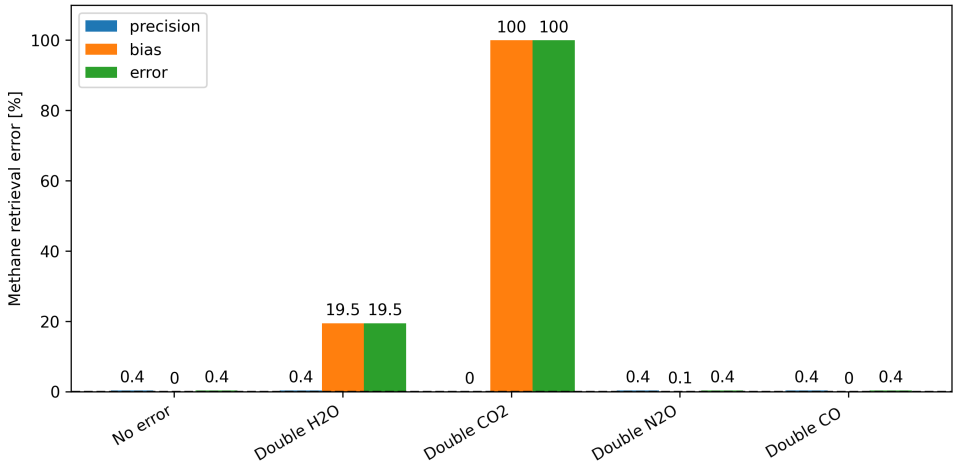

Figure 5.9: Methane retrieval for cases that assume double the concentration of different gases than what is used in the forward model, extended wavelength range. Absolute value of bias is plotted.

The cases that fit other gases is shown in Figure 5.10. All the cases that do not fit CO_2 have an extreme bias in the methane retrieval. Also, once again fitting nitrous oxide did not improve the retrieval of methane. Thus the optimum case requires fitting water vapour and carbon dioxide.

5.4.2. Changing albedo terms and fits methane only

The analyses proceeded once again with the effect of adding more albedo coefficient as fit parameters, and the only gas fitted is methane. This is done to evaluate if the assumptions hold for both wavelength ranges (1625-1670nm and 1590-1670nm). For all materials, the precision improves compared with the original wavelength range. However, the bias caused by the spectrally dependant albedo increases due to the wavelength range almost doubling. This can be seen in Figure 5.11.

However, the minimum error still occurs with 2 albedo coefficients. Furthermore, the total error for methane retrieval does not reach the same level as in Figure 5.7 wavelength range, due to the in-

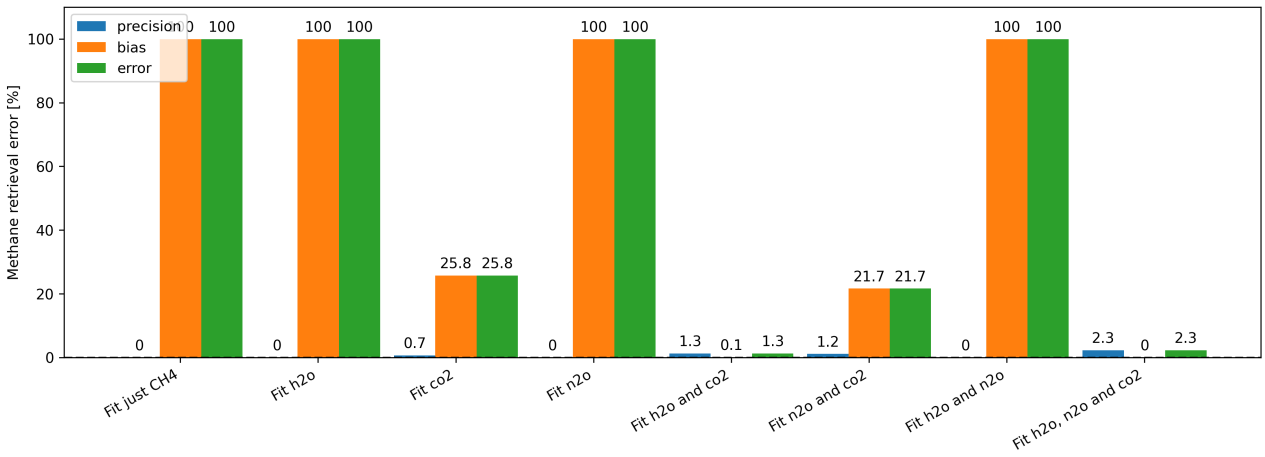

Figure 5.10: Methane retrieval when adding other gases as fit parameters and using the extended wavelength range. If the gas is not fitted, their concentration is assumed as double of the concentration used in the forward model. Absolute value of bias is plotted.

creased bias.

5.4.3. Comparison of performance with changing albedo terms, fitting CH_4, H_2O and CO_2

Finally, the extension of the wavelength range can be compared while fitting the gases and different number of albedo polynomial coefficients, shown in Figure 5.12. Just as was observed in the case where only methane was fitted, there is a degradation in the total error for methane when the wavelength range is expanded. This is once again due to the bigger influence of the spectral dependence of albedo. However, the total error for CO_2 drastically improves, as shown in Figure 5.12.

All in all, the best case to retrieve just methane would be the initial wavelength range. However, if methods to reduce the bias caused by scattering and stray-light are to be used then the extended wavelength range is preferred.

The number of albedo coefficients that minimises the methane precision is 3 for both wavelengths. However, the extended wavelength range is more affected by the spectral dependency.

5.5. Performance final comments

The performance of the inversion algorithm when retrieving methane depends highly on the concentration of water vapour and carbon dioxide, because there are also absorption lines of these gases in the observed spectrum. The fitting of these gases help reduce the bias in the retrieval of methane due to removing errors in assuming their concentration. However, they will still introduce a bias due to the error in the fitting of these gases. This is due to the gases having less sensitive absorption lines in the wavelength range than methane has.

The spectral dependency of the surface reflectance can also introduce a large bias in the retrieval of methane. This is due to it making the lines seem deeper in one part of the spectrum than in others. This can be mitigated by also retrieving the reflectance as a polynomial. The optimum number of polynomial coefficients to be used for albedo tends to be 2 (linear polynomial) although there are materials that lead to smaller errors when a quadratic polynomial is used. This is due to the materials with the most significant changes in reflectance also having higher reflectance. And the critical materials for the performance are the ones that have a lower reflectance.

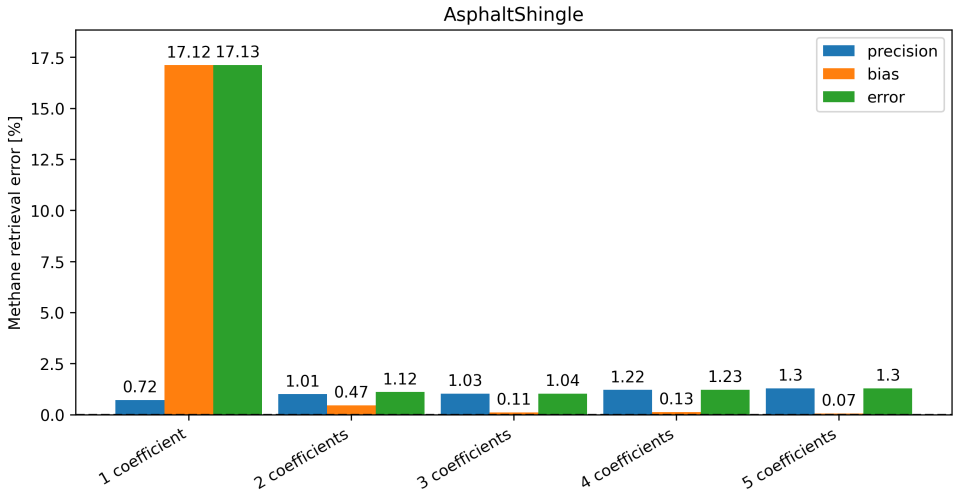

(a) Asphalt shingles (1625nm to 1670nm)

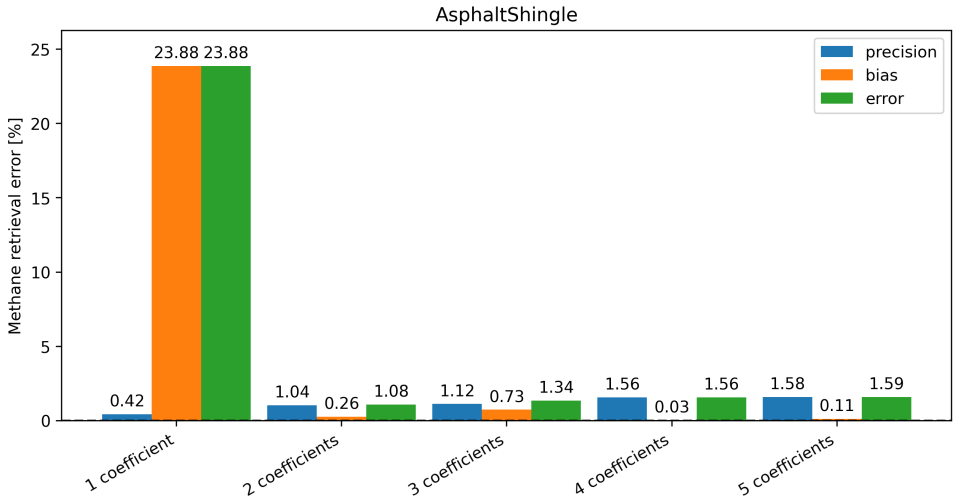

(b) Asphalt shingles (1590nm to 1670nm)

Figure 5.11: Comparison of the impact of spectrally dependant albedo on the retrieval of methane for different instrument wavelength ranges.

Finally, expanding the wavelength range to also include more sensitive absorption lines for carbon dioxide degraded the performance of the algorithm rather than improving it. This is due to the increase effect of the spectral dependency of albedo. It may be worthwhile exploring expanding the wavelength range slightly more to the right of the big absorption pocket of methane. In other words, increase the maximum wavelength from 1670 nm to 1680 nm or some other number. This could help in the retrieval of the albedo polynomials and thus reducing the bias of the inversion algorithm. However this may be limited by the detector quantum efficiency, because it reduces around 1670nm.

It is worth noting that the cases studied here represent a worst case scenario, where the pixel is completely covered by a material with a extremely wavelength dependent reflectance. In reality, each pixel of the image will contain a mix of materials with different wavelength dependencies such that the total surface reflectance will be much less dependant on the wavelength. Thus the impact of the wavelength dependence of the surface reflectance will be smaller. In fact, studies of the precision of GOSAT reference fitting only a slope for the surface reflectance [29]. Thus the higher order terms may be less significant in a scene with more heterogeneous materials.

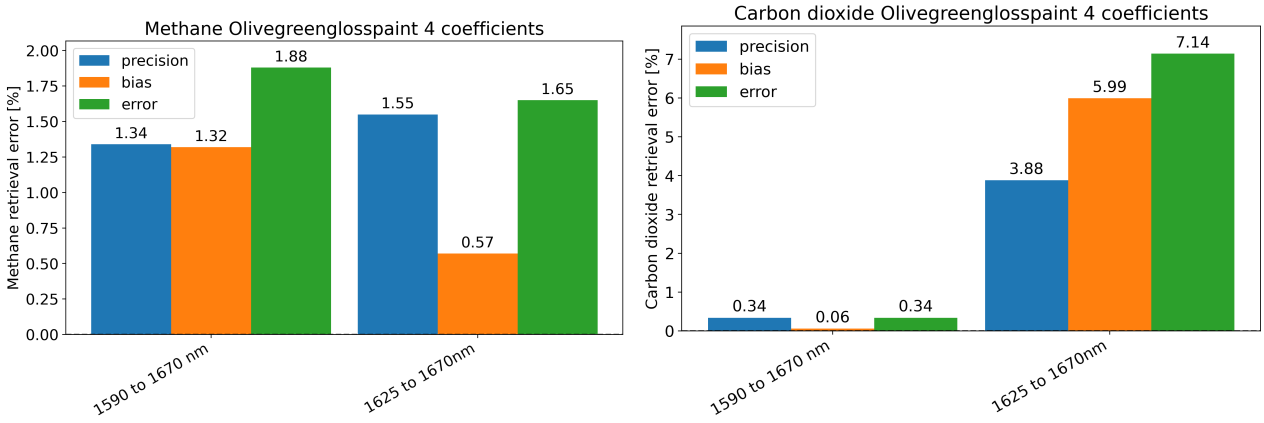

(a) Methane **(b) Carbon dioxide**

Figure 5.12: Comparison between wavelength ranges. Methane and carbon dioxide retrieval when using the new filter selection method, using cubic polynomials for the albedo, fitting h2o and co2.

6 Telescope design

The instrument volume will be mainly driven by the telescope, due to the photonic crystals being place on the detector. The objective is then finding the most compact telescope that meets the mission requirements. This chapter starts by laying out the instrument requirements, this includes global requirements, requirements on the performance of the instrument and requirements on the telescope design, presented in Section 6.1. Also in Section 6.1 the calculations of some requirements are explained with why some design decisions were made. This followed by the investigation of a three mirror anastigmat design in Section 6.2, this telescope concept was chosen due to being an industry standard. Also, a two mirror design was investigated and presented in Section 6.3,due to the small field of view of the instrument and the possibility of further reducing its volume . The final objective of this chapter is to answer the sub-question: *"What is the size of such an instrument?"*.

6.1. Requirements

First of all some requirements on the mission geometry were set, shown in Table 6.1. This requirements were taken from the TANGO mission, this is done for the designed instrument to be comparable with TANGO. Therefore at the end it can be said how much volume/mass is saved.

Table 6.1: Requirements on the mission geometry taken from the TANGO missions in order to be comparable with it.

Mission geometry requirements			
Requirement ID	**Requirement short name**	**Requirement statement**	**Requirement origin**
CSPEC-MGEO -0001	Target areas	The instrument shall be able to observe 300 (Goal)/ 150 (Threshold) different scenes within 4 days	TANGO
CSPEC-MGEO -0002	Scene area	The scene shall cover and area of 30x30 km2	TANGO
CSPEC-MGEO -0003	Altitude	The instrument shall fly at an altitude of 500 km	TANGO
CSPEC-MGEO -0004	Viewing zenith angle limitations	The instrument shall operate with viewing zenith angle smaller than 30 degrees	TANGO
CSPEC-MGEO -0005	Solar zenith angle limitations	The instrument shall operate with solar zenith angle smaller than 80 degrees	TANGO

The following requirements are related to the performance of the instrument and the telescope requirements. The telescope requirements are mainly derived from the performance calculations and will be further explained. The performance requirements are set such that the instrument will be useful in the same scenes as TANGO and with a comparable performance.

6.1.1. Performance requirements

The performance requirements were mainly derived from the TANGO mission, once again such that the missions are comparable. The gases to be retrieved are based on the proxy method, which is also used by TANGO.

Table 6.2: Requirements on the performance of the instrument part 1

Radiance and noise requirement			
Requirement ID	**Requirement short name**	**Requirement statement**	**Requirement origin**
CSPEC-RAD -0001	Gases to be retrieved	The instrument shall be able to retrieve CO2 and CH4 concentrations.	Proxy method
CSPEC-RAD -0002	Wavelength range to be used	The instrument shall operate in the wavelength range 1590 to 1670nm.	CSPEC-RAD -0001
CSPEC-RAD -0003	Full well at maximum radiance	The full well capacity of the detectors shall not be exceeded, when observing a scene with albedo 0,75 at solar zenith angle 10 degrees and viewing zenith angle zero.	Detector
CSPEC-RAD -0004	Precision at 0.15 albedo and 70 sza	The precision of the instrument on a scene with albedo 0.15 and solar zenith angle of 70 degrees shall be smaller than 0.5% (Goal)/ 1%(Threshold)	TANGO
CSPEC-RAD -0006	Binning factors	The Instruments shall be able to support operation with different binning factors	TANGO
CSPEC-RAD -0007	Spatial resolution	The instrument shall have a ground sampling distance smaller or equal to 300 meters	TANGO

An intricate requirement to this instrument concept is in the limitation of the F-number due to the transmission of the photonic crystal. If the F-number is too small, the cone of light that reaches the crystal becomes wider and therefore there is bigger effect of the angle dependency of the transmission. This effect tends to dampen the spectral features of the transmission, as shown in Chapter 2. Thus a limitation of F-number bigger than 6 is placed, based on simulations shown in Figure 6.1.

Another aspect is that the telescope parameters can be optimised for the lowest brightness scene, and then on the brightest scenes the detector gets overfilled and the measurements become useless. Thus requirement CSPEC-RAD-003 was added to ensure the functioning of the instrument also in

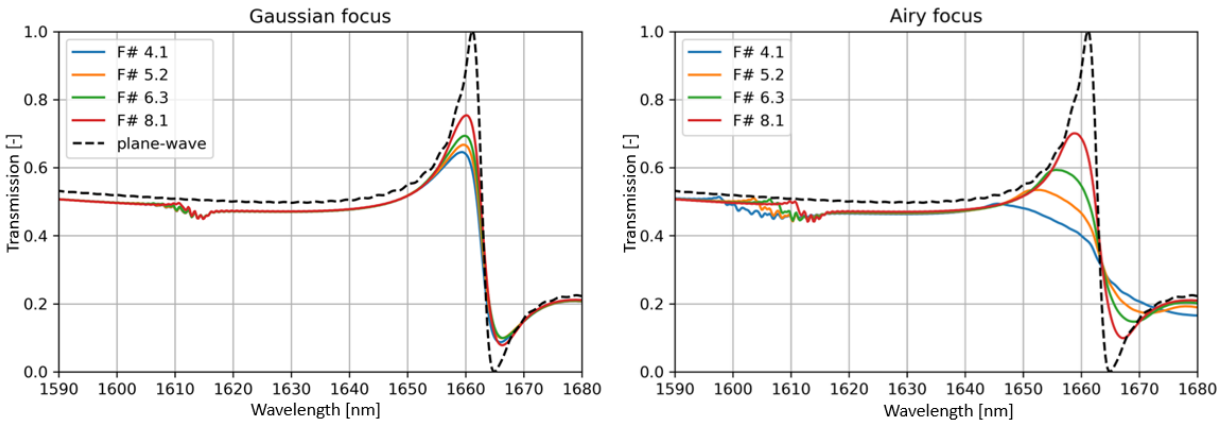

Figure 6.1: Effects of focusing the beam on the transmission of the filters, as simulated at SRON.

the brightest scenes. Finally, the dynamic range of the detector also had to be constrained. This is done to reduce the difference in signal intensity of the darkest pixel in the lowest brightness scene to the brightest pixel of the brightest scene. The brightest pixel drives what will be the maximum allowed aperture and the darkest pixel is related to the precision at the lowest brightness scene. Thus constraining this range allows increasing the aperture and allows the precision in the lowest brightness scene to be improved. This was done by imposing the minimum filter transmission and maximum filter transmission, which constrain the darkest and brightest pixels respectively. Lastly, a limitation due to the detectors maximum readout speed was imposed such that only achievable readout speeds are used.

Table 6.3: Requirements on the performance of the instrument part 2

Radiance and noise requirement			
Requirement ID	**Requirement short name**	**Requirement statement**	**Requirement origin**
CSPEC-RAD -0008	F-number limitations	The instrument shall have an F-number bigger than 6	Photonic crystal transmission
CSPEC-RAD -0009	Aspect ratio of ALT to ACT	The aspect ratio between the spatial resolution in across and along track direction shall be ≥ 0.75 and ≤ 1.5.	TANGO
CSPEC-RAD -0010	Minimum filter transmission	Each filter shall have an average transmission bigger than 0.3	Dynamic range detector
CSPEC-RAD -0011	Maximum filter transmission	Each filter shall have an average transmission smaller than 0.9	Dynamic range detector
CSPEC-RAD -0014	Read frequency	The readout frequency shall not exceed the detector's maximum readout frequency	Detector

These requirements were used on a spreadsheet to estimate the telescope parameters and the pa-

rameters used as input for the instrument simulator. As a ballpark estimate a signal to noise ratio of 400 was set as the goal, as in earlier simulations this signal to noise ratio would lead to a precision close to 1%. However the true goal is the requirement CSPEC-RAD-004, which depends also on the filter selection and can only be verified by running the instrument simulator.

6.1.2. Telescope parameters and requirements

The telescope requirements were set up by adapting the spreadsheet with for the performance until all requirements were met. The parameters that could be adjusted in the spreadsheet were:

- Integration time (t_{int})
- F-number across track and along track ($F\#_{\mathrm{ACT}}$ and $F\#_{\mathrm{ALT}}$)
- Binning across track, along track and temporal ($\mathrm{bin}_{\mathrm{temp}}$, $\mathrm{bin}_{\mathrm{ACT}}$ and $\mathrm{bin}_{\mathrm{ALT}}$)

From these parameters a few others were derived which will be used for the telescope design:

- Aperture across track and along track (D_{ACT} and D_{ALT})
- Focal length across track and along track (f_{ACT} and f_{ALT})
- Half field of view across track and along track ($\mathrm{FoV}/2_{\mathrm{ACT}}$ and $\mathrm{FoV}/2_{\mathrm{ALT}}$)

Whereas the following parameters were important for the instrument simulator to estimate the performance.

- Detector being used
- Ground resolution element across track and along track ($\mathrm{GRE}_{\mathrm{ACT}}$ and $\mathrm{GRE}_{\mathrm{ALT}}$)
- Instantaneous element across track and along track (G_{iACT} and G_{iALT})
- Aperture across track and along track (D_{ACT} and D_{ALT})
- Binning along track, across track and temporal ($\mathrm{bin}_{\mathrm{temp}}$, $\mathrm{bin}_{\mathrm{ACT}}$ and $\mathrm{bin}_{\mathrm{ALT}}$)
- Integration time (t_{int})
- Spacecraft altitude (H)

The instantaneous ground element can be different from the ground resolution element due to binning and smearing of the pixel. The smearing is due to the instrument being considered to be pointing always in nadir direction. As a picture is taken the detector is exposed to the radiance for some time, called integration time. Since the spacecraft is moving, the area that the detector is receiving the radiation from also moves, so the total area from which the radiation was measured is bigger, as shown in Figure 6.2. This effects of stretching the pixel is called smearing and can also be observed in photographs of fast moving objects such as humming birds.

In order to get the output parameters a few intermediate parameters were calculated. The first was how much time is necessary for a ground element to be imaged, this affects the smearing. This was done using Equation 6.1, where t_{smear} is the smearing time, t_{int} is the integration time, $\mathrm{bin}_{\mathrm{temp}}$ is the temporal co-adding and t_{dead} is the detector dead time. The detector Lynred Snake low gain is being used, which has no dead time so $t_{\mathrm{dead}} = 0$.

$$t_{\mathrm{smear}} = t_{\mathrm{int}} \cdot \mathrm{bin}_{\mathrm{temp}} + t_{\mathrm{dead}} \tag{6.1}$$

After that the instantaneous ground elements were calculated. The instantaneous element in the across track direction is the ground element divided by the binning $G_{\mathrm{iACT}} = \mathrm{GRE}_{\mathrm{ACT}}/\mathrm{bin}_{\mathrm{ACT}}$. However in the along track direction the instantaneous ground element was calculated using Equation 6.2. Where V_{proj} is the projected spacecraft velocity on the ground and depends only on the orbital altitude. The mathematical relations are illustrated in Figure 6.3.

Figure 6.2: The effect of smearing on the ground element. The dark green square is the instantaneous ground element. The light green is the area covered by smearing, which is the ground element.

$$G_{\mathrm{iALT}} = \frac{\mathrm{GRE}_{\mathrm{ALT}} - t_{\mathrm{smear}} \cdot V_{\mathrm{proj}}}{\mathrm{bin}_{\mathrm{ALT}} \cdot \mathrm{bin}_{\mathrm{temp}}} \tag{6.2}$$

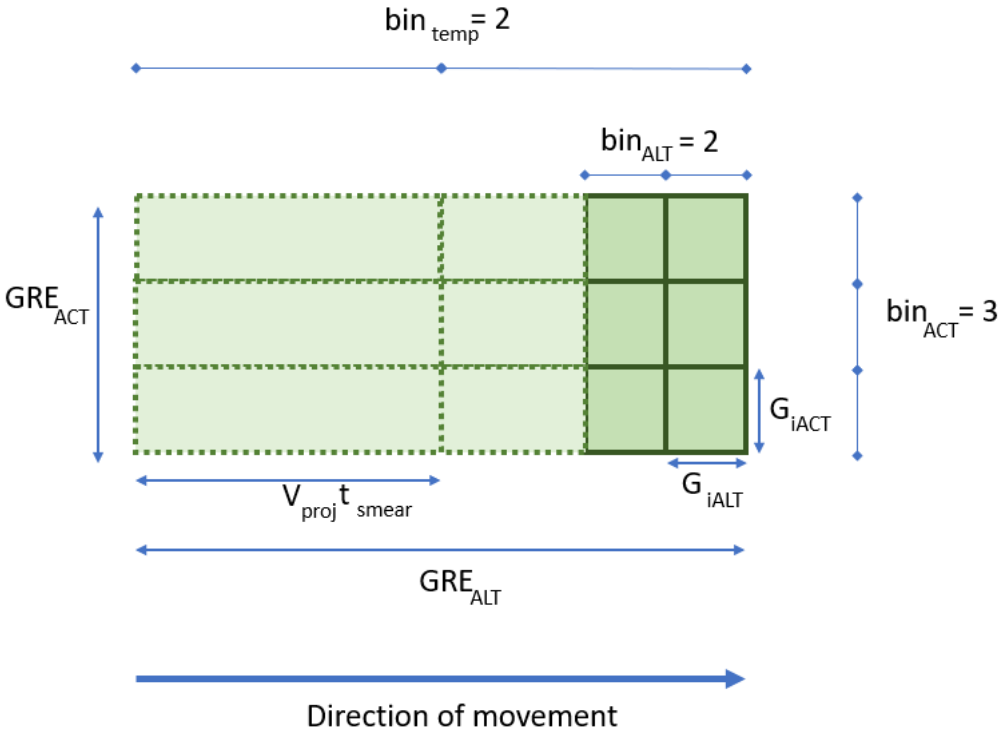

Figure 6.3: Relation between the ground resolution element (GRE) with the binnings, the instantaneous elements and the smearing.

The swath was also calculated in order to check that requirement $CSPEC - MGEO - 0002$ was met, this was simply the amount of pixels in the detector in each direction and the instantaneous ground element for each direction, for instance $\mathrm{Swath}_{\mathrm{ACT}} = G_{\mathrm{iACT}} \cdot N_{\mathrm{ACT}}$. For the Lynred-snake-lowgain detector there are 512 by 640 pixels, for which 640 were placed in the along track direction.

The focal length in the across and along track direction were calculated by using the effective pixel size in each direction. The effective pixel size is the pixel pitch (15 microns for Lynred-snake-lowgain) times the binnings in that direction. The focal length was then derived using the paraxial relation for lateral magnification, seen in Equation 6.3 and illustrated in Figure 6.4. Where H is the spacecraft orbital altitude and p_{effACT} is the effective pixel size.

$$f_{\mathrm{ACT}} = \frac{H \cdot p_{\mathrm{effACT}}}{G_{\mathrm{iACT}}} \tag{6.3}$$

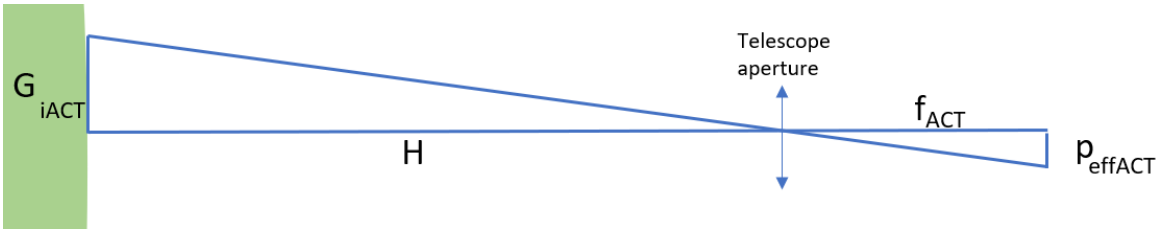

Figure 6.4: Relation between instantaneous ground element, pixel size, focal length and orbital altitude.

The aperture can be derived from the focal length and the F-number requirements. The aperture was calculated by inverting the definition of F-number, $F\# = f/D$, to get the aperture D as the result. The way the calculations are set up the F-number will directly impact the aperture, whereas the focal length depends on both binning of the ground element and the integration time. Thus a quick way of increasing the aperture is decreasing the F-number.

Finally, the actual read out frequency was calculated using the integration time and the detectors dead time, so $\mathrm{freq}_{\mathrm{readout}} = 1/(t_{\mathrm{dead}} + t_{\mathrm{int}})$.

Lastly, an estimate of the signal to noise ratio was required to obtain quick ideas of what performance the parameters used would give. This was divided into calculating the signal for a low brightness scene S_{low} and the expected noise for that scene N_{low}. The signal to noise ratio being the ratio of the two.

The signal was calculated by using the radiance (I_{low}) on top of the atmosphere, in photons per second per steradian per meter squared,in the spectral range from 1590nm to 1670nm. The scene had a standard concentration of the gases, albedo 0.15 and solar zenith angle of 70 degrees. The signal was then calculated using Equation 6.4, where q_e is the quantum efficiency of the detector, $coad$ is the total coadding (multiplication of all binnings) and T_{low} is the lowest average transmission of the filters (set to 0.3 by the requirement $CSPEC - RAD - 0010$). Furthermore, the etendue ε of the instrument was required. This is calculated using Equation 6.5, the definition of the solid angle and areas used is shown in Figure 6.5.The aperture is considered to be squared and will be designed this way.

$$S_{\mathrm{low}} = I_{\mathrm{low}} \cdot q_e \cdot T_{\mathrm{low}} \cdot t_{\mathrm{int}} \cdot \varepsilon \cdot \mathrm{coad} \tag{6.4}$$

$$\varepsilon = \mathrm{GRE}_{\mathrm{ACT}} \cdot \mathrm{GRE}_{\mathrm{ALT}} \cdot \Omega_{SC} = \frac{\mathrm{GRE}_{\mathrm{ACT}} \cdot \mathrm{GRE}_{\mathrm{ALT}} \cdot D_{\mathrm{ACT}} \cdot D_{\mathrm{ALT}}}{H^2} \tag{6.5}$$

Finally the noise can also be calculated using Equation 6.6, where i_{dark} is the detectors dark current and σ_{read} is the read noise from the detector.

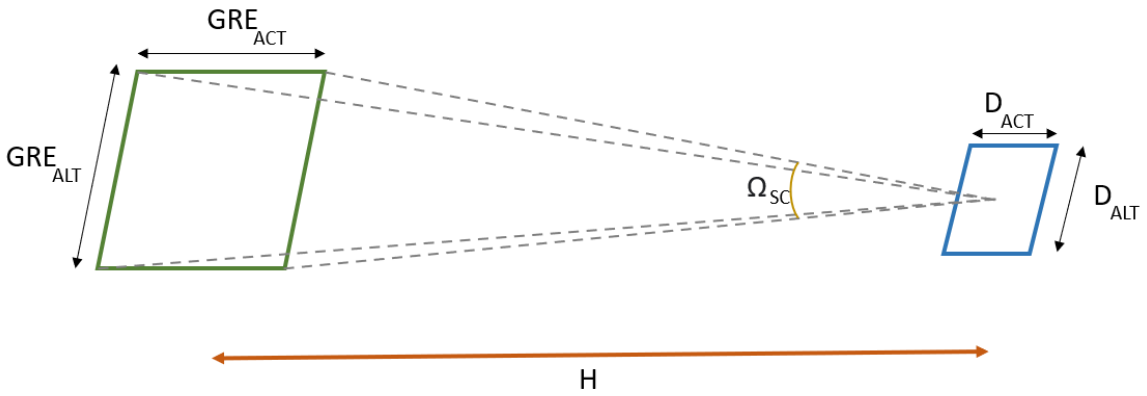

Figure 6.5: Definition of solid angle and areas used for calculating the etendue.

$$N_{\text{low}} = \sqrt{S_{\text{low}} + coad \cdot (\sigma_{read}^2 + i_{dark} \cdot t_{\text{int}})} \tag{6.6}$$

The signal of the brightest scene was also required to check requirement $CSPEC - RAD - 0003$, this was calculated by adjusting the radiance of the lowest brightness scene to the values of the brightest scene, as set in the requirement. This is summarised in Equation 6.7, where 0.75 is the albedo of the brightest scene and 0.15 is the albedo of the lowest brightness scene; the cosines ratios are for the solar zenith angles of each scene. Lastly, he transmission ratio T_{high}/T_{low} is meant to change the average transmission from the lowest to the highest value to according to requirement $CSPEC - RAD - 0011$. The signal was divided by the coad factor in order to get the signal in photons per pixel. This way it is easier to check if this values exceed the full well depth of the detector.

$$S_{\text{pixelbright}} = S_{\text{low}} \frac{0.75}{0.15} \frac{\cos 10°}{\cos 70°} \frac{T_{\text{high}}}{T_{\text{low}}} \frac{1}{\text{coad}} \tag{6.7}$$

The signal to noise ratio calculated here are approximations, since they use average values of transmission and radiance. In reality when running the simulation the signal to noise ratios will be slightly different for the darkest pixels and might exceed the full well depth for the brightest pixels in the brightest scene.

Parameters calculations

The spreadsheet was then used to calculate the value of the signal to noise ratio. The objective was set to find the values for integration time, F-number and binning such that the best signal to noise ratio is achieved, while all requirements are met. No binning in the along track direction was done as this would reduce the allowed integration time, thus increasing it would only reduce signal to noise ratio.

The initial choice was to check the performance without binning. The integration time would then be set such that the focal lengths are the same in both directions. After that, the aperture would be increased until either the minimum F-number was achieved or the detector was over-filled for the brightest scene. However, in this scenario it is not possible to have the focal length in the across track direction equal to the along track direction. This is due to the effective pixel size being the same for both directions. So for the projection on the surface to be also the same, the integration time has to be zero. This is due to the smearing caused by the integration time shown in Figure 6.2.

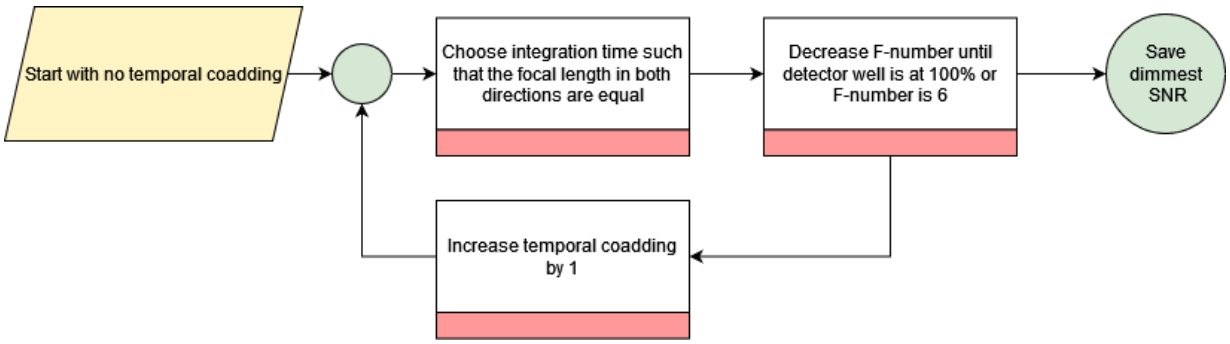

Figure 6.6: Steps used in the investigation of the parameters on the performance of the instrument

The first decision was to increase the binning in the across track direction until the swath was close to the 30km, which is necessary to reach the requirement of 30x30km of imaged area. This happened with a binning of 5 pixels across track, which lead to a across track swath of 30,72 km. This also increased signal-to-noise ratio, because the effective pixel size is increased in the across track direction. The focal length in the across track direction also increased, because the effective pixel size increased in Equation 6.3.

The focal length on the along track direction depends on the integration time. In order to increase it to match the across track direction, the integration time had to be increased. This ends up overflowing the detector, so the aperture is decreased until the full well capacity is not exceeded. All in all the aperture becomes bigger and thus signal to noise ratio reduces. All of this being said, temporal binning could still be added to improve the performance, thus these cases are also explored.

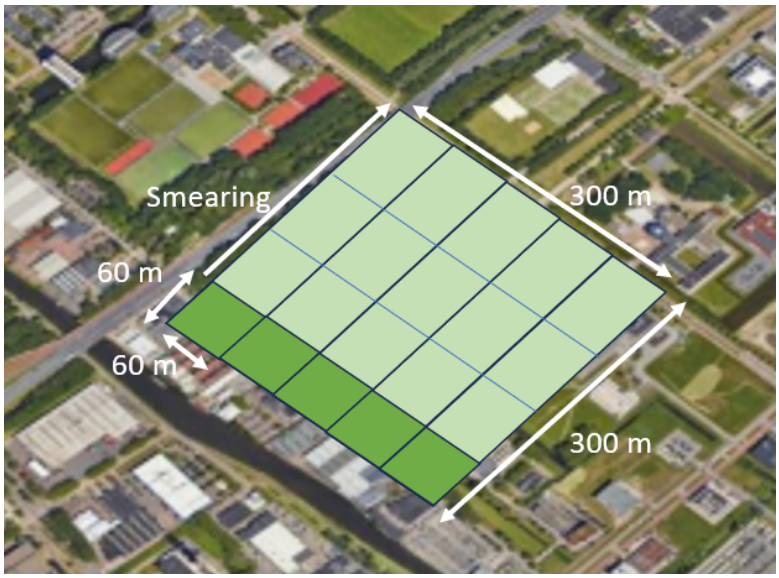

Figure 6.7: Projection on the ground of 5 pixels binned together in the across track direction. In this layout 3 temporal binning are also used. The smearing due to each temporal binning is marked by the blue lines.

The procedure followed is described in Figure 6.6. First the integration time is set such that the focal length in both directions are equal. Than the F-number is used to adjust the aperture such that the brightest scene uses 100% of the detector full well depth. This is then repeated for different temporal coaddings. Increasing the temporal co-adding means more shots are to be used per ground element, as depicted in Figure 6.7 where the ground element is the light green area and the blue lines represent the points where a new shot shot starts. This effectively increases how many times the full well of each pixel can be used. A version of this flow was also made for the case where there would be no

constraint on the minimal F-number. The results are shown in Table 6.4.

Table 6.4: Different temporal binning and their respective integration time, F-number and signal-to-noise-ratio found for them. Cases where the F-number constraint was not considered were also added.

Temporal binning [-]	1	2	3	4	4	5	5	20
Integration time [m s]	33.98	16.99	11.33	8.50	8.50	6.80	6.80	1.70
F-number [-]	11.66	8.24	6.73	6	5.83	6	5.21	2.61
SNR low brightness [-]	211	300	367	403	424	370	474	949

The F-number constraint quickly becomes active, limiting the maximum signal-to-noise ratio that can be achieved. The case chosen to be proceeded with was 4 temporal binning with the constraint active. This case uses 94% of the detector full well capacity in the bright scene and thus leaves some margin for the approximations used in the spreadsheet. However, if no constraint in the F-number was present the signal to noise ratio could be doubled, which happens when 20 temporal sampling are done. At this point the detector readout frequency becomes the limit.

Table 6.5: Different exposure modes and the range of solar zenith angles they could be used for. SNR is calculated for lower bound of solar zenith angle, surface albedo of 0.15 and F-number 6

Mode number	Upper sza limit [deg]	Lower sza limit [deg]	Exposure time [ms]	Temporal binning [-]	SNR [-]
1	70,00	59,82	33,98	1	604
2	59,82	48,44	16,99	2	680
3	48,44	34,50	11,33	3	761
4	34,50	10,00	8,5	4	830

The F-number was mainly driven by the full well capacity of the detector being exceeded. Using 4 temporal binning with an exposure time of 8.5 ms leads to only 2% of the detector full well depth being used in the lowest brightness scenes. The measurement becomes then dominated by detector noise. Therefore, the instrument could be set to different exposure modes depending on the solar zenith angle of the scene. So for a scene with a big solar zenith angle (bigger than 60 degrees) the instrument would use one temporal binning with a longer exposure time such that the detector gets filled more and the contribution of detector noise gets smaller.The suggested modes and the solar zenith angle ranges they could be used for are shown in Table 6.5.

The final requirements for the telescope design are shown in Table 6.6. The dimensions derived from the performance calculations were set as requirements, together with a requirement to ensure telecentricity. Requirements from TANGO on the mass and volume of the instrument were copied to serve as a baseline. And finally requirements CSPEC-TEL-0005 and CSPEC-TEL-0004 were added as basis of what design is good enough.

6.2. Three mirror anastigmat telescope

The design started with a three mirror anastigmat, which has become an industry standard. This telescope has three mirrors and enough design parameters such that coma, astigmatism and spherical aberrations can be compensated for. The layout of the system is shown in Figure 6.8.

Table 6.6: Requirements for the telescope design.

Telescope requirements			
Requirement ID	**Requirement short name**	**Requirement statement**	**Requirement origin**
CSPEC-TEL -0001	Focal length	The instrument shall have a focal length of 125 mm	Performance calculation
CSPEC-TEL -0002	Aperture	The instrument shall have an aperture of 20.83 mm	Performance calculation
CSPEC-TEL -0003	Telecentricity	The variation of the angle of incidence on the detector along the field of view shall be smaller than 0.35 degrees	Telecentricity
CSPEC-TEL -0004	Diffraction	The instrument shall have an Strehl ratio bigger than 0.7	
CSPEC-TEL -0005	Integrated energy	The system integrated energy along a effective pixel shall be bigger than 70%	
CSPEC-TEL -0006	Radiation	The optical surfaces shall tolerate radiance for the lifetime of the mission	
CSPEC-TEL -0007	Telescope volume	The instrument volume shall be smaller than 8 U.	TANGO
CSPEC-TEL -0009	Telescope mass	The telescope mass shall be smaller than 27 kg.	TANGO

The second mirror was defined as the aperture stop in order to have an inner pupil that can be used for stray-light control and should also facilitate the miniaturisation of the telescope. The first mirror was left as an spherical surface, because it is cheaper to fabricate than conical surfaces. However, in order to compensate for astigmatism, coma and spherical aberration the other two mirror require a conic term.

The optimisation from ZEMAX was used in order to achieve a design that meets the requirements. The variables given to the algorithm were the curvature of the first and second mirrors, the conic terms of the secondary and tertiary mirrors and the distance between the surfaces. The curvature of the tertiary mirror was constrained such that the F-number of the system is always 6.

A few constraints were set in order for the optimisation algorithm to give sensible results. The first constraint was on the distances in the y direction of the entrance to the secondary mirror, also from the secondary mirror to the tertiary mirror, and the secondary mirror to the detector. The distance from the top of the mirror to the bottom of the detector was constrained to be bigger than 25mm which is enough for the encasing of the detector chip. The other distances were set to be bigger than 7 mm in order to ensure no overlap between mirrors.

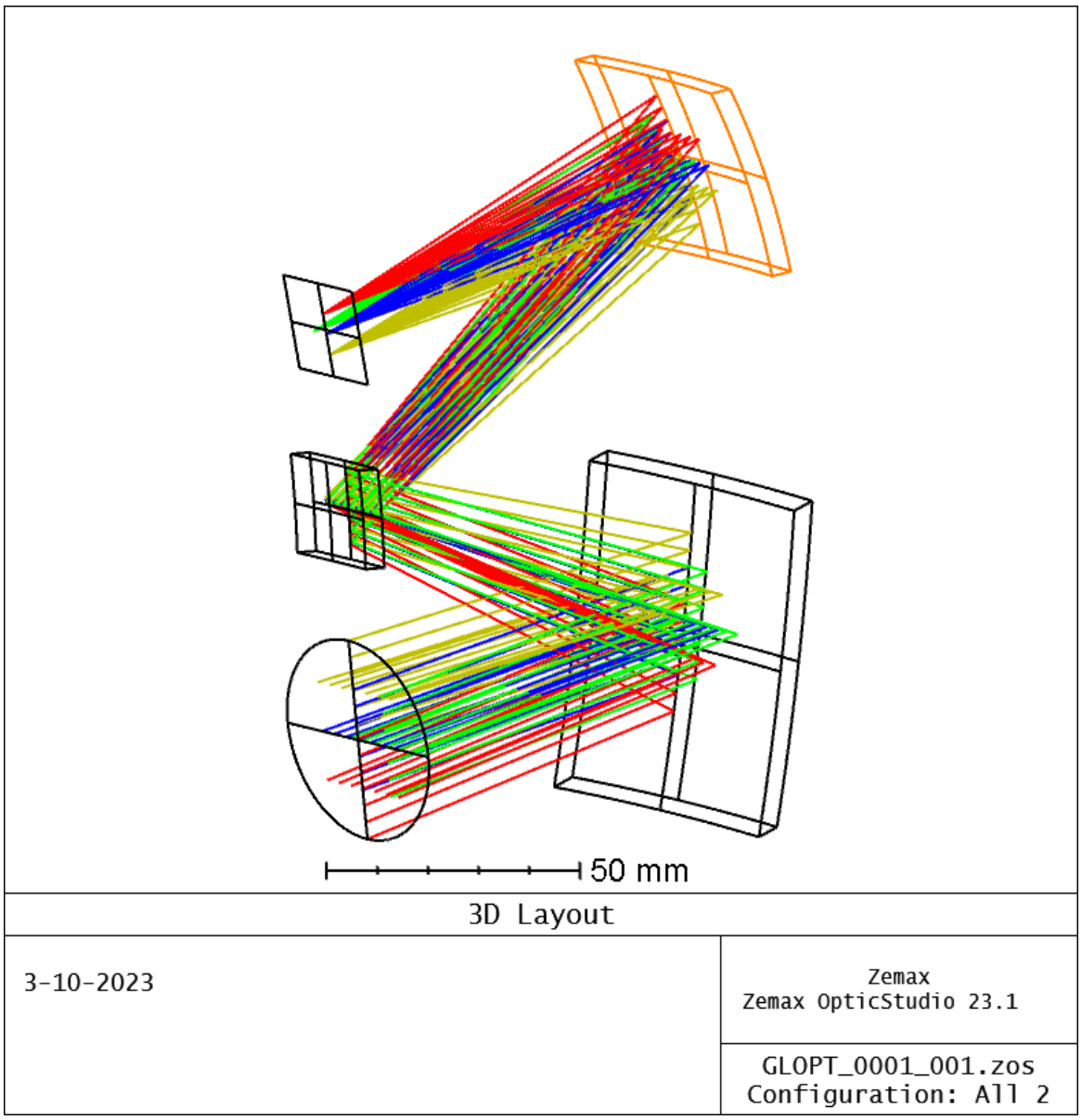

Figure 6.8: Layout of the three mirror telescope. The highlighted surface is the tertiary mirror.

The software sometimes gives solutions where the calculation considers the ray is reflected on a surface but the 3d model show it going through it. This is caused by the distance between two surfaces being the wrong sign, so the surface that the ray has to go to after the reflection is on the wrong side. In order to avoid this, constraints on the distance in the z direction were set to be always bigger than 5 mm. This ensures the initial order is maintained.

After that constraints to ensure telecentricity were added. These were done by calculating the angle of incidence of the chief ray of different pupil positions onto the detector plane. This angle was not allowed to vary more than 0.35 degrees, as set in requirement CSPEC-TEL-0003 .

Finally, in order to force the optimisation to compact the system, constraint were added on the maximum distance in the z and y direction of the system. The values were tweaked but settled on maximum 10cm in the z direction and 9.5cm in the y direction. These limits were reduced until the optimiser struggled to find solutions.

6.2.1. Performance

The main criteria to accept the performance was the encircled energy as defined in the requirement. However, other parameters were looked into to investigate the performance of the telescope. The spot diagram is in Figure 6.9. The central field is dominated by astigmatism and also has some coma in it, however the points fall inside the airy disk. For fields further fro the centre, coma becomes more dominant ans some rays fell outside the airy disk. Also from this diagram it is possible to calculate the root mean square distance of the rays.

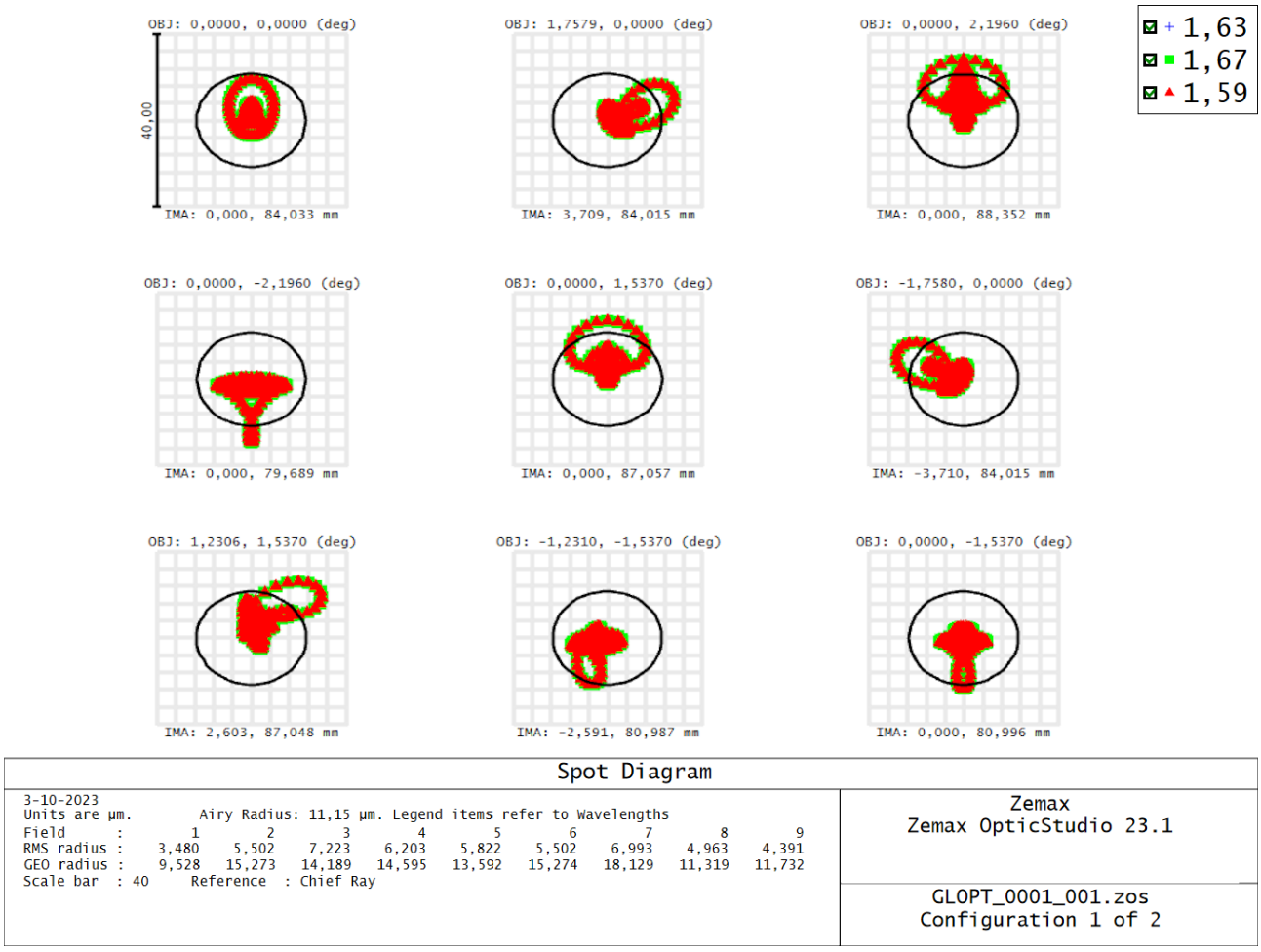

Figure 6.9: Spot diagram for the tree mirror anastigmat design.

In order to evaluate how this changes over the field a plot of the RMS wavefront error as a fraction of the wavelength was made as a function of the field angle, shown in Figure 6.10. For all points in the field the root mean square error is less than $72m\lambda$ of the wavelength range,indicating the design is diffraction limited in the entire field of view.

Finally, in order to evaluate if the design meets the requirement of the integrated energy over an effective pixel the plot for the integrated energy versus the distance of the centre of a circle was made. In fact, the encircled energy over a single pixel was already above 70% for this design, as shown in Figure 6.11.

The total volume of the telescope was estimated from the 3D layout, the maximum distance in the y direction was 110 mm where in the z direction it was also about 110 mm and for the x direction it was 40mm. The distance in the y and z direction are a bit bigger than the ones used in the optimisation, this is due to the furthest point of the surface not always being the ray that was being used for the

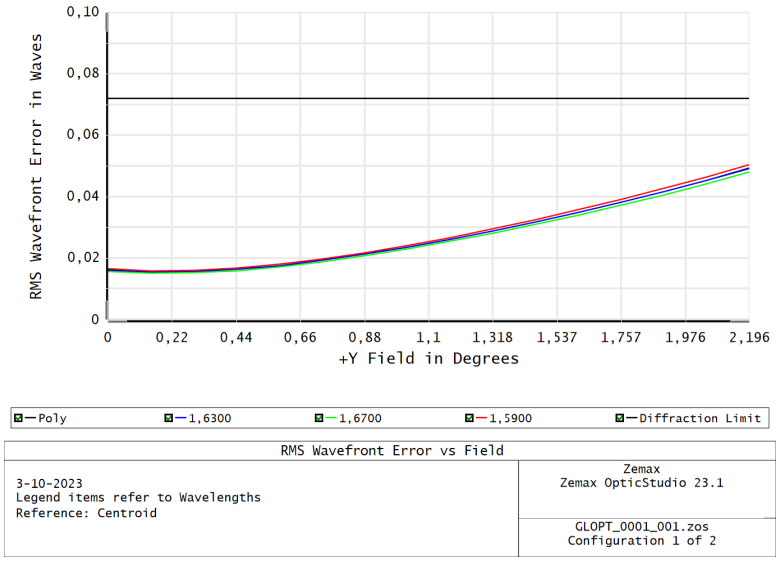

Figure 6.10: Root mean square wavefront error vs field for the tree mirror anastigmat design.

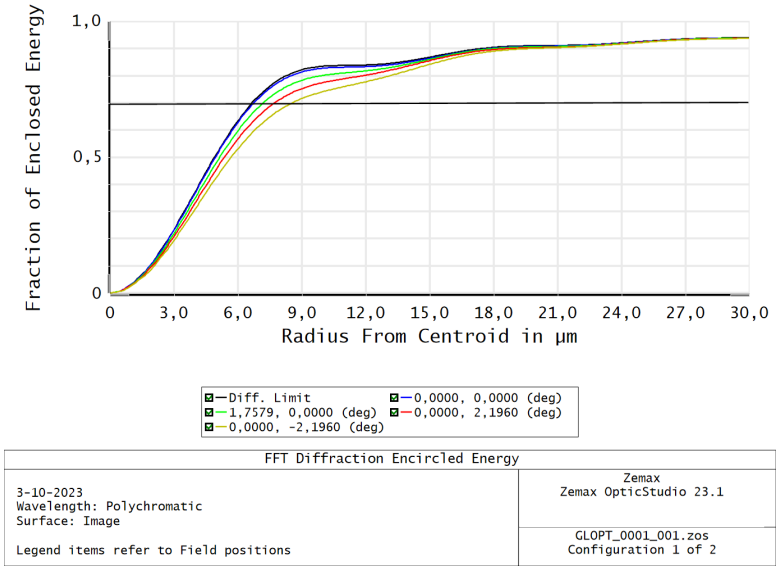

Figure 6.11: Diffraction encircled energy for the tree mirror anastigmat design. Black line was drawn at the 70% threshold.

calculation of the distance. Furthermore, this volume estimation considers that the mirrors have a thickness of 0.5cm. The total volume of the instrument was rounded up to be 110x110x50 mm in order to ensure the detector can also fit. This is equivalent to a volume of 0.6 litres or a bit over half a unit of a cube sat. Using the volume of the mirrors and the density of aluminium the mass of the instrument without support structures or the mass of the detector would be 24 grams.

6.3. Two mirror telescope

The first mirror of the three mirrors anastigmat was almost flat. Also, the field of view of the instrument is relatively narrow, supporting that maybe a two mirror telescope will satisfy the requirements for the instrument. For this reason, the design of a two mirror telescope that meets the requirements was investigated. This would not only reduce volume and mass of the telescope but also the cost of manufacturing for the instrument.

The aperture stop was defined ahead of the first mirror to facilitate the adjustment of telecentricity. Besides that, the same procedures and functions for the optimisation were used as for the three mirror

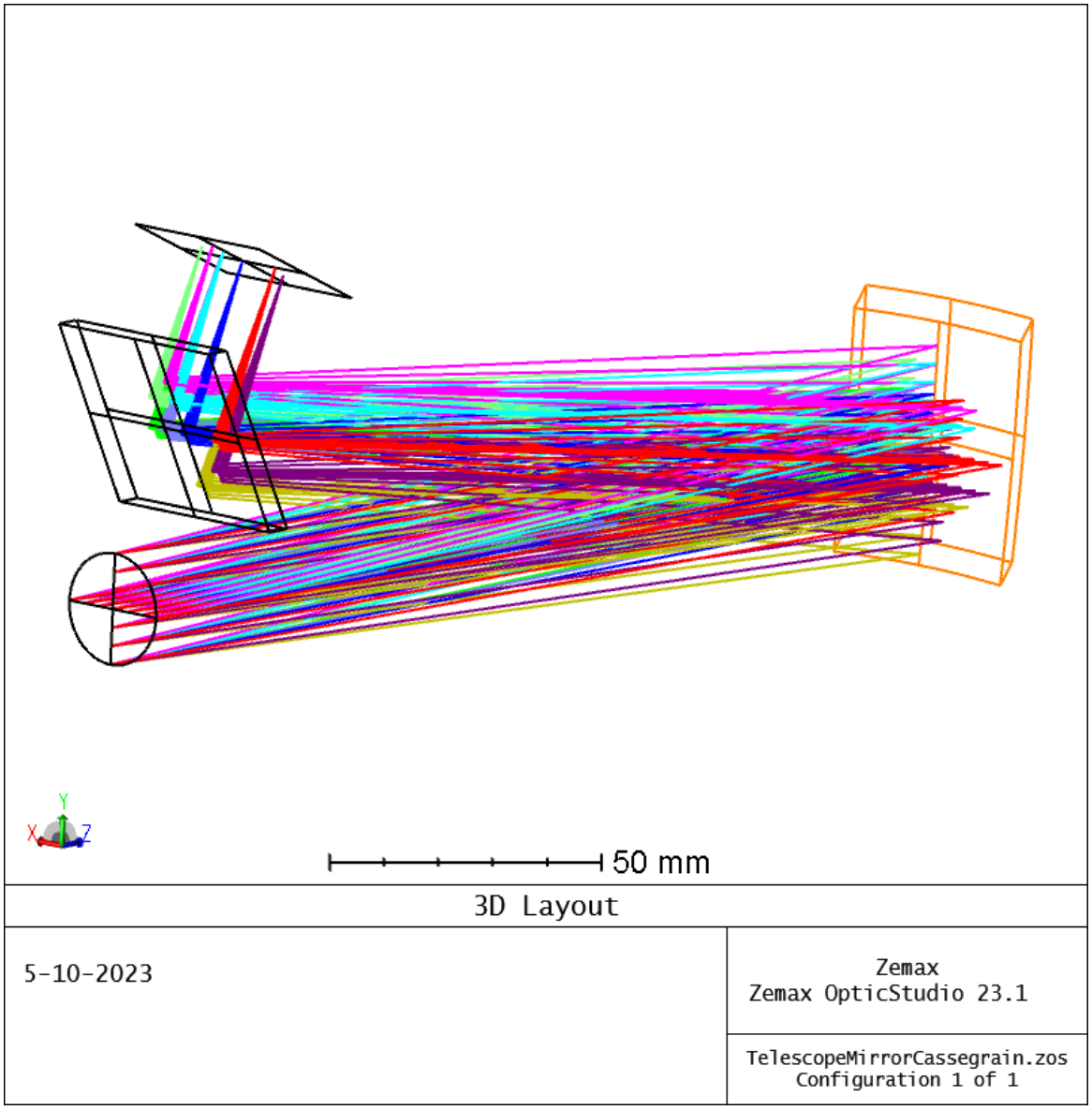

Figure 6.12: Layout of the two mirror telescope. The highlighted surface is the tertiary mirror.

telescope. The difference being that there were less parameters to be adjusted. In this case both mirror are still conics and the radius of the last mirror is set such that the F-number is always 6. The variables left were the rotations and offset of each element, as well as their distances. Also the radius of the mirror and the conic constants of both mirrors were allowed to vary.

6.3.1. Performance

The spot diagram in Figure 6.13, shows already significant coma and astigmatism for the central field. And as the field of view increases, the astigmatism tends to increase at first only to increase again at the edge. This is due to the performance being optimised for the half way to the edge of the field of view, in order to balance out the aberrations on the central and on the edge of the field of view.

This effect of the optimisation is further observed in the root mean squared error along the field of view. It is at its minimum when the field is around 1.1 degrees, only to increase again, as shown in Figure 6.14. Furthermore, on the root mean square plot, it may appear that the instrument is diffraction limited in Figure 6.14. However when the negative y direction is evaluated it shows that at some point the image is not diffraction limited as seen in **??**.

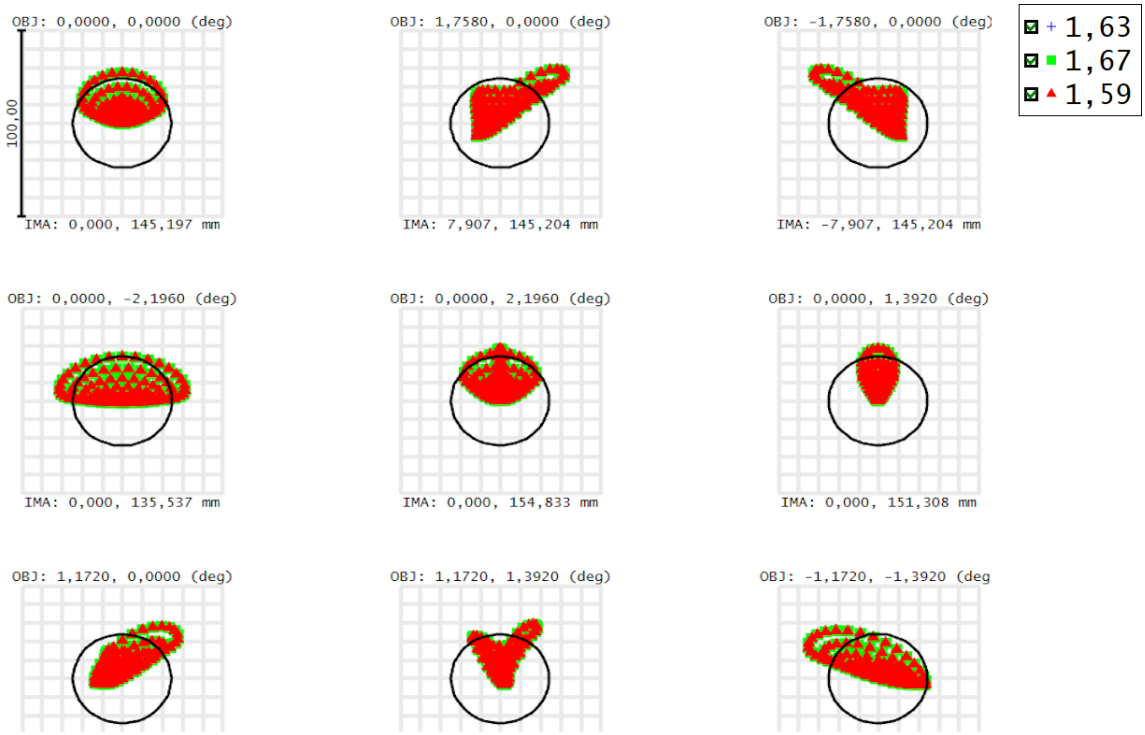

Spot Diagram

5-10-2023
Units are µm. Airy Radius: 24,31 µm. Legend items refer to Wavelengths

Field	1	2	3	4	5	6	7	8	9
RMS radius :	13,669	17,140	17,140	18,110	14,868	12,209	15,297	14,570	17,915
GEO radius :	27,359	41,992	41,992	32,113	28,264	28,242	36,919	33,952	39,552

Scale bar : 100 Reference : Chief Ray

Zemax
Zemax OpticStudio 23.1

TelescopeMirrorCassegrain.zos
Configuration 1 of 1

Figure 6.13: Spot diagram for the two mirror telescope design.

Finally the encircled energy was evaluated. At 15 microns the encircles energy is not above 70% for all fields. However, it is above the threshold at 30um, or two pixels. This mean that for this two mirror design at least two pixels would have to be used in both directions to cover the requirement on the encircled energy.

The final dimensions of the telescope with two mirrors are: 240 mm in the z direction, 70 mm in the y direction and 40 mm in the x direction. The same rounding was for the three mirror telescope was done to accommodate for the detector finalising to a volume of 240x70x50 mm, which equates to 0.84 litters, or almost 1 unit of a cubesat. The telescope ended up being longer due to the presence of less mirrors to fold the focal length. Using the volume of the mirrors and the density of aluminium the mass of the instrument without support structures or the mass of the detector would be 9.77 grams. Thus it is significantly lighter.

6.4. TANGO volume and mass comparison

The instrument was compared to the requirements set to TANGO, as the mission is being developed and values for it can frequently change. Furthermore, the mass of only the mirrors were considered for the calculation of the total instrument mass. Whereas for TANGO the requirement of maximum mass was used, thus it is not a fair comparison.

All in all, the instrument can achieve a precision close to the one achieved by TANGO with a third of the aperture size, thus with less light. This is reflected in the instrument size which is reduced to both the aperture being smaller and the instrument not requiring the dispersion of different wavelengths.

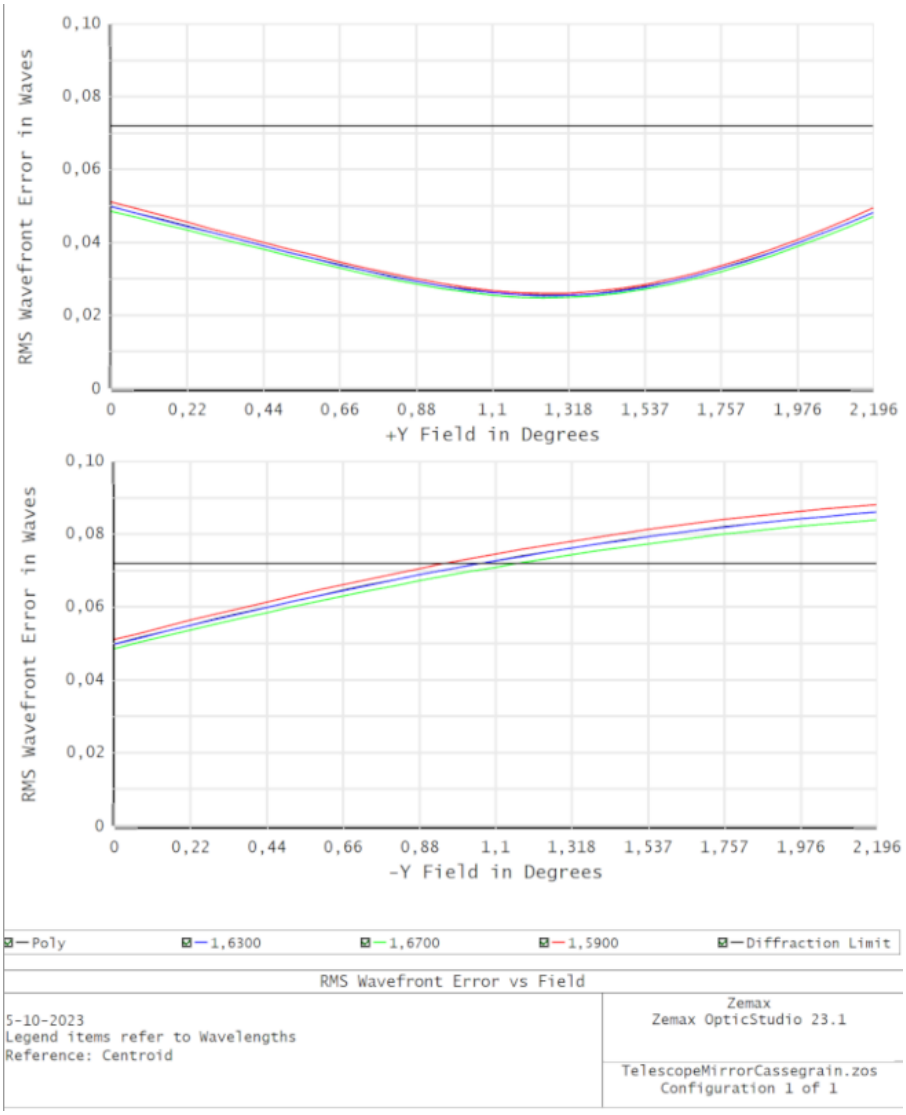

Figure 6.14: Root mean square wavefront error for the two mirror telescope design in the positive and negative y direction.

In fact, the volume of the compressSpec points to the possibility of fitting it into a unit and launching it into a small CubeSat.

The swath is 30.3 kilometres wide for both instruments, this is due to both of them using a CCD with the same array size, binning 5 pixels in the across track direction and using the same ground resolution element size.

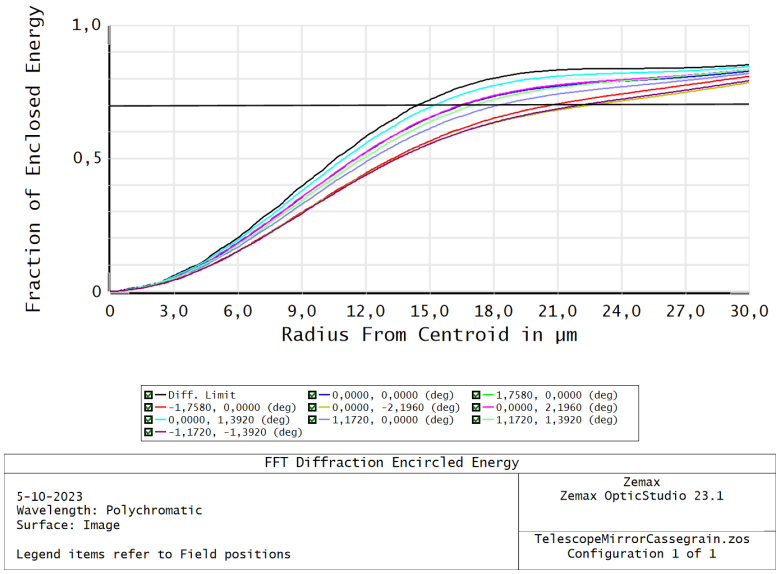

Figure 6.15: Encircled energy for the two mirror telescope

Table 6.7: Comparison of main parameters between TANGO and CompressSpec. Precision is for the albedo 0.15 and solar zenith angle 70 deg without considering spectral dependency of the surface reflectance.

	TANGO	CompressSpec
Aperture [mm]	65	20.83
Volume [mm x mm x mm]	8U 95 x 215 x 415	0.6U 50 x 110 x 110
Mass [kg]	8.5	0.03 (mirrors only)
Precision [%]	1.0	1.1
Swath [km]	30.3	30.3

7 Performance outlook

This chapter has an outlook on what can still improve the performance of the instrument. First, visualising the data product will be a next step of the project. Complete scene simulations are performed in Section 7.1 and the impact of improving the instrument precision is visualised. After that, the possible improvement in the performance of the instrument due to a better set of filters is explored in Section 7.2. It may be that there are filters that improve the precision of the instrument but were not simulated in the initial library.

7.1. Scene simulation

The instrument simulator for TANGO was provided by Jochen Landgraf [30]. In this simulator, a scene was generated with the Jänschwalde coal power plant in Germany and a carbon dioxide plume that would be expected to be seen from it. This carbon dioxide plume was normalised by the usual carbon dioxide background concentration and used as an enhancement for a methane plume. These concentrations are consistent with a small methane plume as can be inferred from data retrieved by GHGSat-D [31]. The location of the plant and the data used as input for the simulator are shown in Figure 7.1. Furthermore, the average solar zenith angle used for this scene is 29 degrees. The same simulator as used in Chapter 5 was ran once in each pixel of the image to generate a retrieval of the scene for the instrument.

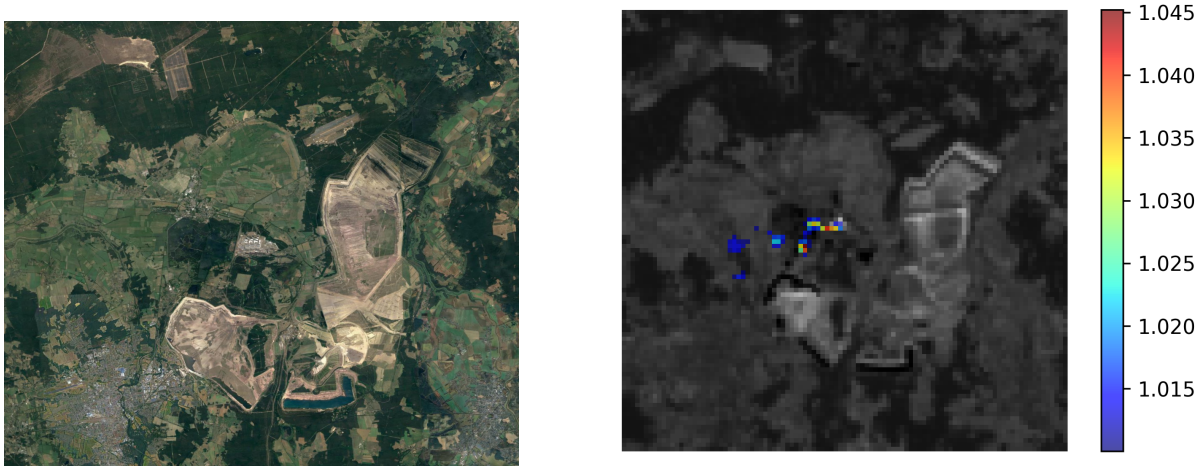

(a) Map showing the Jänschwalde coal power plant. Taken from Google Earth: https://earth.google.com/web/

(b) Data used as ground truth for the scene simulation, albedo was taken from Sentinel 2 data and plume was simulated for the TANGO simulator.

Figure 7.1: Image of the scene used in the simulation and the ground truth used for the surface reflectance and methane plume. The scale is an enhancement above the usual level with 1 being the background level.

The scene was also run for different F-number so the effect of reducing the F-number constraint can be visualised. This is because a smaller F-number leads to a better signal to noise ratio. The values that changed between each F-number are shown in Table 7.1. The maximum amount of temporal binning was 20, this is limited by the detector's maximum read out frequency of 600 Hz. This is also the case where the aperture can be the biggest.

Table 7.1: Different instrument parameters for cases where the F-number constrain is reduced. Precision for a scene with 0.15 albedo, sza 70 degrees, fitting also H_2O and CO_2.

F-number	6	4.12	2.6
Aperture [mm]	20.833	30.33	47.96
Temporal binning [-]	4	8	20
Integration Time [ms]	8.496	4.248	1.699
Precision [%]	1.1	0.77	0.48

The simulated scenes can be seen in Figure 7.2. The albedo on top of the forest, as retrieved from Sentinel-2 data, is very low, around 0.05. Thus the retrieval works much worse on top of those regions, resembling a picture of white noise. A precision of 1.1% is enough to barely tell the plume apart from the noise. But as the precision is improved the plume becomes easier to be identified. This shows the gains of improving the precision, because smaller sources can be detected or quantified.

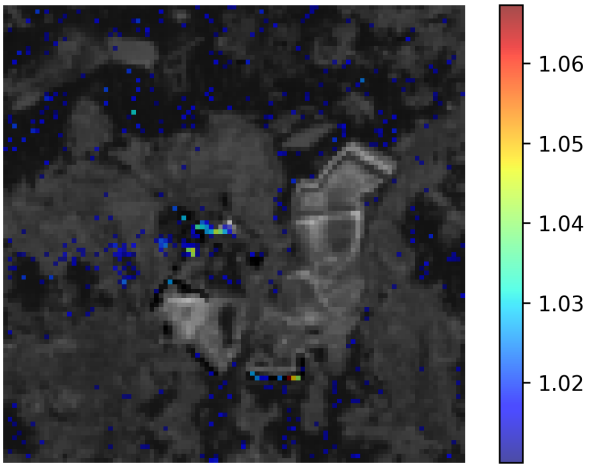

(a) F-number = 2.6, Precision = 0.48%

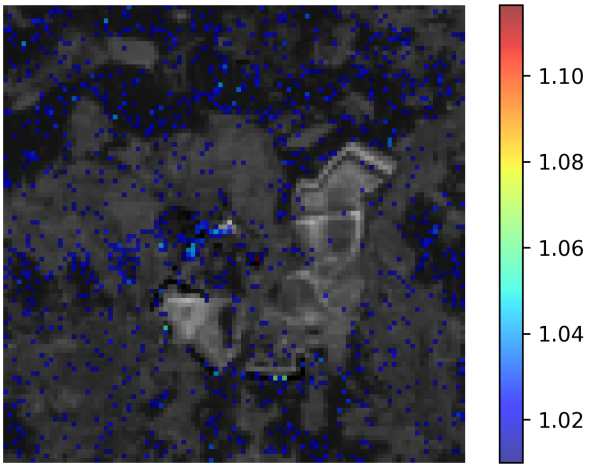

(b) F-number = 4.12, Precision = 0.77%

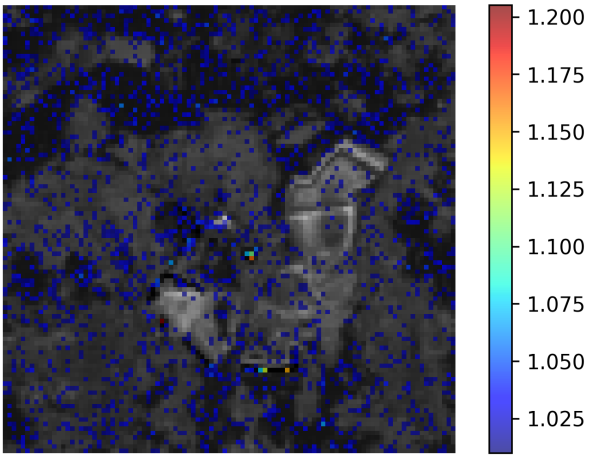

(c) F-number = 6.0, Precision = 1.1%

Figure 7.2: Complete scene simulation for different F-numbers using data gathered for the TANGO simulator. Retrieved methane concentrations above 1.01 are overlaid on top of the albedo retrieval.

7.2. Theoretical better filters

Lastly, a set of theoretical filters were picked in order to see the potential for improvement in the filter selection. This was done by doing the singular value decomposition of the Jacobian of the top of the atmosphere radiance, shown in Equation 7.1. Each row of the matrix in Equation 7.1 is the sensitivity of the radiance to each of the parameters being retrieved.

$$\frac{\partial I_{\mathrm{ToA}}(x_0)}{\partial \mathbf{X}} = \begin{pmatrix} \frac{\partial I_{\mathrm{ToA}}}{\partial \mathrm{xCH_4}} \\ \frac{\partial I_{\mathrm{ToA}}}{\partial \mathrm{H_2O}} \\ \frac{\partial I_{\mathrm{ToA}}}{\partial \mathrm{xCO_2}} \\ \frac{\partial I_{\mathrm{ToA}}}{\partial \mathrm{Alb_0}} \end{pmatrix} \tag{7.1}$$

The parameters considered here were: spectrally constant albedo, water vapour, carbon dioxide and methane. When the singular value decomposition is done; The right singular vectors maps each of the parameters to a singular value, whereas the left singular vectors map the singular values to the points in the spectrum. In this decomposition the right singular vectors almost completely separate the parameters, therefore each parameter is mapped mainly to one singular value. Thus there is also one and only one left singular vector related to each of the parameters.

The left singular vector can have positive and negative values but it shows which regions of the spectrum are more sensitive to each parameter. Thus the absolute value of these vectors were taken and normalised by the maximum absolute value in the vector. So all points in the vector are between zero and one, and can be treated as transmission functions. These transmission functions separated the regions of the spectrum that are more sensitive to changes in each of the parameters. The calculated transmissions are shown in Figure 7.3.

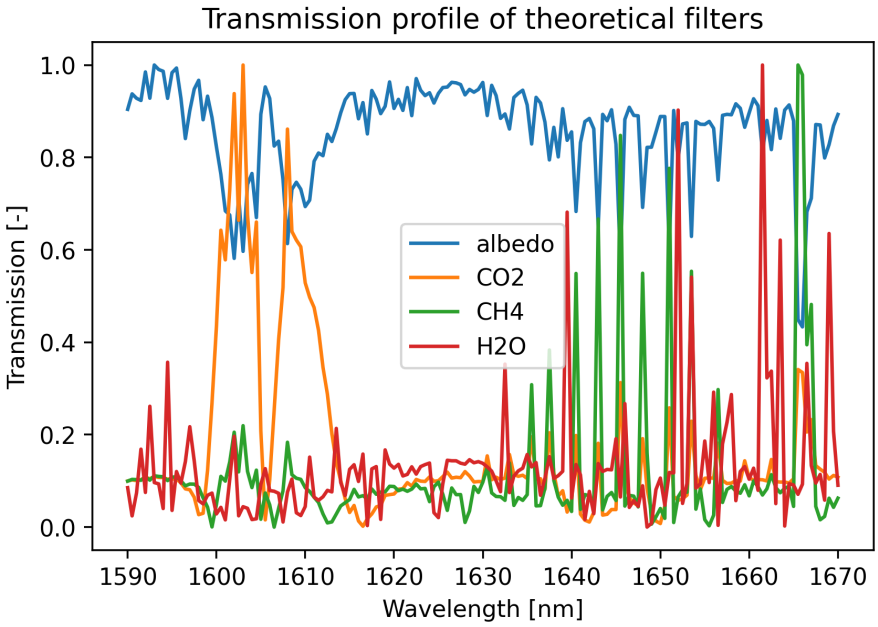

Figure 7.3: Filters fabricated based on the Jacobian of the spectrum relative to the fit parameters.

The theoretical filters show the difficulty of telling apart impact in the measurement due to water vapour and methane concentrations. This is due to the lines that are more sensitive to this gases overlapping in this spectral range, as seen in Figure 7.3 from 1630 nm to 1670nm. Thus it requires filters with

sharp spectral features very close to each other in order to better differentiate those two gases. Exploring other wavelengths just to measure water vapour concentrations might be another way forward.

After that the performance of these theoretical filters were simulated for the cases where the F-number was 6 and where the F-number is 2.6. The scenes are shown in Figure 7.4.

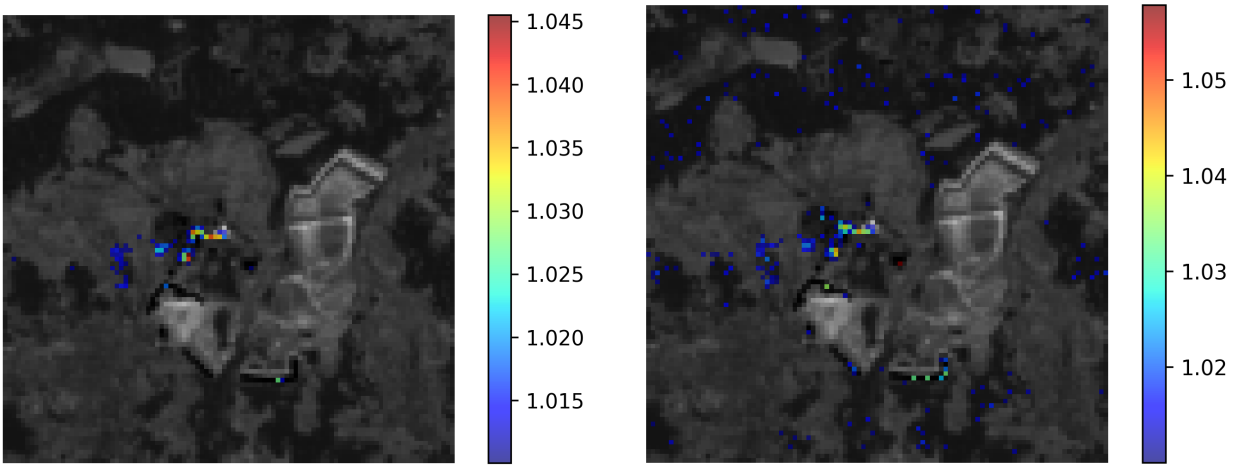

(a) F-number = 2.6, Precision = 0.14% **(b) F-number = 6.0, Precision = 0.32%**

Figure 7.4: Complete scene simulation for different F-numbers using data gathered for the TANGO simulator. Retrieved methane concentrations above 1.01 are overlaid on top of the albedo retrieval.

The precision was brought down to 0.14%, when the theoretical filters are used and the maximum read-out frequency of the detector is also used. In this case even the concentration of the pixels over the forest can be well resolved, as shown in Figure 7.4. Lastly, this filters are not realistically achievable due to their multiple sharp peaks. However, they do show the room for improvement that there is for futures filter libraries and selection methods.

8
Conclusion

The Paris agreement set the goal to limit the global temperature rise to below 2 degrees above pre-industrial levels. To achieve this, countries committed themselves to track and reduce their greenhouse gas emissions. Accurate and frequent measurements of emissions are required to evaluate the impact of policies, which is often performed from space due to its capability to image large areas. By reducing the size ad cost of instruments, more spacecraft can be launched and therefore more frequent measurements of emissions by facilities can be made.

This thesis set out to explore an instrument concept that used photonic crystals as optical filters on a push-broom configuration to sample the spectrum of sunlight reflected by the surface of Earth. From this measurement the concentration of greenhouse gases on the region can be inferred. The main research question was **"Is an instrument based on photonic crystals filters viable for remote sensing of methane?"**. This was further divided into the following sub-questions:

1. What way of using photonic crystals for remote sensing is the most viable?
2. How does the instrument perform when considering the concentrations of other gases and spectral dependency of the surface reflectance?
   (a) What gases influence the retrieval of methane in the chosen band?
   (b) How big is the influence of the spectral dependence of surface reflectance?
   (c) How can the filter selection be improved based on the concentration of other gases and surface reflectance?
   (d) What are the effects of expanding the wavelength range used by the instrument?
3. What is the size of such an instrument?
   (a) What is the trade-off between Field of View, F-number, number of filters, spatial resolution and retrieval precision?
   (b) What is a viable optical design for such an instrument?
   (c) How does the instrument compare to TANGO?

8.1. Research sub questions:

Each of the sub-questions was answered in a different chapter. The following answers were drawn for each of them:

1.What possible concept configurations are there for the photonic crystal-based spectrometer?

In Chapter 2, different instrument concepts were explored which used both plane wave transmissions of the photonic crystals and the transmission when the light is focused onto the material. The best concept was the on-chip configuration with a top hat profile. In this design, the photonic crystal is placed on top of the detector and the light of the scene is focused on it. This concept ranked very well in signal to noise ratio due to the aperture not having to be divided. It is also a very simple concept that will lead to a compact design. On the other hand, it has the disadvantage that the spectral features of the filter tend to be dampened when light is focused on it. However, this effect can be mitigated by limiting the F-number of the instrument. Furthermore, there are photonic crystals that are less angle dependant and might not be so affected by the light focused on it. However, more research is

required in order to find those photonic crystals.

2.How does the instrument perform when considering the concentrations of other gases and spectral dependency of the surface reflectance?

In Chapter 5, the performance of the algorithm and the filter selection methods were explored. The impact of the concentration of other gases and the spectral dependency of albedo were investigated for the retrieval of methane. The effect of assuming the concentration of CO_2, H_2O, CO and N_2O were explored due to the presence of absorption lines for these gases in the spectral range 1625 to $1670nm$. The lines of CO were very weak and the effect on the retrieval of methane was negligible. N_2O had some impact in the retrieval of methane however the lines were too weak in order for the concentration of this gas to be retrieved and improve the bias in the retrieval of methane. Finally, H_2O and CO_2 had a significant impact in the retrieval of methane and the impact was significantly improved by adding them as fit parameters.

This was followed by exploring the spectral dependency of albedo. If the surface reflectance is better modelled by a linear polynomial and the fit algorithm tries to retrieve a constant polynomial, than it will compensate by introducing a systematic error in the concentration of the gases. In order to observe this, data from the ECOSTRESS missions was used and materials with significant spectral dependency were chosen. In fact, the spectral dependency of the surface reflectance introduced very significant biases. In fact, the total error of the instrument was dominated by the bias. Thus higher order polynomials had to be fitted in order to better model the reflectance of the surface. Each new polynomial order that had to be fitted reduced the precision of the methane retrieval, however it improved the bias. In general, a quadratic polynomial worked best to retrieve methane in the initial wavelength range.

After that, the wavelength range that the instrument uses was expanded from $1625 - 1670nm$ to $1590 - 1670nm$. This includes more absorption lines of carbon dioxide such that it can be better retrieved. Then the proxy method can be used in order to reduce bias that affects the same way both carbon dioxide retrieval and methane retrieval, an example is scattering in the atmosphere. This wavelength expansion further increased the sensitivity of the methane retrieval to errors in the retrieval of carbon dioxide. However, the extra absorption lines improved the retrieval of carbon dioxide by roughly 6 fold.

All in all, the effect of the spectral dependency of albedo will be smaller than what was studied in this chapter. Due to the scene being a mix of materials and the cases studied were significantly spectrally dependent albedo. In fact, GOSAT operates in a similar wavelength range and only fits a linear albedo in its retrieval model [29].

3. What is the size of such an instrument?

Chapter 6 explored the telescope design, as it is what defines the size of the instrument. The photonic crystals are just an extra layer on top of the detector, not adding significant volume. The chapter started by defining the parameters required by the telescope design, such as focal length, aperture size and field of view. It was chosen that the focal length in the across track direction and along track direction should be the same in order to simplify the telescope and thus its manufacturing costs.

The smallest F-number allowed for the instrument was set to 6, this was a rule of thumb for limiting the degradation of the spectral features in the transmission. Furthermore, the ground element of the

instrument is to be the same as for TANGO (300x300 m). Thus the focal length in the across track direction was chosen such that this was true. The pixels in the across track direction were also binned such that the swath width was close to the requirement of 30 km. This was necessary because the pixel will be smeared in the along track direction. The bigger the difference of the instantaneous size of the ground element is, the longer the instrument can integrate until the ground element is smeared to be 300 by 300 meters. In the end, 5 pixels are binned in the across track direction whereas only one is used in the along track direction. So the across track instantaneous pixel is 5 times bigger than along track to allow for smearing and a longer integration time.

As mentioned, the integration time was then chosen such that the ground element is smeared to be 300 by 300 meters. After that, the aperture was chosen such that in the brightest scene the detector is very close to being saturated. The detector filled up fairly quickly which made the aperture very small. In order to allow for a bigger aperture, temporal sampling was included. So for a single element the instrument will take multiple shots and combine them afterwards. With 4 temporal sampling the instrument aperture could be opened up until it reached the F-Number constraint of 6. Further increasing the temporal sampling would make the noise of the measurement more dominated by the detector noise and thus reduce the signal to noise ratio, this is due to not being able to further open the aperture because of the F-number constraint.

Based on this two designs for the telescope were made in ZEMAX. One using three mirrors and another one that uses just two mirrors. The three mirror design was the most compact occupying a volume of $110x110x50$ mm, or a bit over 0.6 litres. Whereas the two mirror design was a bit less compact due to it folding less the optical path. Furthermore the two mirror design can correct less for aberrations and concentrates less of the energy in a single pixel. However, the two mirror design would be cheaper and lighter since it features one less mirror.

The instrument volume will be much smaller than TANGO, 0.6 litres compared to the 8 litres set as a requirement for TANGO. The total mass cannot be fairly compared, as the estimations here do not include structures and the mass of the detector. However, the mirrors would weight 30 grams for the three mirror anastigmat whereas the requirement set for TANGO is for the total instrument mass to be smaller than 8.5 kg.

8.2. Research question and way forward

The main research question:*"Is an instrument based on compressive sensing using photonic crystals viable for remote sensing of methane?"*, was answered by the sub questions. It is a promising instrument that can be much more compact than current ones. In order to further improve its performance, it will require to explore photonic crystal that are less angle dependent an still have valuable resonances for the retrieval of methane, carbon dioxide and water vapour. Besides that, the current filter selection almost matches the performance of traditional dispersion spectrometers at a fraction of the volume. In Chapter 7, it was shown that there is still room for improving the performance of the instrument. Therefore, this concept is very promising.

The precision can still be significantly improved by finding better filter sets and being able to further open the aperture of the instrument, with the best possible scenario improving the precision from 1.1% to 0.14%. Furthermore, the concentration of water vapour is the most difficult to retrieve and thus introduces the biggest errors to the retrieval of methane. Thus exploring other wavelengths to improve the retrieval of water vapour may be a way forward to improve the instrument performance.

Furthermore, this instrument leaves margin to smaller ground resolution elements being used. Since at this point it does not require forward motion compensation. Including this compensation would both reduce the smearing of a pixel and increase the amount of light gathered by the instrument by a small region on the ground. Thus the instrument could image scenes more finely. However, if the size of the ground resolution element is reduced, the swath of the instrument would also be reduced. Since it is limited by the amount of pixels in the detector in the across track direction.

Further next steps is also building the instrument and testing it. It is very important in order to validate the instrument performance simulator. This will also help securing extra funding for the project and bring it closer to being flight ready.

Bibliography

[1] Jervis, D., McKeever, J., Durak, B. O., Sloan, J. J., Gains, D., Varon, D. J., Ramier, A., Strupler, M., and Tarrant, E., "The GHGSat-D imaging spectrometer," *Atmospheric Measurement Techniques*, Vol. 14, No. 3, 2021, pp. 2127–2140.

[2] Lipson, R., and Lu, C., "Photonic crystals: a unique partnership between light and matter," *European Journal of Physics*, Vol. 30, No. 4, 2009, p. S33.

[3] Johnson, S. G., Fan, S., Villeneuve, P. R., Joannopoulos, J. D., and Kolodziejski, L., "Guided modes in photonic crystal slabs," *Physical Review B*, Vol. 60, No. 8, 1999, p. 5751.

[4] *AFGL atmospheric constituent profiles (0-120km)*, 1986.

[5] Horowitz, C. A., "Paris agreement," *International Legal Materials*, Vol. 55, No. 4, 2016, pp. 740–755.

[6] Lan, X., Nisbet, E. G., Dlugokencky, E. J., and Michel, S. E., "What do we know about the global methane budget? Results from four decades of atmospheric CH4 observations and the way forward," *Philosophical Transactions of the Royal Society A*, Vol. 379, No. 2210, 2021, p. 20200440.

[7] Prather, M. J., "Lifetimes and eigenstates in atmospheric chemistry," *Geophysical Research Letters*, Vol. 21, No. 9, 1994, pp. 801–804.

[8] ESA, "Sentinel Overview," , 2023. URL https://sentinels.copernicus.eu/web/sentinel/missions.

[9] Gilbert, K., Turnbull, D., Walker, K., Boone, C., McLeod, S., Butler, M., Skelton, R., Bernath, P., Chateauneuf, F., and Soucy, M.-A., "The onboard imagers for the Canadian ACE SCISAT-1 mission," *Journal of Geophysical Research: Atmospheres*, Vol. 112, No. D12, 2007.

[10] Yang, Z., Zhang, P., Gu, S., Hu, X., Tang, S., Yang, L., Xu, N., Zhen, Z., Wang, L., Wu, Q., et al., "Capability of Fengyun-3D satellite in earth system observation," *Journal of meteorological research*, Vol. 33, 2019, pp. 1113–1130.

[11] Liu, Y.-N., Sun, D.-X., Hu, X.-N., Ye, X., Li, Y.-D., Liu, S.-F., Cao, K.-Q., Chai, M.-Y., Zhang, J., Zhang, Y., et al., "The advanced hyperspectral imager: aboard China's gaoFen-5 satellite," *IEEE Geoscience and Remote Sensing Magazine*, Vol. 7, No. 4, 2019, pp. 23–32.

[12] Blumstein, D., Chalon, G., Carlier, T., Buil, C., Hebert, P., Maciaszek, T., Ponce, G., Phulpin, T., Tournier, B., Simeoni, D., et al., "IASI instrument: Technical overview and measured performances," *Infrared Spaceborne Remote Sensing XII*, Vol. 5543, 2004, pp. 196–207.

[13] Guanter, L., Kaufmann, H., Segl, K., Foerster, S., Rogass, C., Chabrillat, S., Kuester, T., Hollstein, A., Rossner, G., Chlebek, C., et al., "The EnMAP spaceborne imaging spectroscopy mission for earth observation," *Remote Sensing*, Vol. 7, No. 7, 2015, pp. 8830–8857.

[14] Galeazzi, C., Sacchetti, A., Cisbani, A., and Babini, G., "The PRISMA program," *IGARSS 2008-2008 IEEE International Geoscience and Remote Sensing Symposium*, Vol. 4, IEEE, 2008, pp. IV–105.

[15] Kuze, A., Suto, H., Nakajima, M., and Hamazaki, T., "TANSO-FTS and CAI on GOSAT; Project Overview, Design, and Prelaunch Test Results," *AGU Fall Meeting Abstracts*, Vol. 2007, 2007, pp. A13D–1494.

[16] Imasu, R., Matsunaga, T., Nakajima, M., Yoshida, Y., Shiomi, K., Morino, I., Saitoh, N., Niwa, Y., Someya, Y., Oishi, Y., et al., "Greenhouse gases Observing SATellite 2 (GOSAT-2): mission overview," *Progress in Earth and Planetary Science*, Vol. 10, No. 1, 2023, p. 33.

[17] Aumann, H. H., Chahine, M. T., Gautier, C., Goldberg, M. D., Kalnay, E., McMillin, L. M., Revercomb, H., Rosenkranz, P. W., Smith, W. L., Staelin, D. H., et al., "AIRS/AMSU/HSB on the Aqua mission: Design, science objectives, data products, and processing systems," *IEEE Transactions on Geoscience and Remote Sensing*, Vol. 41, No. 2, 2003, pp. 253–264.

[18] Veefkind, J. P., Aben, I., McMullan, K., Förster, H., De Vries, J., Otter, G., Claas, J., Eskes, H., De Haan, J., Kleipool, Q., et al., "TROPOMI on the ESA Sentinel-5 Precursor: A GMES mission for global observations of the atmospheric composition for climate, air quality and ozone layer applications," *Remote sensing of environment*, Vol. 120, 2012, pp. 70–83.

[19] Day, J., Brenny, B., Palombo, E., de Goeij, B., Ouwerkerk, B., Misiun, G., Lemmen, M., Koc, N. A., Leemhuis, A., Landgraf, J., et al., "Development of the TANGO carbon instrument for greenhouse gas detection," *Remote Sensing Technologies and Applications in Urban Environments VIII*, Vol. 12735, SPIE, 2023, pp. 130–141.

[20] Wang, Z., Yi, S., Chen, A., Zhou, M., Luk, T. S., James, A., Nogan, J., Ross, W., Joe, G., Shahsafi, A., et al., "Single-shot on-chip spectral sensors based on photonic crystal slabs," *Nature communications*, Vol. 10, No. 1, 2019, p. 1020.

[21] Skorobogatiy, M., and Yang, J., *Fundamentals of photonic crystal guiding*, Cambridge university press, 2009.

[22] Fan, S., and Joannopoulos, J. D., "Analysis of guided resonances in photonic crystal slabs," *Physical Review B*, Vol. 65, No. 23, 2002, p. 235112.

[23] Wang, Z., and Yu, Z., "Spectral analysis based on compressive sensing in nanophotonic structures," *Optics express*, Vol. 22, No. 21, 2014, pp. 25608–25614.

[24] Siemons, M., Hagenaar, M., Adam, A., and Kohlhaas, R., "A compressive sensing with photonic crystals enabled spectrometer for trace gas observation," *International Conference on Space Optics—ICSO 2022*, Vol. 12777, SPIE, 2023, pp. 2911–2919.

[25] Gousset, S., Croizé, L., Le Coarer, E., Ferrec, Y., Rodrigo-Rodrigo, J., Brooker, L., and consortium http://scarbo-h2020. eu/, S., "NanoCarb hyperspectral sensor: on performance optimization and analysis for greenhouse gas monitoring from a constellation of small satellites," *CEAS Space Journal*, Vol. 11, 2019, pp. 507–524.

[26] Kochanov, R. V., Gordon, I., Rothman, L., Wcisło, P., Hill, C., and Wilzewski, J., "HITRAN Application Programming Interface (HAPI): A comprehensive approach to working with spectroscopic data," *Journal of Quantitative Spectroscopy and Radiative Transfer*, Vol. 177, 2016, pp. 15–30.

[27] Young, A. T., "Air mass and refraction," *Applied optics*, Vol. 33, No. 6, 1994, pp. 1108–1110.

[28] Meerdink, S. K., Hook, S. J., Roberts, D. A., and Abbott, E. A., "The ECOSTRESS spectral library version 1.0," *Remote Sensing of Environment*, Vol. 230, 2019, p. 111196.

[29] Schepers, D., Guerlet, S., Butz, A., Landgraf, J., Frankenberg, C., Hasekamp, O., Blavier, J.-F., Deutscher, N., Griffith, D., Hase, F., et al., "Methane retrievals from Greenhouse Gases Observing Satellite (GOSAT) shortwave infrared measurements: Performance comparison of proxy and physics retrieval algorithms," *Journal of Geophysical Research: Atmospheres*, Vol. 117, No. D10, 2012.

[30] Landgraf, J., Laasner, R., and Goudar, M., “Tango-Carbon End-to-End Simulator (TEDS): Algorithm Theoretical Baseline Document,” Tech. Rep. SRON-ESG-TN-2022-012, SRON Netherlands Institute for Space Research, Niels Bohrweg 4, 2333 CA Leiden, The Netherlands, August 2023.

[31] Varon, D. J., Jacob, D. J., Jervis, D., and McKeever, J., “Quantifying time-averaged methane emissions from individual coal mine vents with GHGSat-D satellite observations,” *Environmental science & technology*, Vol. 54, No. 16, 2020, pp. 10246–10253.

Column number density per atmosphere model layer

Table A.1: Data used for modelling a standard atmosphere [4]

Layer Thickness [km]	Average layer pressure [hPa]	Average Temperature [K]	Column number density H2O [cm^-2]	Column number density CO2 [cm^-2]	Column number density N2O [cm^-2]	Column number density CO [cm^-2]	Column number density CH4 [cm^-2]
1.0001573	955.06853	284.95241	1.6762846e22	8.0125539e20	7.7697492e17	3.5824831e17	4.1276791e18
1.0004721	845.98694	278.45364	1.1793346e22	7.2653441e20	7.0451823e17	3.1372569e17	3.7427535e18
1.000787	747.22068	271.95493	7.7700111e21	6.5725525e20	6.3733838e17	2.736608e17	3.3858588e18
1.0011021	658.00629	265.45628	4.7511433e21	5.9313816e20	5.7516446e17	2.3880235e17	3.0555657e18
1.0014173	577.62039	258.95769	2.8476266e21	5.3391146e20	5.1773174e17	2.1133927e17	2.7504346e18
1.0017327	505.37845	252.45918	1.6644341e21	4.7931149e20	4.6478886e17	1.884426e17	2.4692418e18
1.0020482	440.63364	245.96075	9.6054883e20	4.290826e20	4.1607353e17	1.6507073e17	2.2098972e18
1.0023639	382.77564	239.4624	5.3851841e20	3.829771e20	3.713936e17	1.4138389e17	1.9707009e18
1.0026797	331.22944	232.96415	2.6712038e20	3.4075521e20	3.3022606e17	1.1782338e17	1.7505305e18
1.0029957	285.45417	226.46599	9.5414467e19	3.02185e20	2.9198155e17	9.5665628e16	1.5468487e18
1.0033118	244.94199	219.96795	4.1282461e19	2.6704238e20	2.5576207e17	7.6559714e16	1.3595642e18
1.003628	209.37779	216.65	1.8560729e19	2.3183828e20	2.1900112e17	5.903788e16	1.1723514e18
1.0039445	178.8329	216.65	8.6675368e18	1.9807919e20	1.843397e17	4.2552373e16	9.9253084e17
1.004261	152.74401	216.65	4.1058675e18	1.6923592e20	1.5503301e17	2.9017298e16	8.3867208e17
1.0045777	130.46109	216.65	2.3122966e18	1.4459267e20	1.3017651e17	1.9464889e16	7.0771371e17
1.0048946	111.42888	216.65	1.668573e18	1.2353785e20	1.0896243e17	1.2955718e16	5.9646461e17
1.0052116	95.173179	216.65	1.2245108e18	1.0554893e20	9.0484907e16	8.7840279e15	5.0120024e17
1.0055288	81.288923	216.65	1.0514931e18	9.0179458e19	7.4469663e16	6.0299495e15	4.1981166e17
1.0058461	69.430159	216.65	8.9453675e17	7.7048012e19	6.0597058e16	4.0295176e15	3.5020024e17
1.0061635	59.301401	216.65	7.7327034e17	6.58287e19	4.8664997e16	2.8244218e15	2.8935042e17
4.0278318	40.669051	218.43736	2.2102357e18	1.7924576e20	1.1395014e17	6.9244912e15	6.9715683e17
4.0329233	21.879258	222.44115	1.2866726e18	9.4815179e19	4.8723997e16	4.4048981e15	2.962827e17
4.0380244	11.901565	226.44479	7.2455851e17	5.0728393e19	2.1699758e16	2.6268492e15	1.4067705e17
53.83805	1.1675343	244.461	9.2270274e17	6.1458622e19	1.2199755e16	6.2445749e15	1.1267054e17